

**Characterization of Radon Progeny in EXO-200 Using Machine Learning Algorithms**

A Thesis  
Submitted to the Faculty  
of  
Drexel University  
by  
Erica Smith  
in partial fulfillment of the  
requirements for the degree  
of  
Doctor of Philosophy  
February 2016



© Copyright 2016  
Erica Smith.

This work is licensed under the terms of the Creative Commons Attribution-ShareAlike 4.0 International license. The license is available at  
<http://creativecommons.org/licenses/by-sa/4.0/>.

## Table of Contents

LIST OF TABLES . . . . .	v
LIST OF FIGURES . . . . .	vi
ABSTRACT . . . . .	x
1. INTRODUCTION . . . . .	1
2. NEUTRINOS . . . . .	4
2.1    History . . . . .	4
2.2    Oscillations . . . . .	5
2.3    Neutrino Mass . . . . .	9
2.3.1    Absolute Neutrino Mass . . . . .	9
2.3.2    Dirac or Majorana . . . . .	9
2.4    Neutrinoless Double Beta Decay . . . . .	10
2.4.1    Majorana Mass . . . . .	11
2.4.2 $0\nu\beta\beta$ Experiments . . . . .	13
3. EXO-200 . . . . .	16
3.1    Xenon . . . . .	16
3.2    Time Projection Chamber . . . . .	17
3.2.1    Scintillation Channel . . . . .	19
3.2.2    Ionization Channel . . . . .	20
3.2.3    Vessel . . . . .	21
3.2.4    Guide Tube . . . . .	21
3.3    Passive Shielding . . . . .	21
3.3.1    Muon Veto . . . . .	23
3.4    Assembly and Installation . . . . .	23
4. DATA HANDLING . . . . .	25

4.1	Data Acquisition System . . . . .	25
4.2	Data Preparation . . . . .	26
4.2.1	Rootification . . . . .	26
4.2.2	Reconstruction . . . . .	27
4.2.3	Processing . . . . .	27
4.3	Detector Performance . . . . .	29
4.3.1	Channel Gains . . . . .	29
4.3.2	Energy Resolution . . . . .	29
4.3.3	Electron Lifetime . . . . .	29
5.	MACHINE LEARNING . . . . .	31
5.1	Bias-Variance Tradeoff . . . . .	31
5.2	Linear Regression . . . . .	32
5.3	Decision Trees . . . . .	32
5.4	Validation Methods . . . . .	33
5.4.1	Cross-Validation . . . . .	33
5.4.2	Mean Squared Error . . . . .	34
5.4.3	Coefficient of Determination . . . . .	34
5.5	Results . . . . .	34
6.	ALPHA ION STUDIES . . . . .	38
6.1	Application of Machine Learning Techniques . . . . .	39
6.2	Coincidence Technique . . . . .	39
6.3	Ion Velocity . . . . .	40
6.4	$^{218}\text{Po}$ Ionization Fraction . . . . .	41
7.	SURFACE STUDIES . . . . .	49
7.1	Motivation . . . . .	49
7.2	Training and Testing . . . . .	50
7.3	1CC Events . . . . .	52

7.4	0CC Events . . . . .	54
7.5	Non-Uniformity . . . . .	54
	BIBLIOGRAPHY . . . . .	61

## List of Tables

2.1	Current values for $2\nu\beta\beta$ decay half-lives and limits on $0\nu\beta\beta$ decay half-lives. All $2\nu\beta\beta$ decay values obtained the National Nuclear Data Center at Brookhaven National Laboratory [76]. . . . .	12
2.2	Current and future $0\nu\beta\beta$ decay experiments. . . . .	14
7.1	Locations of 1CC events with raw scintillation counts in the range 28000-50000. Events used to investigate the Teflon reflectors are those that fall into the $20 <  z  < 172$ mm & $R > 172$ mm categories. . . . .	53
7.2	Locations for 0CC events. Events that are within $20 <  z  < 172$ mm and $R > 172$ mm categories are used to investigate the Teflon reflectors. All events have between 28000-50000 raw scintillation counts. . . . .	54

## List of Figures

2.1 Illustration of the normal and inverted hierarchies of neutrino mass states. Each mass state is composed of a mixture of the flavor states (red: $\nu_e$ , blue: $\nu_\mu$ , and green: $\nu_\tau$ . The mass splittings $\Delta m_{31}^2$ and $\Delta m_{21}^2$ are associated with atmospheric and solar neutrinos, respectively. . . . .	7
2.2 Feynman diagram of the charged current interaction. . . . .	8
2.3 Feynman diagram of the neutral current interaction. . . . .	8
2.4 Feynman diagrams of the elastic scattering interactions. . . . .	8
2.5 Change in energy for isobars with $A = 136$ . Single beta decay is energetically forbidden for $^{136}\text{Xe}$ and $^{136}\text{Ce}$ , leaving double beta decay as the only decay channel. . . . .	11
2.6 Feynman diagram for double beta decay. . . . .	11
2.7 Feynman diagram for neutrinoless double beta decay. In this model, the neutrino is a light, but massive, Majorana particle, exchanged as a virtual particle between the two nucleons. . . . .	12
2.8 Effective Majorana mass, shown here as $ <m> $ , as a function of the lightest neutrino mass state. The figure is generated using the best fit values and $2\sigma$ ranges of the current neutrino oscillation parameters. The Majorana phases $\alpha_1$ and $\alpha_2$ are varied over the range $[0, 2\pi]$ . Predictions for the normal and inverted hierarchies are labeled. Red regions correspond to at least one of the Majorana phases having a CP-violating value, whereas the blue and green areas correspond to the Majorana phases having CP-conserving values. From [80]. . . . .	13
2.9 Nuclear matrix elements for $0\nu\beta\beta$ decay candidates using the QRPA, EDF, PHFB, IBM-2, and LSSM methods. Variation between these methods leads to uncertainties in the calculation of the effective Majorana mass. From [31]. . . . .	14
2.10 Spectra of the sum of the electron kinetic energies for $2\nu\beta\beta$ decay, normalized to 1 (dotted), and $0\nu\beta\beta$ decay (solid), normalized to $10^{-2}$ ( $10^{-6}$ , inset), assuming a 5% energy resolution. From [44]. . . . .	15
3.1 Map of the Waste Isolation Pilot Plant. . . . .	16
3.2 Simplified schematic of the xenon system. Liquid xenon is heated and returns the gas phase after leaving the TPC, where it is purified before returning to the TPC. . . . .	17
3.3 TPC cutaway. [22] . . . . .	18
3.4 Cartoon schematic of the TPC. . . . .	18
3.5 Large Area Avalanche Photodiode. Ruler shows size in cm and inches. On the right: gold-plated cathode; on the left, active surface surrounded by gold-plated ring-wafer anode. . . . .	19

3.6	Panel of wires from the wire readout planes. This panel contains half of the wires for one plane [22]. . . . .	20
3.7	Geometry of the readout planes with a simulated $0\nu\beta\beta$ event. In actuality the U- and V-wire planes are rotated 60° with respect to each other. . . . .	21
3.8	TPC vessel before welding to the inside of the cryostat [22]. . . . .	22
3.9	Guide tube attached the TPC vessel, with source locations highlighted [22]. . . . .	22
3.10	The TPC being inserted into the cryostat [22]. . . . .	23
4.1	Detector readout electronics system. . . . .	25
4.2	Flowchart of the EXO-200 processing chain. . . . .	26
4.3	Anti-correlation of scintillation and ionization signals. The energy resolution is improved by using the linear combination of both signals [8]. . . . .	30
5.1	Differences between the OLS machine learned output and the truth values for the testing set. The fit is a two Gaussian fit, with the weights and $1\sigma$ values of each Gaussian shown. This algorithm does not perform as expected on the corrected scintillation counts, as the two Gaussian fit does not properly describe these results. The coefficient of determination is 0.8167. . . . .	35
5.2	Differences between the DTR machine learned output and the truth values for the testing set. The fit is a two Gaussian fit, with the weights and $1\sigma$ values of each Gaussian shown. The coefficient of determination is 0.945. . . . .	36
5.3	Differences between the Adaboosted-DTR machine learned output and the truth values for the testing set. The fit is a two Gaussian fit, with the weights and $1\sigma$ values of each Gaussian shown. Each variable must be trained and testing separately as the Adaboost method does not allow for multi-output; the coefficients of determination are: $R_x^2$ : 0.984; $R_y^2$ : 0.992; $R_{scE}^2$ : 0.952. . . . .	37
6.1	Summed electron energy for (a) single-site events and (b) multi-site events. Insert is zoomed into $0\nu\beta\beta$ decay region of interest. The vertical red lines in the SS spectrum shown the $\pm 2\sigma$ region of interest. Within the region of interest is the 2448 keV $\gamma$ line from the $^{214}\text{Bi}$ decay [35]. . . . .	38
6.2	(a) Raw (before corrections are applied) scintillation counts and (b) corrected scintillation counts versus purity corrected charge energy. Only events that are fully position reconstructed have enough information to be corrected; therefore, events that do not have a V-wire signal are not included in (b). Region A, red, corresponds to bulk $\alpha$ events; because this analysis handles events that do not have complete position reconstruction, bulk is defined as: between 28000 - 50000 raw scintillation counts, purity corrected charge energy less than 210 keV, and $20 <  z  < 172$ mm. Once corrections are applied to the scintillation counts, the populations of $^{222}\text{Rn}$ and its progeny can be seen with mean scintillation counts of 38766, 42377, and 54254 for $^{222}\text{Rn}$ , $^{218}\text{Po}$ , and $^{214}\text{Po}$ , respectively [15]. Region B, green, are $\alpha$ decays that occur on surfaces; the signal is smeared such that they are not able to be identified based on their energies. Region C, yellow, are $\beta$ and $\gamma$ decays. There is less overlap in these regions in (b) due to the light map correction, which implements an $z$ -position-dependent energy correction, allowing for a larger separation in populations of events. . . . .	42

6.3	Locations of events in region A and B as defined in Figure 6.2.	43
6.4	Radon decay chain, including half-lives of the decays. Highlighted in red are the progeny of interest for this work. Decays displayed vertically are $\alpha$ decays, and decays moving toward the right of the figure are $\beta$ decays.	44
6.5	(a) Raw scintillation counts and (b) ADTR-reconstructed corrected scintillation counts versus $z$ position of coincident pairs for events in the bulk; events assigned as $^{222}\text{Rn}$ are in red and $^{218}\text{Po}$ in black based on ordering in time. The ADTR-reconstructed corrected scintillation counts shows a reduction in the $z$ -position dependence of the scintillation energy; this lends confidence to using the ADTR method for this work.	44
6.6	$^{218}\text{Po}$ drift time versus drift distance. The population at $z = 0$ are neutral $^{218}\text{Po}$ , which do not drift a long distance before decaying. The population in $+z$ are $^{218}\text{Po}$ ions. Positive displacement is movement toward the cathode.	45
6.7	Mean velocity of $^{218}\text{Po}$ atoms and ions. Gaussian fit gives a mean ion velocity of $v = 1.153 \pm 0.42$ mm/s where the error is the $1\sigma$ value of the fit.	46
6.8	$^{218}\text{Po}$ drift time versus $^{218}\text{Po}$ drift velocity. The ion velocity decreases as the drift time increases. This points to the possibility of two ion velocities.	47
6.9	Velocity of $^{218}\text{Po}$ that passes the $\Delta t$ cut that is implemented to avoid biasing toward neutral $^{218}\text{Po}$ . This cut eliminates events that, were they charged, would have drifted out of the analysis volume. The blue area, corresponding to $v = 0.5\text{-}2.5$ mm/s, is integrated to determine the number of ions.	48
7.1	Electric current resulting from fluid flow [93].	49
7.2	Difference in ADTR-reconstructed $x$ -position and $x$ -position for 1CC events reconstructed by the EXO Analysis software. The coefficient of determination is $R_x^2$ : 0.983.	50
7.3	Difference in ADTR-reconstructed $y$ -position and $y$ -position for 1CC events reconstructed by the EXO Analysis software. The coefficient of determination is $R_y^2$ : 0.984.	51
7.4	Difference in ADTR-reconstructed $z$ -position and $z$ -position for 1CC events reconstructed by the EXO Analysis software. The coefficient of determination is $R_z^2$ : 0.998.	51
7.5	Difference in ADTR-reconstructed corrected scintillation counts and corrected scintillation counts for 1CC events reconstructed by the EXO Analysis software. The coefficient of determination is $R_{scE}^2$ : 0.949.	52
7.6	1CC events outside of the fiducial $z$ , without radial cuts applied. The accumulation of events on the cathodes and anodes is apparent here.	53
7.7	0CC events that occur outside of the region $20 <  z  < 172$ mm (a) without and (b) with the $R > 172$ mm requirement.	55
7.8	0CC events that occur within $20 <  z  < 172$ mm (a) without and (b) with the $R > 172$ mm requirement.	56
7.9	$z$ -distribution of all 1CC events with $20 <  z  < 172$ mm and $R > 172$ mm.	57

7.10 Cumulative distribution functions (CDFs) for 1CC $R > 172\text{mm}$ events in (a) TPC1 and (b) TPC2. Blue is the empirical CDF of the distribution of events in $ z $ ; green is the CDF for a uniform distribution. There is a slight deficit in events toward the cathode in both TPCs. The distribution of events along the $z$ -axis is not inconsistent with a uniform distribution in TPC1, but is inconsistent with a uniform distribution in TPC2. . . . .	58
7.11 $z$ -distribution of all 0CC events with $20 <  z  < 172 \text{ mm}$ and $R > 172 \text{ mm}$ . . . . .	59
7.12 Cumulative distribution functions (CDFs) for 0CC $R > 172\text{mm}$ events in (a) TPC1 and (b) TPC2. Blue is the empirical CDF of the data; green is the CDF for a uniform distribution. The distribution of events along the $z$ -axis is not consistent with a uniform distribution in either TPC. . . . .	60

## Abstract

Characterization of Radon Progeny in EXO-200 Using Machine Learning Algorithms

Erica Smith

Advisor: Dr. Michelle Dolinski

EXO-200 is a neutrinoless double beta ( $0\nu\beta\beta$ ) decay experiment that uses 200 kg of liquid xenon (LXe) enriched in  $^{136}\text{Xe}$ . Characterizing backgrounds is an important goal for  $0\nu\beta\beta$  decay experiments to ensure that they do not obscure a potential signal. Understanding the contribution of radon and its progeny to the background is particularly important for EXO-200 due to a  $^{214}\text{Bi}$   $\gamma$  emission in the  $0\nu\beta\beta$  decay region of interest. EXO-200 uses a combination of scintillation and ionization signals to detect events; because of this, EXO-200 has excellent particle discrimination capabilities that allow for the investigation of  $\alpha$  decays in radon chain. However,  $\alpha$  decays tend to have much smaller charge signals and often fall below the threshold for which we can reconstruct the positions of events, particularly events that occur close to the walls of the LXe vessel. Without position information it is not possible to characterize the events near the walls. Investigating these events is important to determine if ions are clustering on or near the walls, which could point to charging up of the plastics inside the LXe vessel or a “hotspot” on the plastic due to contamination during cleaning and installation. In this work we implement machine learning algorithms to reconstruct the positions of events that are not reconstructed by the existing analysis framework. We verify the validity of this method by measuring the ion velocity and ionization fraction of  $^{218}\text{Po}$  produced by the  $^{222}\text{Rn}$   $\alpha$  decay. With the method verified, we reconstruct the positions of events with no charge information and investigate events on the detector walls.



## Chapter 1: Introduction

Since the neutrino was initially postulated in 1930 [81], the particle physics community has made great strides in determining its characteristics. At the time, there was an emergency in the field; it appeared that energy and momentum were not conserved in beta decay. The neutrino came about as a desperate attempt to explain why electrons were not carrying away the full energy of the decay. When it was introduced, it was thought to be a neutral, massless particle that would never be detected. Discovered experimentally in 1956 [88], neutrinos finally found their way into the Standard Model, still as neutral, massless particles. Over time, we would find that neutrinos come in three flavors – electron, muon [36], and tau [40] – and interestingly, that they oscillate between these flavors as they travel through space [48], [11]. Experiments dedicated to studying neutrino oscillations show that flavor oscillation is due to flavor states being a linear combination of the mass states – meaning that neutrinos must be massive particles! This is especially intriguing as there is nothing in the Standard Model that suggests that this must be true.

Neutrino oscillation experiments have given us a great deal of information about neutrinos, but we cannot learn all we want to know through these experiments alone. While they are able to shed light on the mass squared differences between the different neutrino mass states, as well as the parameters that determine how the neutrinos mix as they travel [42], they are unable to provide information about the absolute mass and quantum nature of neutrinos. All charged leptons are Dirac particles; that is, the particle and anti-particle are two distinct states. However, since the neutrino is neutral, it is theoretically possible for it to be a Majorana particle; that is, the neutrino and anti-neutrino are the same particle. Double beta decay experiments may be able to shed light on these issues.

Double beta decay ( $2\nu\beta\beta$ ) is the primary decay mode for even-even nuclides when beta decay is energetically forbidden or suppressed by a large change in angular momentum; this is possible in 35 naturally-occurring isotopes and has been observed in 11. In this decay, two neutrons are converted to protons, and two electrons and two electron anti-neutrinos are emitted. Not long after double beta decay was theorized [51], it was also theorized that double beta decay would occur whether neutrinos were Dirac or Majorana, and if neutrinos were Majorana, neutrinoless double beta ( $0\nu\beta\beta$ ) decay would occur [49]; that is, the decay would occur with only electrons as the products, and no neutrino emission. Observation of this decay mode would definitively show that neutrinos are Majorana particles.

Assuming the neutrino is a Majorana particle and that light Majorana neutrino exchange is the dominant mechanism by which  $0\nu\beta\beta$  decay occurs, it is possible to probe the absolute neutrino mass with double beta decay experiments. The neutrino mixing matrix, which dictates how neutrinos oscillate, relates the Majorana neutrino mass to the absolute neutrino mass. The Majorana mass is related to the  $0\nu\beta\beta$  half-life by a phase factor and nuclear matrix element. Therefore, determining a  $0\nu\beta\beta$  half-life would allow for the determination of the absolute neutrino mass.

EXO-200, the Enriched Xenon Observatory, is a double beta decay experiment that utilizes 200kg of liquid xenon (LXe) isotopically enriched in  $^{136}\text{Xe}$  in a dual time projection chamber (TPC) setup, with scintillation and ionization readouts to measure the energy of the decay electrons. The experiment is located approximately one half mile underground at the Waste Isolation Pilot Plant (WIPP) in Carlsbad, New Mexico, USA. EXO-200 made the first observation of  $2\nu\beta\beta$  in 2011 [8], and has since made the most precise  $2\nu\beta\beta$  half-life measurement,  $T_{1/2}^{2\nu\beta\beta} = 2.172 \pm 0.017 \text{ stat} \pm 0.060 \text{ sys} \times 10^{21} \text{ years}$  [12]. EXO-200 also has measured the lower limit of the  $0\nu\beta\beta$  half-life to be  $T^{1/2,0\nu} = 1.1 \times 10^{25}$  at 90% CL [35]. This corresponds to a Majorana mass of 190-450 meV, depending on the nuclear matrix element used.

There are many double beta decay experiments currently running, using a variety of isotopes, including  $^{76}\text{Ge}$ ,  $^{136}\text{Xe}$ , and  $^{130}\text{Te}$ . Previous experiments have not seen a  $0\nu\beta\beta$  signal, though a portion of the Heidelberg-Moscow collaboration has claimed to make an observation using  $^{76}\text{Ge}$  [66],

[65], [68], [67]. However, the result is considered to be suspect and is disfavored by current limits set with  $^{136}\text{Xe}$  and  $^{76}\text{Ge}$  [10]. Future experiments are being developed to scale up the amount of isotope used; the next generation experiments are expected probe masses within the inverted hierarchy.

While the observation of  $0\nu\beta\beta$  is the primary physics goal of EXO-200, there is opportunity for many other robust analyses. Having low backgrounds is a requirement to be able to observe  $0\nu\beta\beta$ , and though the detector was constructed with low radioactivity material, there is sufficient  $^{222}\text{Rn}$  in the LXe to study its decay progeny. Due to the dual energy readout of the detector, we are able to identify alpha decays with ease, as alpha decays have high scintillation energy and a relatively low ionization energy due to a higher initial electron density, which leads to recombination before the electrons are collected; in contrast, beta and gamma decays have a high ionization energy with a relatively low scintillation energy, making alpha decays easily distinguishable. However, the EXO-200 hardware is optimized for detection of beta decays. The ionization energies of the alpha decays often fall into a range that is below the energy threshold of the charge collection plane. Because of this, the full position of the event is unable to be reconstructed for many alpha events.

By capitalizing on our ability to study individual alpha decays and match them in time and position to other alpha or beta decays, studies can be done on  $^{222}\text{Rn}$  and its progeny, specifically  $^{218}\text{Po}$ . Using a coincidence technique to associate  $^{222}\text{Rn}$  and  $^{218}\text{Po}$  decays, it is possible to comment on the characteristics of the  $^{218}\text{Po}$ , such as its average drift velocity, and the fraction of  $^{218}\text{Po}$  daughters that are ionized. Combining these measurements with studies previously done on the  $^{214}\text{Bi}$ - $^{214}\text{Po}$  decay, the  $\beta$  ionization fraction for the  $^{214}\text{Pb}$ - $^{214}\text{Bi}$  beta decay can be calculated.

Ions behave differently on the surfaces of the detector (i.e., the cathodes, anodes, Teflon surfaces) than in the bulk liquid xenon, away from the surfaces. In particular, these events tend to have a lower scintillation energy, and many do not have any charge information reconstructed by the EXO analysis software. It is also unclear how long the ions stay on the surfaces. It is interesting to investigate whether these ions cluster in a particular pattern on the surfaces, which could point to charging of the Teflon surfaces.

In this work I examine using machine learning algorithms as a potential method to improve the EXO-200 alpha decay investigation, as well as the application of these techniques to investigating surface events. Machine learning is a field of study that gives computers the ability to learn without explicitly being programmed. Supervised learning is a subset of these algorithms which involves training the machine with the “truth values,” whereas unsupervised learning is a set of algorithms in which the data is supplied to the machine and it forms patterns on its own. Supervised learning algorithms can be classification, in which there is discrete output, or regression, in which there is continuous output. Unsupervised learning can be clustering, in which the data set is supplied and the machine finds concentrations of points, or dimensionality reduction, in which high dimensional data is reduced to fewer dimensions, which is generally used for data visualization.

Though the EXO reconstruction is unable to reconstruct all alpha events, there is still a portion for which the position is fully reconstructed. Using scintillation information and the reconstructed position of these fully reconstructed events as truth values, the algorithm is able to predict the event location for unreconstructed events based on their scintillation information. By increasing the number of events for which there is full position reconstruction, we allow for the inclusion of these events into low statistics analyses, such as the alpha ion analysis. In this work I present  $^{218}\text{Po}$  ion velocity and ionization fraction with the increased data set, as well as the recalculation of the ionization fraction of  $^{214}\text{Bi}$  using these values.

There also exists a set of events for which there is a scintillation signal, but no charge signal is reconstructed. A lack of charge signal necessarily means that there is no 3D position information available for the event due to the way event position is reconstructed in the EXO Analysis framework. Therefore, without an outside method to reconstruct these positions, these events cannot be investigated. In this work I apply the machine learning predictions to these events so that the detector walls can be studied. These events are thought to be alpha decays that occur on or close enough to the walls of the vessel that this proximity disrupts the ionization cloud such that the charge energy falls below the detection threshold of the U-wires. If these events are distributed in a non-uniform way, this may point to ions clustering on the Teflon due to charging of the plastics in the detector or a portion of the Teflon that may have been contaminated during cleaning and

installation.

## Chapter 2: Neutrinos

With the 2015 Nobel Prize being awarded to members of SuperKamiokande and the Sudbury Neutrino Observatory for the discovery of neutrino oscillations and neutrino mass, it is hard to believe that it was not even a century ago that physicists did not know of the existence of the neutrino. While the field of neutrino physics has grown significantly in a short period of time, there are still a few unknowns to be discovered. In this chapter I discuss the history of neutrino physics and some of the future prospects of the field.

### 2.1 History

Beta decay is the transition of a down quark of a neutron to an up quark, converting it to a proton and resulting in the emission of an electron and an electron anti-neutrino. However, in the 1920s, physicists expected that the electron was the only emitted particle from  $\beta$ - decay; because this was considered to be a two-body decay, the energy spectrum was expected to be discrete. This was not what was observed experimentally; instead, a continuous spectrum was observed. Physicists were unable to explain this phenomenon and even began to consider the possibility that energy was not conserved in  $\beta$ - decay.

In 1930, Wolfgang Pauli made what he referred to as a "desperate attempt" to show that energy conservation was not being violated by suggesting there was a second particle emitted from  $\beta$  decay which was carrying away the missing energy. He believed this particle to be a neutral, spin-1/2 particle that was about the same mass as the electron. However, Pauli also believed that this particle, which he, at the time, called the neutron, would be impossible to detect [81]. By the time of Fermi's development of  $\beta$  decay theory in 1934 [46], the neutron had been discovered [34], and Fermi had renamed Pauli's particle the "neutrino," meaning "little neutral one."  $\beta^-$  and  $\beta^+$  decay was adjusted to include neutrinos,

$$(A, Z) \rightarrow (A, Z + 1) + e^- + \bar{\nu},$$

$$(A, Z) \rightarrow (A, Z - 1) + e^+ + \nu,$$

where A is mass number, Z is atomic number,  $e^-$  is the electron,  $e^+$  is the positron,  $\nu$  is the neutrino, and  $\bar{\nu}$  is the antineutrino.

Luckily, neutrino detection was not impossible as Pauli had feared, and in 1956, Clyde Cowan and Frederick Reines published the first neutrino detection from a nuclear reactor as a result of studying inverse beta decay [88],

$$\bar{\nu}_e + p \rightarrow n + e^+.$$

To do so, they initially used a detector with protons in a hydrogenous liquid scintillator, which was doped with cadmium, but high background from cosmic rays and the nuclear reactor prevented an actual measurement. The second attempt included what was referred to as a "club sandwich" approach, in which the "bread" layers were scintillation detectors equipped with photomultiplier tubes (PMTs), and the "meat" layers were neutrino targets, consisting of cadmium chloride mixed with water. The detector was then enclosed with a paraffin and lead shield and placed in an underground room in the reactor building, providing shielding from the reactor neutrons and cosmic ray backgrounds. With this setup, they were able to observe inverse beta decay when anti-neutrinos interacted with the protons in the water, producing neutrons and positrons; the resulting positrons immediately annihilate with electrons, which produces gammas. The neutron is subsequently captured by an appropriate nucleus - in this case, cadmium - which also produces gammas. This signature serves as a positive neutrino detection.

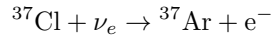
The muon neutrino was discovered in 1962 at Brookhaven National Laboratory [36] as a result of pion decay:

$$\pi^+ \rightarrow \mu^\pm + (\nu/\bar{\nu})$$

and the realization that the neutrino observed produced muons, but not electrons, led to the conclusion that this was a new, second type of neutrino. Once the tau was discovered, it seemed to follow that there would be an associated neutrino, which was discovered by the DONUT collaboration [40] by observing tau decay.

## 2.2 Oscillations

In the 1960s, the Standard Solar Model was being developed, and that model showed that there was a measurable flux of solar neutrinos from  ${}^8\text{B}$  decay from nuclear fusion in the interior of the sun [26]. To test this, Raymond Davis [38] set up an experiment at the Homestake gold mine in Lead, South Dakota. The detector was set up 4850 feet underground (4400 m.w.e.) and consisted of a horizontal cylindrical tank containing 390,000L of liquid tetrachloroethylene  $\text{C}_2\text{Cl}_4$  (520 tonnes of Cl). The electron neutrino was to interact with the chlorine to produce radioactive argon:



Based on calculations performed by John Bahcall [26], it was estimated that there would be 2-7 solar neutrino captures per day for 520 tonnes of chlorine.

Neutrinos were not detected directly but instead by extracting the resulting  ${}^{37}\text{Ar}$ ; the argon, which has a 35 day half-life, was then counted as it decayed. The observed flux from this experiment was a factor of 3 below the expected rate [38].

The initial reaction to the Homestake experiment was to alter the Standard Solar Model [25]. However, based on the energy spectrum of neutrinos from the sun, there was no way to change the model that would reconcile the differences between the observed and expected neutrino fluxes [54]. Initially the reduction in fluxes from  ${}^7\text{Be}$  and  ${}^8\text{B}$  were achieved by lowering the temperature of the sun in the Standard Solar Model, but in order to achieve the proper ratio of these fluxes, the temperature needed to be higher. Inability to explain the results of the Homestake experiment through altering the Standard Solar Model cast doubt on the validity of these results.

Results from SAGE [5], GALLEX [17], and Kamiokande II/III [55] also reported a deficit in the observed neutrino flux. SAGE and GALLEX, located in Baksan Neutrino Observatory in Mount Andyrchi in the Caucasus and Gran Sasso National Laboratory in Italy, respectively, were radiochemical experiments that used gallium, specifically looking at the reaction  ${}^{71}\text{Ga} + \nu_e \rightarrow {}^{71}\text{Ge} + \text{e}^-$ .

Kamiokande II was the first non-radiochemical measurement of the neutrino flux. The Kamioka Nucleon Decay Experiment, the predecessor to Kamiokande II, was a water Cherenkov detector located in the Kamioka mine in Japan, originally dedicated to measure proton decay. It was refigured as a neutrino detector in the successive experiments, operating by measuring Cherenkov light from neutrino-electron recoils [55]. Using data from 1987 to 1990, Kamiokande II provided the first direct measurement of the production of solar neutrinos by showing a directional correlation of solar-neutrino-induced electron events with respect to the sun. When measuring the flux of  ${}^8\text{B}$  solar neutrinos, they showed that the neutrino flux was only about one-half of the flux predicted by Bahcall, which was also in contention with the flux found by the Homestake Experiment. The conclusion was that it was difficult to resolve both flux measurements by altering the Standard Solar Model, and that perhaps the difference from the expectation was an intrinsic characteristic of the neutrino [56].

In 1957-1958, Bruno Pontecorvo first postulated that neutrinos may oscillate in a similar manner to neutral kaons [84]. Though the muon neutrino had not yet been discovered, so neutrino flavors had not been considered, Pontecorvo suggested that it was possible for a neutrino to oscillate into an anti-neutrino [83]. He suggested that neutrino composition may change on the journey from the reactor to the detector, and commented that Cowan and Reines should perform their experiment

with detectors at different distances. In 1967, after the discovery of muon neutrinos, Pontecorvo considered that electron neutrinos could oscillate into muon neutrinos and vice versa [85].

Mako, Nakagawa, and Sakata were also working on a way to relate neutrino masses to neutrino flavors. At the time, only two flavors of neutrinos were known; the neutrino mass states 1 and 2 were suggested to be the orthogonal combination of the flavor states  $e$  and  $\mu$  [72]. In the case of only two states this relation is

$$\begin{aligned}\nu_e &= \nu_1 \cos(\theta) + \nu_2 \sin(\theta) \\ \nu_\mu &= -\nu_1 \sin(\theta) + \nu_2 \cos(\theta)\end{aligned}\quad (2.1)$$

Once the tau was discovered it was also assumed that there would be a related neutrino; the mixing matrix that maps the rotation from the mass states to the flavor states was then expanded. In the three-neutrino picture, the flavor and mass eigenstates are related by:

$$\begin{aligned}|\nu_\alpha\rangle &= \sum_i U_{\alpha i}^* |\nu_i\rangle \\ |\nu_i\rangle &= \sum_\alpha U_{\alpha i} |\nu_\alpha\rangle\end{aligned}\quad (2.2)$$

where  $\alpha = e, \mu, \tau$  are the flavor indices and  $i = 1, 2, 3$  are the indices for the mass eigenstates. The mixing matrix  $U_{\alpha i}$ , now called the PMNS matrix, is as follows:

$$\begin{aligned}U &= \begin{bmatrix} U_{e1} & U_{e2} & U_{e3} \\ U_{\mu 1} & U_{\mu 2} & U_{\mu 3} \\ U_{\tau 1} & U_{\tau 2} & U_{\tau 3} \end{bmatrix} \\ &= \begin{bmatrix} 1 & 0 & 0 \\ 0 & c_{23} & s_{23} \\ 0 & -s_{23} & c_{23} \end{bmatrix} \begin{bmatrix} c_{13} & 0 & s_{13}e^{-i\delta} \\ 0 & 1 & 0 \\ -s_{13}e^{i\delta} & 0 & c_{13} \end{bmatrix} \begin{bmatrix} c_{12} & s_{12} & 0 \\ -s_{12} & c_{12} & 0 \\ 0 & 0 & 1 \end{bmatrix} \begin{bmatrix} e^{i\alpha_1/2} & 0 & 0 \\ 0 & e^{i\alpha_2/2} & 0 \\ 0 & 0 & 1 \end{bmatrix} \\ &= \begin{bmatrix} c_{12}c_{13} & s_{12}c_{13} & s_{13}e^{-i\delta} \\ -s_{12}c_{23} - c_{12}s_{23}s_{13}e^{i\delta} & c_{12}c_{23} - s_{12}s_{23}s_{13}e^{i\delta} & s_{23}c_{13} \\ s_{12}s_{23} - c_{12}c_{23}s_{13}e^{i\delta} & -c_{12}s_{23} - s_{12}c_{23}s_{13}e^{i\delta} & c_{23}c_{13} \end{bmatrix} \begin{bmatrix} e^{i\alpha_1/2} & 0 & 0 \\ 0 & e^{i\alpha_2/2} & 0 \\ 0 & 0 & 1 \end{bmatrix}\end{aligned}$$

where  $s_{ij}$  and  $c_{ij}$  stands for  $\sin \theta_{ij}$  and  $\cos \theta_{ij}$ , respectively [30]. The phase  $\delta$  is a CP-violating phase, which will be nonzero only if there is CP violation. The phases  $\alpha_1$  and  $\alpha_2$  are Majorana phases, which cannot be measured in neutrino oscillation experiments. These phases can be calculated with the observation of lepton-number violating processes such as neutrinoless double beta decay.

Returning to the simpler two neutrino mixing from equation 2.1 which expresses the flavor states as a linear combination of the mass states, and expressing the propagation of the neutrino as  $\nu(t) = e^{-iE_i t} \nu(0)$ , we find that the probability of a neutrino of flavor  $\alpha$  oscillating to a neutrino of flavor  $\beta$  is

$$\begin{aligned}P(\nu_\alpha \rightarrow \nu_\beta) &= \langle \nu_\beta(0) | \nu_e(t) \rangle \\ &= \sin^2(\theta) \cos^2(\theta) |e^{-iE_2 t} - e^{-iE_1 t}|^2 \\ &= \sin^2(2\theta) \sin^2 \left( 1.27 \Delta m^2 \frac{L}{E} \right).\end{aligned}\quad (2.3)$$

Equation 2.3 is the standard oscillation equation for any two neutrino mixing. The parameter  $\theta$  is the mixing angle, which defines the amplitude of the oscillation; a value of zero would imply that there are no oscillations. The parameter  $\Delta m^2$  is the the mass squared difference between two states; that is,  $\Delta m_{ij}^2 = m_i^2 - m_j^2$  eV<sup>2</sup>. The propagation of the oscillation is determined by  $L/E$ , where  $L$  is the distance from the neutrino source to the detector in km, and  $E$  is the energy of the neutrino in

GeV.

The current values for the neutrino oscillation parameters, from the Particle Data Group (PDG) [80], are:

- $\sin(2\theta_{13}) = 0.085 \pm 0.005$  (PDG average of Daya Bay, Double Chooz, RENO)
- $\sin(2\theta_{12}) = 0.846^{+0.021}_{-0.021}$  (KamLAND, solar, reactor, and accelerator data)
- $\sin^2(2\theta_{23}) = 0.999^{+0.001}_{-0.018}$  (T2K)
- $\Delta m_{21}^2 = 7.53 \pm 0.18 \times 10^{-5} \text{ eV}^2$  (KamLAND, solar, reactor, and accelerator data)
- $|\Delta m_{32}^2| = 2.49 \pm 0.06 \times 10^{-3} \text{ eV}^2$  if inverted mass hierarchy and  $|\Delta m_{32}^2| = 2.42 \pm 0.06 \times 10^{-3} \text{ eV}^2$  if normal hierarchy (PDG fit)

Still unknown are the CP violating phase  $\delta$ , the Majorana phases  $\alpha_1$  and  $\alpha_2$ , the sign of  $\Delta m_{32}^2$ , and the absolute neutrino masses. The uncertainty on the sign of  $\Delta m_{32}^2$ , that is, whether  $m_3$  is the largest or smallest mass eigenstate, leads to the different mass hierarchies shown in Figure 2.1.

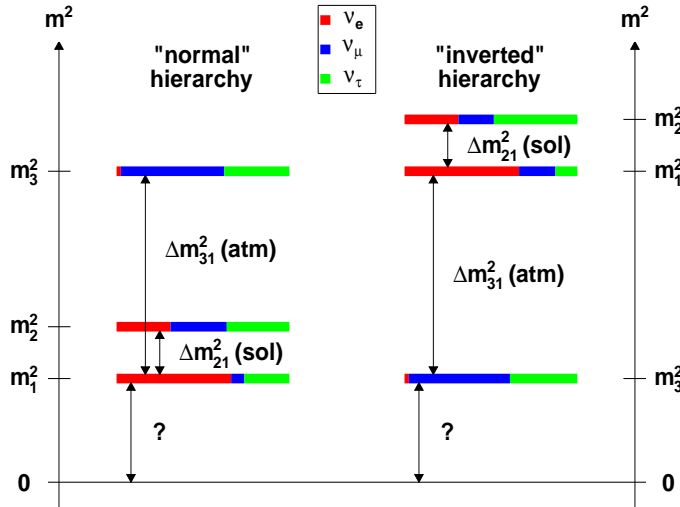


**Figure 2.1:** Illustration of the normal and inverted hierarchies of neutrino mass states. Each mass state is composed of a mixture of the flavor states (red:  $\nu_e$ , blue:  $\nu_\mu$ , and green:  $\nu_\tau$ ). The mass splittings  $\Delta m_{31}^2$  and  $\Delta m_{21}^2$  are associated with atmospheric and solar neutrinos, respectively.

The first experimental indication of neutrino oscillation arose in 1998 from the SuperKamiokande experiment. SuperKamiokande, the successor to the Kamiokande experiments, began measuring the atmospheric neutrino flux in 1996 and announced first evidence of neutrino oscillation in 1998; specifically, their data were consistent with two-flavor  $\nu_\mu \leftrightarrow \nu_\tau$  oscillations at 90% confidence level [48]. In 2001, Sudbury Neutrino Observatory measured interactions of electron neutrinos with heavy water, produced by  ${}^8\text{B}$  solar neutrinos [11]. The solar neutrinos interact via the reactions

$$\begin{array}{ll} \nu_e + d \rightarrow p + p + e^- & \text{charged current, Figure 2.2} \\ \nu_x + d \rightarrow p + n + \nu_x & \text{neutral current, Figure 2.3} \\ \nu_x + e^- \rightarrow \nu_x + e^- & \text{elastic scattering, Figure 2.4.} \end{array}$$

where the subscript  $x$  indicates that this can be any flavor of neutrino. The charged current interaction is only sensitive to electron neutrinos, whereas the neutral current interaction is sensitive to

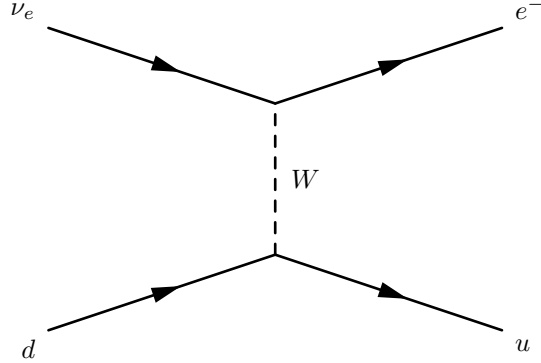


**Figure 2.2:** Feynman diagram of the charged current interaction.

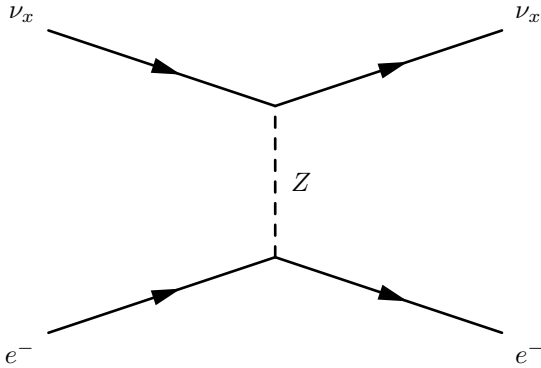


**Figure 2.3:** Feynman diagram of the neutral current interaction.

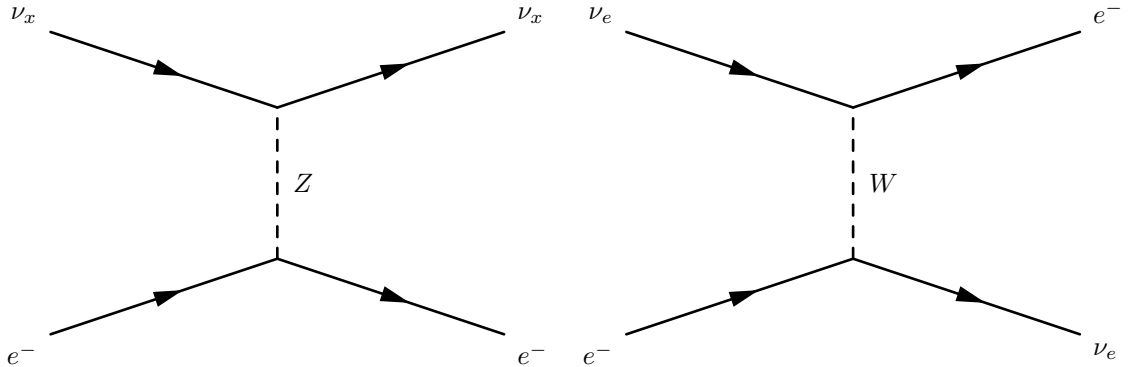


**Figure 2.4:** Feynman diagrams of the elastic scattering interactions.

all active flavors of neutrinos and the elastic scattering reaction is sensitive to all active flavors but with a reduced sensitivity to the muon and tau flavors. SNO compared the electron neutrino flux from the charged current interaction and the deduced  ${}^8\text{B}$  flux preserved from the elastic scattering reaction [11]. If there were no oscillations, the flux from the elastic scattering should have been equal to that from the charged current interaction since all  ${}^8\text{B}$  solar neutrinos are produced as electron neutrinos. However, SNO observed a significantly smaller flux from the charged current interaction

than the flux from the elastic scattering, which is consistent with neutrinos oscillating into other active flavors. The total flux, determined from the elastic scattering reaction, was determined to be in good agreement with the predictions from the Standard Solar Model [11].

In 2008, KamLAND rejected the no-oscillation hypothesis at  $> 5\sigma$  [7], all but confirming the existence of neutrino oscillations; they were officially confirmed by the T2K collaboration in 2014, with the observation of electron neutrino appearance in a muon neutrino beam [6].

## 2.3 Neutrino Mass

While oscillation experiments have demonstrated that neutrinos are massive particles, they are unable to determine the absolute neutrino mass. They are also not sensitive to the quantum nature of neutrinos, that is, whether they are Dirac or Majorana particles.

### 2.3.1 Absolute Neutrino Mass

While there has not yet been a measurement of the absolute neutrino mass, there have been upper limits from experiments that measure the endpoint region of the tritium  $\beta$  decay spectrum, as well as cosmological limits on the sum of the neutrino masses.

Limits from the tritium  $\beta$  decay experiments Mainz [69] and Troitsk [21] are

$$m_\beta \leq 2.3 \text{ eV (Mainz)}, \quad m_\beta \leq 2.1 \text{ eV (Troitsk)}$$

where  $m_\beta$  is an average neutrino mass, defined as

$$m_\beta^2 = \sum_i |U_{ei}|^2 m_i^2. \quad (2.4)$$

The KATRIN collaboration hopes to improve on these measurements with up to 10kg/yr gaseous tritium; KATRIN will be sensitive to a neutrino mass of 0.2 eV [89]. Recent cosmological limits from *Planck* constrain the sum of neutrino masses to  $\Sigma_\nu < 0.23$  eV [9].

### 2.3.2 Dirac or Majorana

In 1928, Dirac derived a relativistic wave equation that describes all spin-1/2 massive particles [39], given here in natural units

$$i\partial^\mu\psi - m\psi = 0 \quad (2.5)$$

where  $\psi$  is a Dirac spinor,  $\partial^\mu$  is the derivative including the gamma matrices and a summation of the individual spinor components, and  $m$  is the rest mass of the particle. Dirac particles are distinct from their antiparticles.

In 1937, Ettore Majorana suggested that neutral spin-1/2 particles can be described by an equation which is similar to equation 2.5 but includes the charge conjugate of the spinor [71]

$$-i\partial^\mu\psi + m\psi_c = 0. \quad (2.6)$$

Here  $\psi$  is a Majorana spinor,  $\psi_c$  is the charge conjugate of  $\psi$ , and  $m$  is the Majorana mass. The field  $\psi$  must be neutral or it will violate charge conservation. It is important to note that  $\psi = \psi_c$  and so a Majorana particle is its own antiparticle. Particles which are described by the Majorana spinor are called Majorana particles. Being electrically neutral, neutrinos with definite mass may be Dirac or Majorana fermions; this distinction cannot be made with the current knowledge of neutrinos.

Neutrinos are assumed to be massless in the Standard Model (SM); for this case, the SM contains the left-handed field  $\nu_L$  which couples to the  $W$  and  $Z$  bosons. However, the SM can be extended to include neutrino masses in the same way that quark masses are handled, which includes a  $\nu_R$  term. This leads to the construction of the Dirac mass term [42]

$$\mathcal{L}_{Dirac} = -m_D \bar{\nu}_L \nu_R + \text{h.c.} \quad (2.7)$$

where  $m_D$  is the Dirac mass, which couples the left-handed and right-handed neutrino. This term conserves lepton number  $L$ , defined by  $L(\nu) = L(\ell^-) = -L(\bar{\nu}) = -L(\ell^+) = 1$ . When  $L$  is conserved, neutrinos are distinct from anti-neutrinos, as their lepton numbers are different. Once  $\nu_R$  is added to the SM, a Majorana mass term can be constructed:

$$\mathcal{L}_{Majorana} = -m_R \bar{\nu}_R^c \nu_R + \text{h.c.} \quad (2.8)$$

where  $m_R$  is the Majorana mass and  $\nu_R^c$  is the charge conjugate of  $\nu_R$ . This process does not conserve lepton number, and therefore leaves no way to distinguish a neutrino from its anti-particle. Neither of these terms are excluded by symmetry, if lepton number conservation is not required, and so it is possible that Majorana masses exist in nature.

The seesaw mechanism [74], [92], an attractive explanation for neutrino masses being lighter than other known fermions, requires both Dirac and Majorana terms. In this mechanism, a large Majorana mass term splits a Dirac neutrino into two Majorana neutrinos. The relationship between the Dirac and Majorana neutrinos is

$$m_\nu m_N \approx m_D^2 \quad (2.9)$$

where  $m_\nu$  are the observed light neutrinos and  $m_N$  are heavy partners to these neutrinos that have yet to be observed.

The Majorana nature of neutrinos can be observed in processes where the lepton number changes by two units; double beta decay allows for this, and the observation of neutrinoless double beta decay would not only show that lepton number is not conserved, but may also provide information on the absolute scale of neutrino masses [80].

## 2.4 Neutrinoless Double Beta Decay

Double beta decay is a rare, second-order process in which two neutrons are converted to two protons and two electrons and two electron anti-neutrinos are emitted. For (double) beta decay to occur, the resulting nucleus must have a lower energy than the original nucleus. Due to spin-coupling, an even- $A$  nucleus with equal spin-up and spin-down nucleons, occurring for even- $Z$ , even- $N$  isobars, will have a lower energy than isobars with odd  $Z$  and odd  $N$ . This occurs, for example, in isobars of  $A = 136$ , shown in Figure 2.5.  $^{136}\text{Xe}$  has a lower energy than  $^{136}\text{Cs}$ , so single beta decay in this case is forbidden. However,  $^{136}\text{Ba}$  has a lower energy than  $^{136}\text{Xe}$ , and therefore  $^{136}\text{Xe}$  can double beta decay.

Double beta decay was first theorized in 1935 by Goeppert-Mayer [51], as

$$(A, Z) \rightarrow (A, Z + 2) + 2e^- + 2\bar{\nu}.$$

The Feynman diagram is given in Figure 2.6. Inghram and Reynolds made the first indirect detection of  $2\nu\beta\beta$  decay in 1950, using  $^{130}\text{Te}$  [62], with a geochemical approach in which they separated the resulting xenon from minerals and analyzed the isotopes. Detecting an excess of  $^{130}\text{Xe}$  showed that there was a  $2\nu\beta\beta$  decay and allowed for the calculation of the half-life, which was determined to be  $T_{1/2}^{^{130}\text{Te}} = 1.4 \times 10^{21}$  years. The first measurement of  $2\nu\beta\beta$  decay in the laboratory was with  $^{82}\text{Se}$  in 1987 [43], using a time projection chamber. This experiment found the half-life to be  $T_{1/2}^{^{82}\text{Se}} = 1.1_{-0.3}^{+0.8} \times 10^{20}$  yr.

Since then the  $2\nu\beta\beta$  decay half-life has been determined for many of the isotopes for which  $2\nu\beta\beta$  is possible, shown in Table 2.1.

Shortly after  $2\nu\beta\beta$  decay was theorized, Majorana suggested that there is no change to the  $\beta$  theory if neutrinos are Majorana particles [71]. In 1939, Furry [49] considered the idea that  $0\nu\beta\beta$  decay could happen with electron emission only, and no neutrino emission, as represented in Figure 2.7

$$(A, Z) \rightarrow (A, Z + 2) + 2e^-.$$

In this process the initial nucleus emits an electron and goes into a virtual intermediate state, releas-

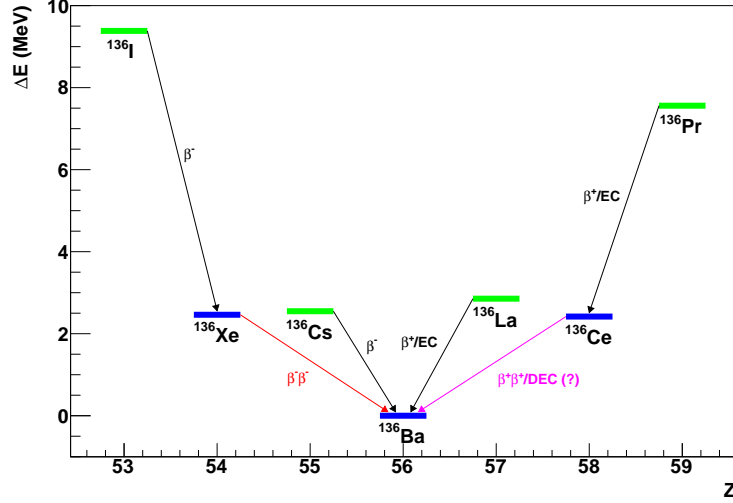


**Figure 2.5:** Change in energy for isobars with  $A = 136$ . Single beta decay is energetically forbidden for  $^{136}\text{Xe}$  and  $^{136}\text{Ce}$ , leaving double beta decay as the only decay channel.

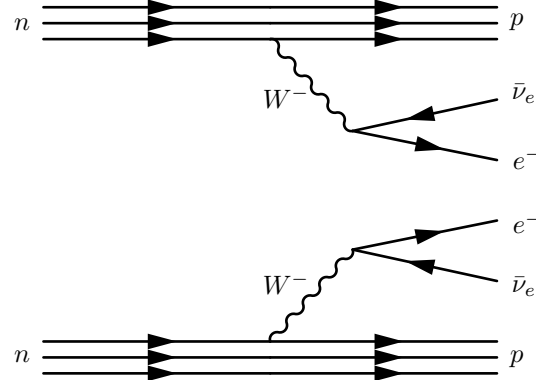


**Figure 2.6:** Feynman diagram for double beta decay.

ing an antineutrino, which then, since it is a Majorana particle, is absorbed into the intermediate nucleus as a neutrino, causing the nucleus to decay and release a second electron. This process violates lepton number conservation and requires that neutrinos have a Majorana mass term. Observation of  $0\nu\beta\beta$  decay would provide conclusive evidence that neutrinos are Majorana particles.

#### 2.4.1 Majorana Mass

If neutrinos are confirmed to be Majorana particles, it may be possible to measure the Majorana mass. The decay rate depends on the lepton number violating parameter; for the exchange of a light but massive virtual neutrino, as shown in Figure 2.7, this parameter is the effective Majorana mass. However, this is not the only possible mechanism by which  $0\nu\beta\beta$  decay may occur; it is possible that  $0\nu\beta\beta$  decay occurs with the exchange of a heavy particle, which may not necessarily be a neutrino [59], [58], [57]. The lepton number violating parameter differs for each of these mechanisms [24].

We continue, here, with the assumption that  $0\nu\beta\beta$  decay involves the exchange of a light neutrino. If this is the case, the effective Majorana mass is related to the  $0\nu\beta\beta$  decay rate by

$$[T_{1/2}^{0\nu}]^{-1} = G(Q, Z)|M(Z, A)|^2 \langle m_{\beta\beta} \rangle^2 \quad (2.10)$$

**Table 2.1:** Current values for  $2\nu\beta\beta$  decay half-lives and limits on  $0\nu\beta\beta$  decay half-lives. All  $2\nu\beta\beta$  decay values obtained the National Nuclear Data Center at Brookhaven National Laboratory [76].

Isotope	Q-value (keV)	$T_{1/2}^{2\nu\beta\beta}$ (yr)	$T_{1/2}^{0\nu\beta\beta}$ (yr, 90% CL)
$^{48}\text{Ca}$	4267.0	$(4.39 \pm 0.58) \times 10^{19}$	$>1.4 \times 10^{22}$ [79]
$^{76}\text{Ge}$	2039.06	$(1.43 \pm 0.53) \times 10^{21}$	$>2.1 \times 10^{25}$ [10]
$^{82}\text{Se}$	2996.4	$(9.19 \pm 0.76) \times 10^{19}$	$>1.0 \times 10^{23}$ [20]
$^{96}\text{Zr}$	3349.0	$(2.16 \pm 0.26) \times 10^{19}$	$>9.2 \times 10^{21}$ [19]
$^{100}\text{Mo}$	3034.37	$(6.98 \pm 0.44) \times 10^{18}$	$>4.6 \times 10^{23}$ [20]
$^{116}\text{Cd}$	2813.44	$(2.89 \pm 0.25) \times 10^{19}$	$>1.6 \times 10^{22}$ [28]
$^{130}\text{Te}$	2527.51	$(7.14 \pm 1.04) \times 10^{20}$	$>4.0 \times 10^{24}$ [50]
$^{136}\text{Xe}$	2457.99	$(2.34 \pm 0.13) \times 10^{21}$	$>1.1 \times 10^{25}$ [23]
$^{150}\text{Nd}$	3371.38	$(8.37 \pm 0.45) \times 10^{18}$	$>1.8 \times 10^{22}$ [18]

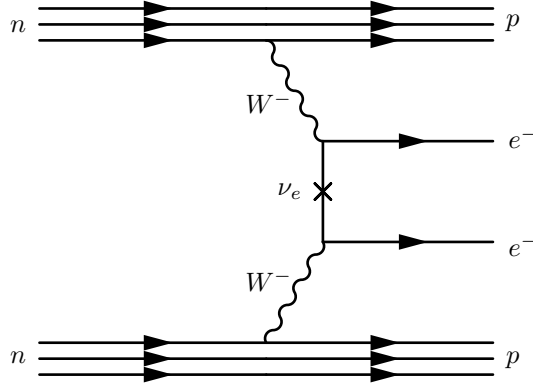


**Figure 2.7:** Feynman diagram for neutrinoless double beta decay. In this model, the neutrino is a light, but massive, Majorana particle, exchanged as a virtual particle between the two nucleons.

where  $G$  is a phase space factor that depends on the nucleus and the decay endpoint of the isotope,  $M(Z, A)$  is the nuclear matrix element, which depends on the nucleus and the model used, and  $\langle m_{\beta\beta} \rangle$  is the effective Majorana mass given by

$$|m_{\beta\beta}| = |\sum_i m_i U_{ei}^2| \quad (2.11)$$

where  $m_i$  are the neutrino mass states and  $U_{ei}$  are the elements of the PMNS matrix that correspond to the electron neutrino [42]. The range of possible Majorana masses as a function of smallest neutrino mass can be calculated by inputting the oscillation parameters and varying the Majorana phases  $\alpha_1$  and  $\alpha_2$ , shown in Figure 2.8.

In equation 2.10, the  $0\nu\beta\beta$  half-life is proportional to the square of the nuclear matrix element (NME). This is not a measurable quantity and determining these NMEs is a difficult problem in nuclear theory. There are many methods of calculating these quantities, the results of which are shown in Figure 2.9: Quasi-particle Random Phase Approximation (QRPA) [90], Energy Density Function method (EDF) [91], Projected Hartree-Fock-Bogoliubov approach (PHFB) [87], Interacting Boson Model-2 (IBM-2) [29], and Large-Scale Shell Model (LSSM) [73]. The variation between these methods is high, and uncertainty in the values of the NMEs is reflected in the uncertainty of the effective Majorana mass. Currently, there is no model-independent way to estimate the uncertainty.

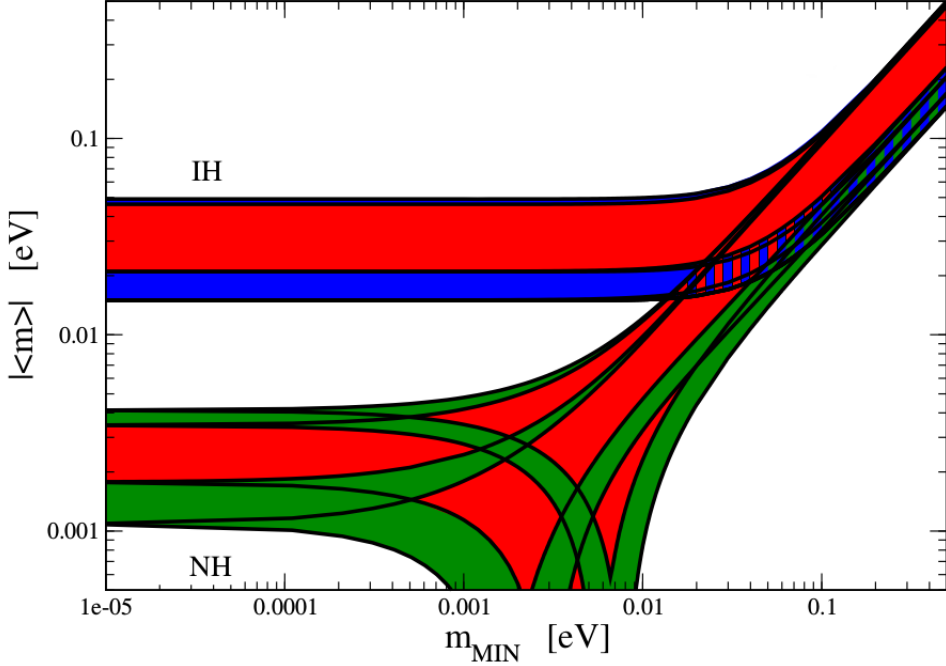


**Figure 2.8:** Effective Majorana mass, shown here as  $|<m>|$ , as a function of the lightest neutrino mass state. The figure is generated using the best fit values and  $2\sigma$  ranges of the current neutrino oscillation parameters. The Majorana phases  $\alpha_1$  and  $\alpha_2$  are varied over the range  $[0, 2\pi]$ . Predictions for the normal and inverted hierarchies are labeled. Red regions correspond to at least one of the Majorana phases having a CP-violating value, whereas the blue and green areas correspond to the Majorana phases having CP-conserving values. From [80].

#### 2.4.2 $0\nu\beta\beta$ Experiments

It is possible to measure the  $0\nu\beta\beta$  decay half-life experimentally by looking for a peak at the Q-value, at the endpoint of the  $2\nu\beta\beta$  energy spectrum. This becomes difficult because the signal is quite small and without excellent energy resolution it will be difficult to distinguish from the  $2\nu\beta\beta$  spectrum. This is illustrated in Figure 2.10, particularly in the inset, for a detector with 5% energy resolution.

There was a claim of an observation of the  ${}^{76}\text{Ge}$   $0\nu\beta\beta$  decay put forward by a portion of the Heidelberg-Moscow Collaboration. Initially, the Heidelberg-Moscow Collaboration reported a limit of  $T_{1/2} < 1.9 \times 10^{25}$  yr [66] in 2001. Shortly after, the collaboration split and Klapdor-Kleingrothaus et al reported an observation of the  $0\nu\beta\beta$  decay with a half-life of  $T_{1/2}^{0\nu\beta\beta} = (0.8 - 18.3) \times 10^{25}$  yr (95% CL) with a best value of  $1.5 \times 10^{25}$  yr [65]. However, the rest of the collaboration did not agree with these findings [27]. In 2004, Klapdor-Kleingrothaus amended the best value of the half-life to  $1.19 \times 10^{25}$  yr [68], and changed it again in 2006 to  $2.23^{+0.44}_{-0.31} \times 10^{25}$  yr. This observation has been in contention since the first claim, and recent results from GERDA do not support the claim for observation of  $0\nu\beta\beta$  decay, finding a lower limit of  $T_{1/2}^{{}^{76}\text{Ge}} > 3.0 \times 10^{25}$  yr (90% CL) when combined with results from previous  ${}^{76}\text{Ge}$  experiments [10].

Experiments that are currently running or running in the near future are listed in Table 2.2.

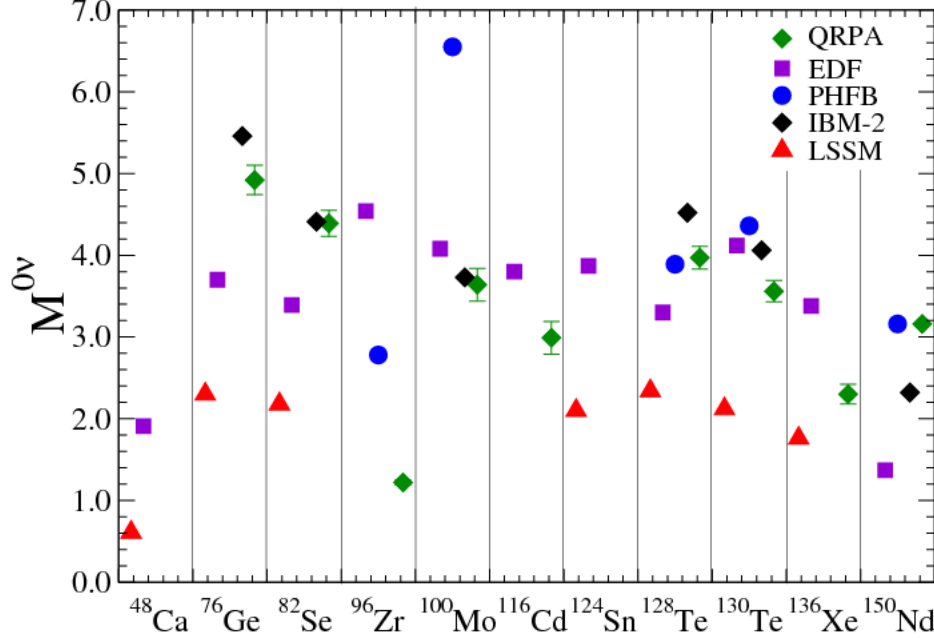


**Figure 2.9:** Nuclear matrix elements for  $0\nu\beta\beta$  decay candidates using the QRPA, EDF, PHFB, IBM-2, and LSSM methods. Variation between these methods leads to uncertainties in the calculation of the effective Majorana mass. From [31].

**Table 2.2:** Current and future  $0\nu\beta\beta$  decay experiments.

Experiment	Isotope	Status
CUORE-0	$^{130}\text{Te}$	running
EXO-200	$^{136}\text{Xe}$	running
GERDA	$^{76}\text{Ge}$	running
KamLAND-Zen	$^{136}\text{Xe}$	running
MAJORANA	$^{76}\text{Ge}$	future
NEXT	$^{136}\text{Xe}$	future
SNO+	$^{130}\text{Te}$	future
SuperNEMO	$^{82}\text{Se}$	future

Regardless of the choice of isotope, there are major design goals common to all  $0\nu\beta\beta$  decay experiments. As previously stated, it is vitally important to achieve excellent energy resolution so that the summed electron kinetic energy peak for  $0\nu\beta\beta$  decay is distinguishable from that of  $2\nu\beta\beta$  decay. However, energy resolution is not the only concern. Large backgrounds can obscure the  $0\nu\beta\beta$  signal peak as well; to increase the signal-to-background ratio, additional signatures are explored, such as event topology or daughter ion tagging. To decrease backgrounds, experiments are generally placed underground and involve a great deal of shielding. Given the long half-lives of the decays in question, large detector masses, high decay isotope enrichment, and high double beta decay detection efficiency [52].

Chapter 3 will describe the EXO-200 detector in detail, including the reduction of backgrounds and the inclusion of radiopure materials. Chapter 4 will discuss data handling, including particle discrimination capabilities to constrain backgrounds.

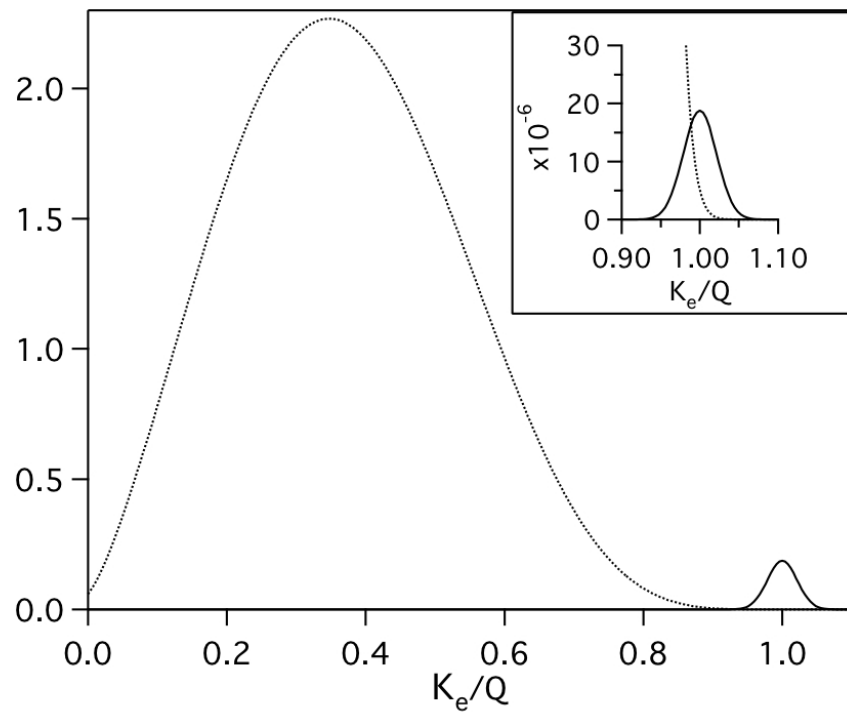


**Figure 2.10:** Spectra of the sum of the electron kinetic energies for  $2\nu\beta\beta$  decay, normalized to 1 (dotted), and  $0\nu\beta\beta$  decay (solid), normalized to  $10^{-2}$  ( $10^{-6}$ , inset), assuming a 5% energy resolution. From [44].

## Chapter 3: EXO-200

The Enriched Xenon Observatory, or EXO-200, is a double beta decay experiment that has an active mass of 110kg of liquid xenon (LXe) isotopically enriched in  $^{136}\text{Xe}$ . EXO-200 is located 2150 feet underground at the Waste Isolation Pilot Plant (WIPP) outside of Carlsbad, New Mexico. WIPP is an active salt mine which houses the only permanent transuranic radioactive waste repository in the United States; nuclear waste that is generated from research and production of nuclear weapons is stored at the site [45]. EXO-200 is located about one mile from the waste storage; locations are shown in Figure 3.1

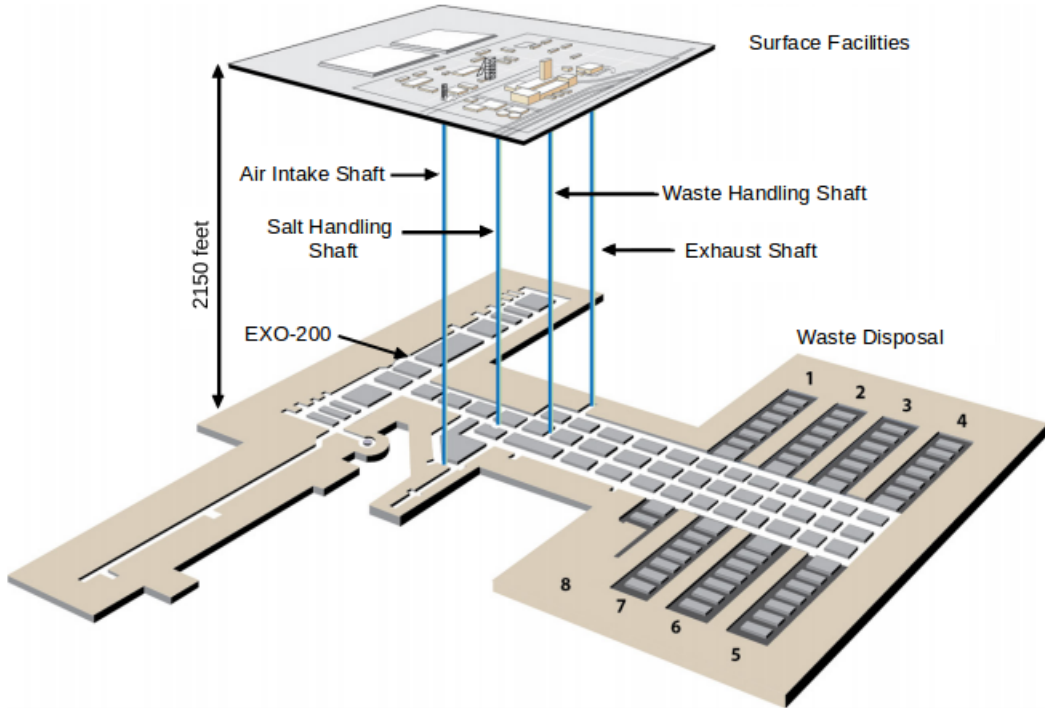


**Figure 3.1:** Map of the Waste Isolation Pilot Plant.

Because of the low rate of  $0\nu\beta\beta$ , it is important to tightly control experimental backgrounds. To ensure low backgrounds, detector materials were carefully chosen [70] to ensure low radioactivity, shielding was provided to reduce external radioactivity, passive components were minimized where possible, and cosmic ray activation was limited during construction and transportation.

### 3.1 Xenon

EXO-200 utilizes a total mass of 200kg of xenon isotopically enriched to 80.6%  $^{136}\text{Xe}$ . 19.1% of the xenon is  $^{134}\text{Xe}$ , with the remaining percentage consisting of natural isotopes that occur in negligible amounts [22].

$^{136}\text{Xe}$  is an attractive isotope for a double beta decay experiment for many reasons.  $^{136}\text{Xe}$  is the decay source as well as the detection medium; this serves to minimize potential backgrounds as well as reducing energy loss from the decay electrons before they are captured. In addition, the double beta decay signature appears as a localized energy deposition and is therefore a single-site event

(described in section 4.2.3), whereas  $\gamma$ -ray backgrounds Compton scatter, and can be identified due to the multi-site signature.

The Q-value for  $^{136}\text{Xe}$  is 2458 keV [76], which has the benefit of being above the energy from most  $\gamma$  rays from naturally occurring radionuclides, with the exception of the 2615 keV  $\gamma$  ray from  $^{208}\text{Tl}$ . A slight drawback to this Q-value is the proximity to the 2448 keV  $\gamma$  line from  $^{214}\text{Bi}$  decay; however, this background can be constrained by measuring the  $^{222}\text{Rn}$  rate in the detector.

Due to the high density of LXe ( $3 \text{ g/cm}^3$  [22]), background  $\gamma$  rays are quickly attenuated near the outer edge of the LXe volume, which provides extra background reduction toward the center of the detector. This self-shielding property will be beneficial when looking toward future experiments; next generation LXe double beta decay experiments will be on the tonne-scale, and will have a large inner volume within the self-shielded region.

Because xenon is a noble gas, it is easy to remove chemically active contaminants. This allows for continuous repurification throughout the lifetime of the experiment. Because there are no long-lived radioisotopes of xenon, contamination due to cosmogenically activated Xe isotopes can be removed by simply holding the xenon underground. With this combination of properties there should be very little contamination left.

While taking data, there is 175 kg of xenon in liquid phase, and 110 kg inside the time projection chamber itself, described in section 3.2. The remaining xenon is gaseous, distributed throughout the gas handling system, described in a simplified cartoon in Figure 3.2.

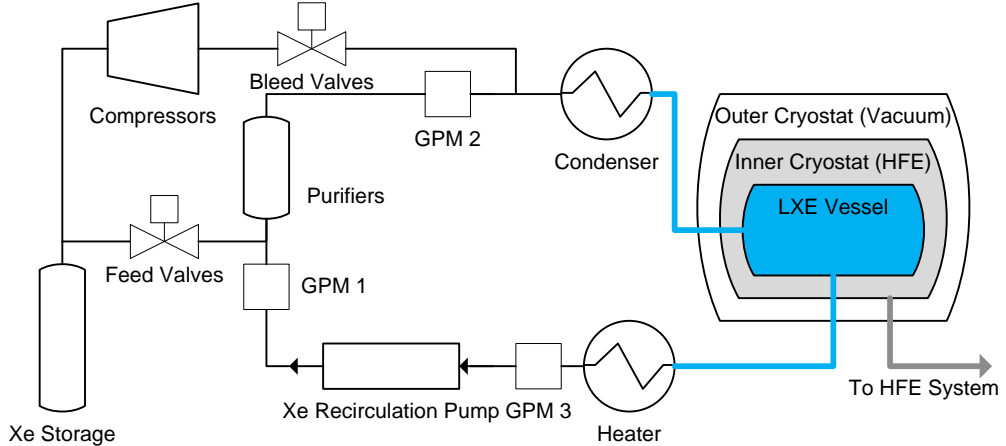
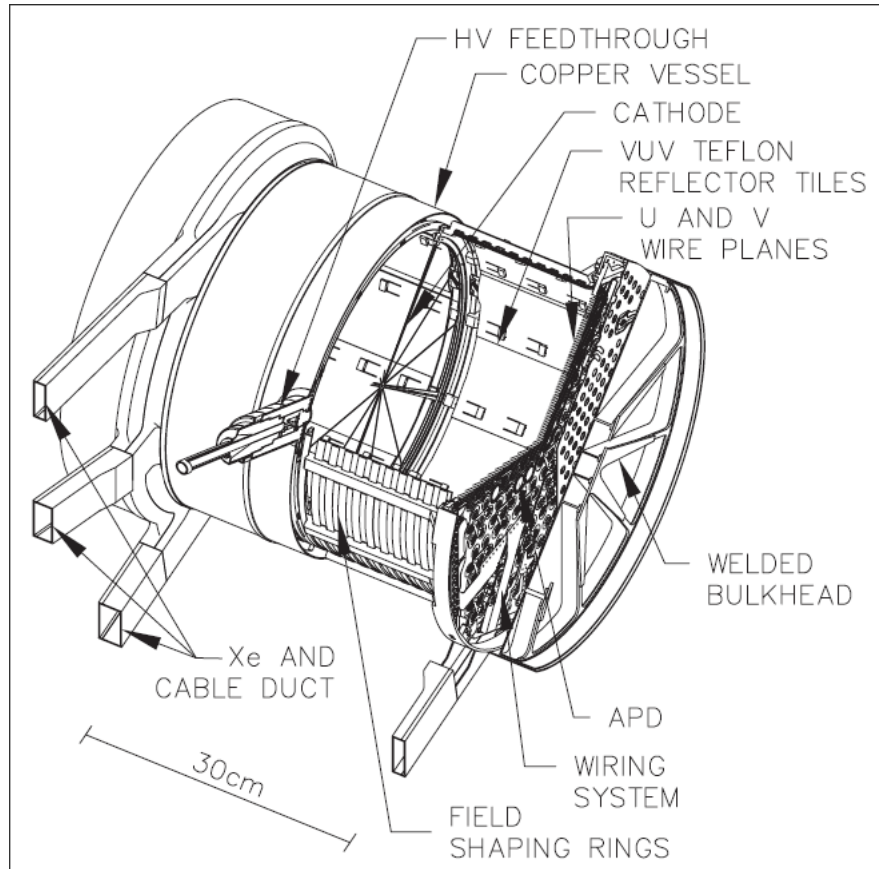


**Figure 3.2:** Simplified schematic of the xenon system. Liquid xenon is heated and returns the gas phase after leaving the TPC, where it is purified before returning to the TPC.

## 3.2 Time Projection Chamber

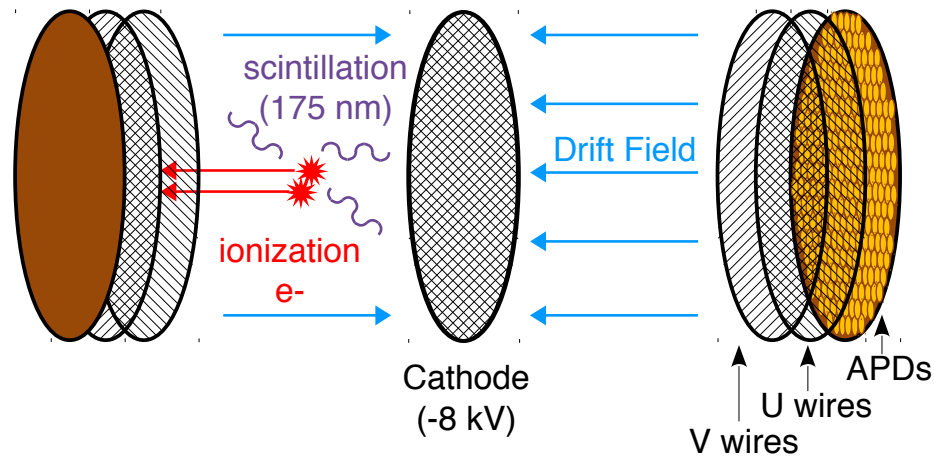
The EXO-200 detector consists of two nearly identical, back-to-back, cylindrical time projection chambers (TPCs), shown in 3.3, which serve to collect ionization and scintillation signals. The TPC volume was set based on the amount of available xenon, which resulted in a 58L volume containing the LXe, cable conduits, and high voltage feedthroughs. The LXe vessel was built using copper and bronze for conductors and acrylic, PTFE and polyimide for dielectrics; all TPC materials were degreased and etched to remove surface contamination [70].

Figure 3.4 shows a simplified, cartoon version of an event occurring in the detector. Decays that occur in the LXe make an energy deposition. As the surrounding xenon is excited, then de-excites, it emits scintillation light with a wavelength of 178 nm, which is captured by 468 Large Area Avalanche Photodiodes (LAAPDs), split between each end of the detector. There is a uniform electric field of 376 V/cm in each TPC, which drifts electrons to the end of the detector, where they pass through the V-wire (induction) plane, and are collected on the U-wire (collection) plane, which is held at virtual ground. A cathode, held at a voltage of -8 kV, separates the two TPCs. The cathode has 90%



**Figure 3.3:** TPC cutaway. [22]

optical transparency. To simplify the cathode feedthrough and make identical signal path-lengths from both ends, the axis of the TPC is horizontal.



**Figure 3.4:** Cartoon schematic of the TPC.

### 3.2.1 Scintillation Channel

Scintillation light is collected with Large Area Avalanche Photodiodes (LAAPDs), described in detail in [77]. LAAPDs were chosen over photomultiplier tubes (PMTs) because they are smaller and therefore have lower levels of radioactivity, are compatible with cryogenic temperatures, and have a higher quantum efficiency at 178 nm. The LAAPDs are used bare, with no ceramic encapsulation; this increases packing density and reduces radioactivity. There is a slight drawback in that they have a lower gain and higher noise than PMTs but this is tolerable at LXe temperatures. Each LAAPD, shown in Figure 3.5, is between 19.6 mm and 21.1 mm in diameter, with an active diameter of 16 mm, a thickness between 1.32 and 1.35 mm, and a mass of 0.5 g.

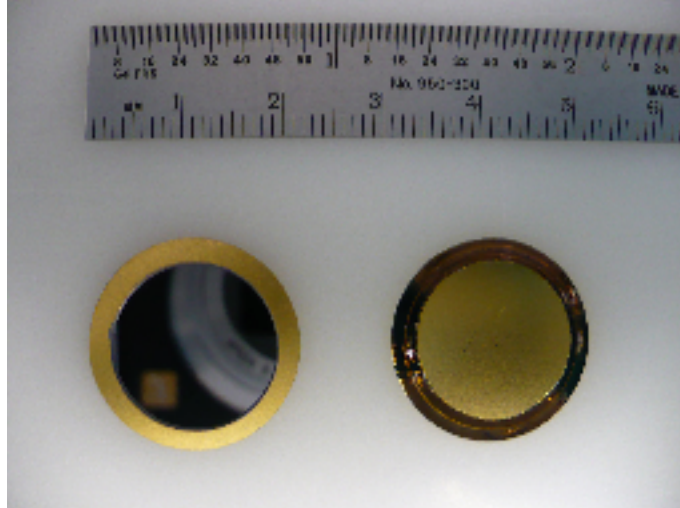


**Figure 3.5:** Large Area Avalanche Photodiode. Ruler shows size in cm and inches. On the right: gold-plated cathode; on the left, active surface surrounded by gold-plated ring-wafer anode.

Tests were done with custom equipment on 851 LAAPDs to understand the noise, gain, and quantum efficiency before installation in EXO-200. The LAAPDs were tested at the operating temperature of EXO-200, 170K. Of the LAAPDs that met operating specifications, those with the lowest noise were chosen for installation. While the energy resolution was not a criterion for installation within EXO-200, only two devices that were selected had a resolution (at 5.90 keV) above 15%, and none were above 16.5%. To test the stability of the LAAPDs over time, a few of the LAAPDs were kept in the same location in the grouping over many testing cycles. Over 600 days, no systematic gain fluctuations were observed and the gain of each device was constant to within 3% [77].

The resulting 468 LAAPDs are mounted on two platters at either end of detector, constructed from the same copper as the LXe vessel; the front of the platter is aluminum-plated to reflect photons that miss the LAAPDs, and the back of the platter is gold-plated for improved electrical contact with the LAAPD anodes. Each platter contains 234 LAAPDs, which are mainly ganged for readout in groups of 7 although there are some in gangs of 5 and 6; this ensures gain uniformity by grouping LAAPDs with a similar gain and tuning the bias voltage for that gang. The photosensitive packing fraction of this arrangement is 48%.

Due to the electric field it is impractical to install LAAPDs throughout the entire detector, particularly around the field cage. In these regions there are reflective PTFE tiles, which increases the light collection efficiency by 50-150%.

### 3.2.2 Ionization Channel

The ionization channel includes the TPC cathode and field cage, which defines a region of uniform electric field, and the U-wire and V-wire planes, which are the charge collection and induction wire planes, respectively.

#### 3.2.2.1 Wire Planes

The wire readout planes are the U-wire (charge collection) plane and V-wire (charge induction) planes, a portion of which are shown in Figure 3.6. The U-wire plane is located 6 mm in z above the LAAPD plane, and the V-wire plane is 6 mm above the U-wire plane, as illustrated in Figure 3.7. The U- and V-wire planes are rotated 60° from each other which allows for 2-dimensional reconstruction of the ionization cloud location. There is 3 mm spacing between each adjacent wire. The spacing between wires as well as between planes were chosen to ensure a maximal fiducial volume while still allowing electrical transparency without requiring a large high voltage on the V-wire plane. Each wire plane has 95.8% optical transparency so that the scintillation signal is not blocked from the LAAPD plane.

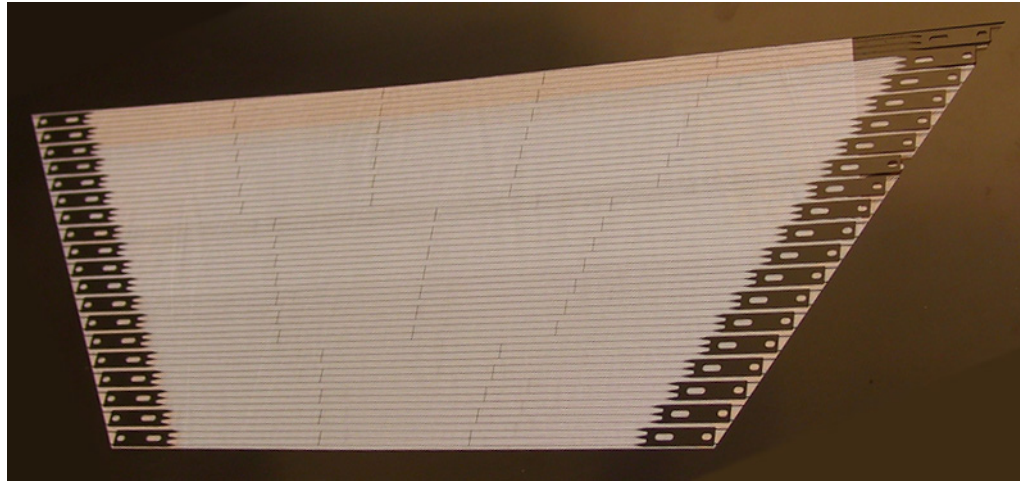


**Figure 3.6:** Panel of wires from the wire readout planes. This panel contains half of the wires for one plane [22].

Readout channels are organized by wire triplets, resulting in 38 readout channels for each plane. Grouping these wires into triplets allowed for the usage of fewer electronics channels, which allowed for fewer materials near the fiducial volume. Using extra channels would not necessarily have improved the ability to determine between single site and multi-site events [22].

Wire triplets were photoetched from 0.13 mm thick phosphor bronze [1]. A spring is created at the end of each triplet by folding it, which allows for wire stability at the electric field at which EXO-200 operates. Each wire triplet is connected by a bridge every 10 cm. Screws anchor each end of the triplet to six 6-mm thick acrylic beams which are mounted on a copper support ring to form a hexagon. The U- and V-wire planes are stretched between two pairs of these acrylic beams, with the wire planes mounted on opposite sides of the beams. The length of the wire triplets ranges from 22.8 cm to 41.5 cm along the acrylic.

#### 3.2.2.2 Field Cage

The drift region is defined by the V-wire planes, the cathode, and the PTFE reflecting tiles installed between the field shaping rings. This results in a cylindrical drift region of 18.3 cm in radius and 38.4 cm in length. The electric field is graded in ten steps by copper field shaping rings; each ring is 0.97 cm long, with an outer diameter of 37.4 cm. The pitch between rings is 1.69 cm. Simulations

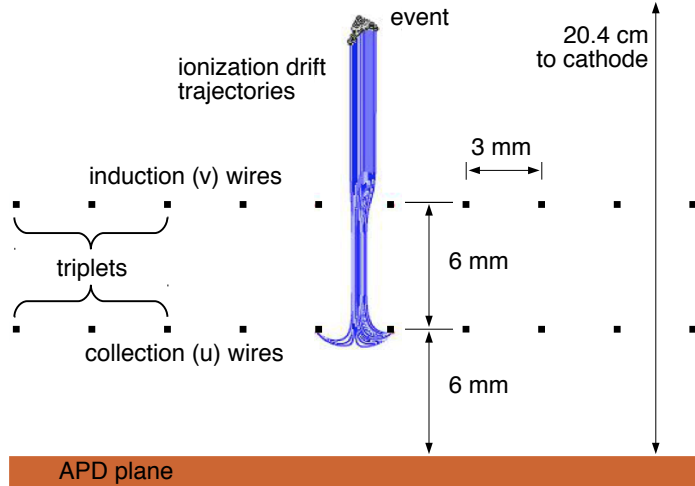


**Figure 3.7:** Geometry of the readout planes with a simulated  $0\nu\beta\beta$  event. In actuality the U- and V-wire planes are rotated 60° with respect to each other.

of this geometry [2] predict full electron collection from a cylinder with radius 0.8 cm smaller than that made by the field shaping rings.

The cathode is mounted on the last ring of one of the field cages. Like the U- and V-wire planes, the cathode is made from photoetching sheets of phosphor bronze; it also has springs at the edges to maintain tension. The screws used to install the U- and V-wire triplets are also used to secure the cathode onto the copper ring. A special high voltage feedthrough to the cathode was developed for EXO-200 to fulfill background requirements.

### 3.2.3 Vessel

The previously described components are all housed in a thin-walled, quasi-cylindrical copper vessel which flares out at each end to accommodate the wire planes, LAAPD planes, and the associated wiring. In the center, the vessel closely contains the field cage, with a diameter of 39.62 cm. The vessel is built using low-background copper and is only 1.37 mm thick in most places, resulting in a total mass of under 30 kg. Finite element analysis was used to show that the vessel should be able to handle pressures of up to 33 kPa. The vessel, shown in Figure 3.8, was welded to the inside of the cryostat before TPC components were installed.

### 3.2.4 Guide Tube

Calibrations for EXO-200 are done by positioning radioactive  $\gamma$  ray sources such as  $^{228}\text{Th}$  at various positions around the vessel. To maximize the full absorption efficiencies in the active detector volume the sources must be placed close to the detector. This is done by inserting the source into a copper guide tube that is attached to the cryostat, inside the HFE7000 volume, shown in Figure 3.9. The sources are then deployed to a known location along the length of the tube where they remain for the source calibration runs.

## 3.3 Passive Shielding

There are several layers of shielding that protect the LXe from external radioactivity, with layers getting progressively cleaner as they get closer to the LXe. The innermost layer of shielding is a  $\geq 50$  cm layer of HFE7000 [3], located outside of the LXe vessel but inside the inner vessel of the cryostat; this layer of refrigerant doubles as a thermal insulator for the LXe. Nested cryostat vessels



**Figure 3.8:** TPC vessel before welding to the inside of the cryostat [22].

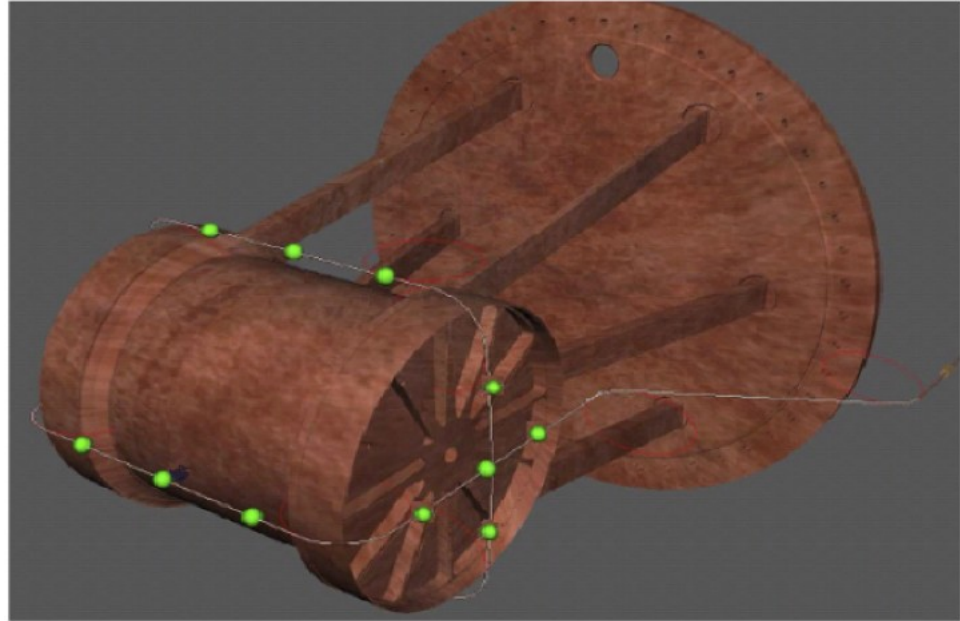


**Figure 3.9:** Guide tube attached the TPC vessel, with source locations highlighted [22].

give another 5.4 cm of copper shielding. The outermost layer of passive shielding comes from 25 cm of low radioactivity lead blocks.

Feedthroughs in the cryostat allow for plumbing and electrical connections to pass through. Another lead wall, 20 cm thick, is placed outside of this hardware. The front end electronics are made from regular, non-low-background materials and are placed between the two lead walls, out of line of sight of the TPC.

### 3.3.1 Muon Veto

Cosmic ray muon flux at WIPP was measured to be  $4.07 \pm 0.14(\text{sys}) \pm 0.03(\text{stat}) \times 10^{-7} \text{cm}^{-2} \text{sr}^{-1}$  [13]. Muons that travel through the TPC are rejected based on their tracks and large energy depositions. However, when cosmic ray muons and spallation muons move through detector components and shielding, they produce  $\gamma$  rays. To reject this background, as well as muon bremsstrahlung, an external muon veto is required.

The muon veto consists of 31 plastic scintillator panels on the outside of four of the six walls of the clean room module that contains the TPC. The scintillator panels were repurposed from the KARMEN experiment [41]. All panels were refurbished, tested, and calibrated before installation. Each panel has 180° light guides at each end, and are wrapped in aluminum foil to increase the light collection of each panel. Each panel end is read out by four 2" PMTs which make up 58 channels. There is a dedicated readout module which takes the analog signals from the PMT channels, applies a threshold, and reports any signal above threshold in the TPC data stream. The muon veto efficiency was measured to be  $96.0 \pm 0.5\%$  [22].

## 3.4 Assembly and Installation

Throughout assembly, special care was taken to protect materials from surface contamination. The detector was assembled in a class 1000 cleanroom with a  $\sim 7$  m.w.e. concrete overburden. Machining of low-background components was done with new carbide tools and while using gloves.

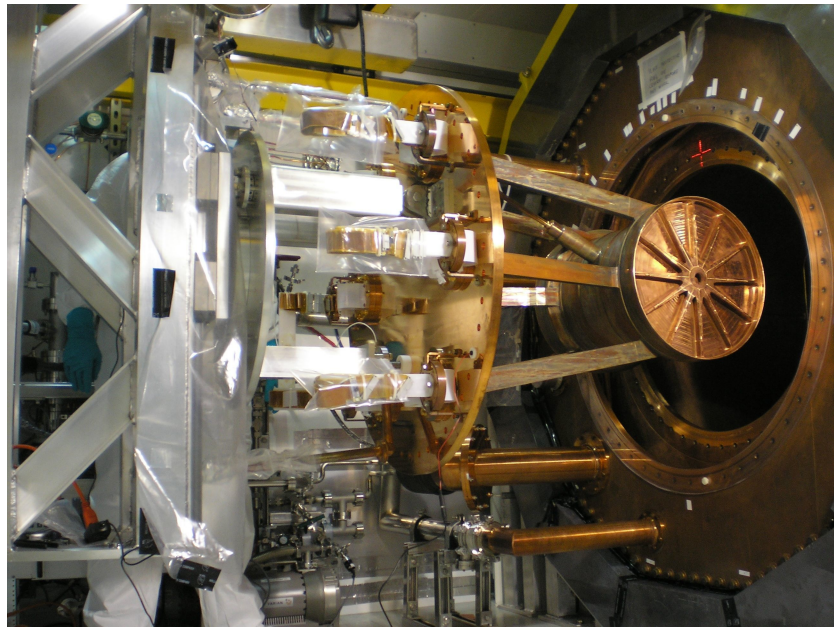


**Figure 3.10:** The TPC being inserted into the cryostat [22].

Before installation, all detector components were cleaned with the following: acetone rinse to remove grease, with the exception of those materials that were incompatible with acetone; ethanol rinse; 0.5 - M 1.5 M HNO<sub>3</sub> rinse, with the copper and copper-based alloys receiving the more dilute treatment; and 18 MΩ-cm deionized water rinse. After the final cleaning, all components were stored under nitrogen boil-off atmosphere.

It is important to minimize cosmic-ray activation of detector components prior to installation; because EXO-200 has many copper components it is especially important to do this as <sup>60</sup>Co is a potential background. The copper cryostat and TPC components were made from batches of high purity electrolytic copper [4]. Steps were taken to ensure that the time the TPC components and cryostat spent above ground was minimized, and the TPC and cryostat were underground for 18

months and 3 years, respectively, before low background data taking began. The TPC was installed in the cryostat, shown in Figure 3.10, in January 2010.

## Chapter 4: Data Handling

Initial data files contain digitized, unprocessed waveforms of the signals on the U-wires, V-wires, and APD channels. Before analysis can be done, this data must be processed so that these waveforms are transformed into physical quantities which describe the events. The processing chain can be split into three main parts: rootification, reconstruction, and processing. This section details the data acquisition system and the processing chain, as well as data quality checks.

### 4.1 Data Acquisition System

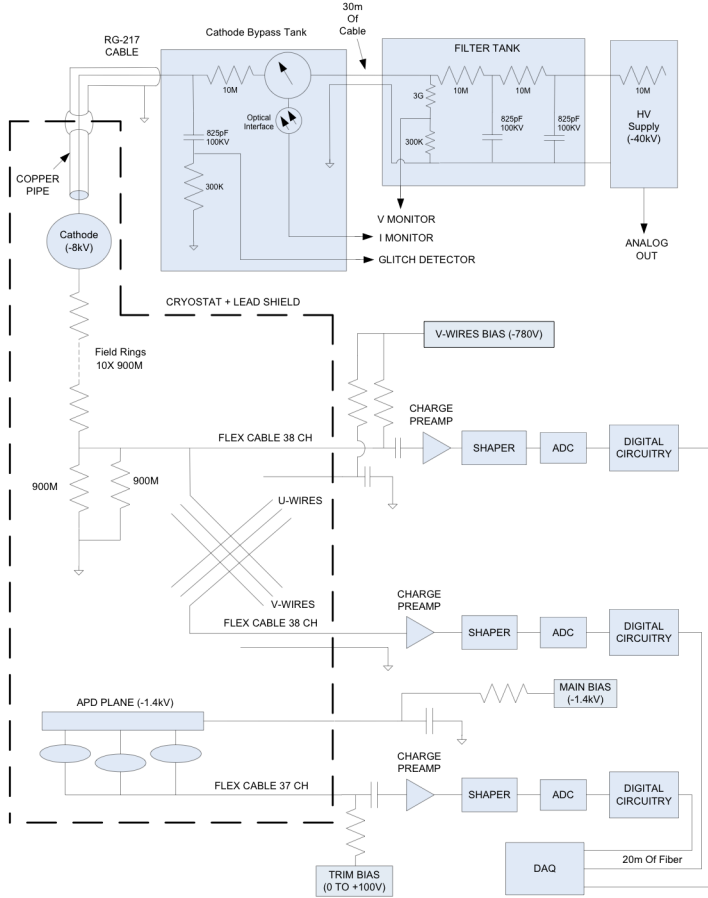


**Figure 4.1:** Detector readout electronics system.

The EXO-200 data acquisition system (DAQ) [12] is composed of 226 hardware channels, a muon veto, and a high voltage (HV) glitch detector. The hardware channels consist of 76 U-wire channels, 76 V-wire channels, and 74 avalanche photodiode (APD) channels. Front end electronics, composed

of low-noise charge amplifiers with a dual, two-stage shaper, followed by a 12 bit 1MS/s analog-to-digital converter (ADC), couple the hardware channels to the DAQ. Digitized data is fed to the Trigger Electronics Module (TEM), which synchronizes the data from all hardware channels and forms detector triggers; the electronics scheme is illustrated in Figure 4.1.

If there is a valid trigger, data are stored to disk. Muon veto and glitch detector events are stored separately and are synchronized with TPC data later, based on their time stamps. When a TPC trigger occurs, the TEM transfers digitized data from all hardware channels starting from  $1024 \mu\text{s}$  before the trigger through  $1024 \mu\text{s}$  after the trigger. Four types of triggers are used during low background physics runs, with the thresholds for each in parentheses:

1. individual U-wire triggers for LXe  $\gamma$  and  $\beta$  events ( $\sim 100\text{keV}$ ). This is the main physics trigger, and triggers on the U-wires rather than the APDs because the scintillation signal from  $\gamma$  and  $\beta$  events is quite low.
2. APD individual trigger for activity inside the respective APDs ( $\sim 3\text{-}4 \text{ keV}$ ); this trigger is to monitor APD noise over time.
3. APD sum trigger for LXe alpha events ( $\sim 25\text{k photons}$ ). The APD sum trigger detects  $\alpha$  events only as  $\beta$  or  $\gamma$  events do have a large enough scintillation signal for this trigger.
4. 0.1 Hz forced trigger for monitoring detector performance; this trigger is also used during calibration runs for strong radioactive sources which would normally overload the DAQ with triggers.

Data are written to local storage, then transferred to an offline data storage facility. The DAQ is controlled from a graphical web based application which allows data quality plots and information from the DAQ database to be viewed both at WIPP and remotely [22].

## 4.2 Data Preparation

The data is prepared for physics analysis in several steps: rootification, reconstruction, and processing, illustrated in Figure 4.2.

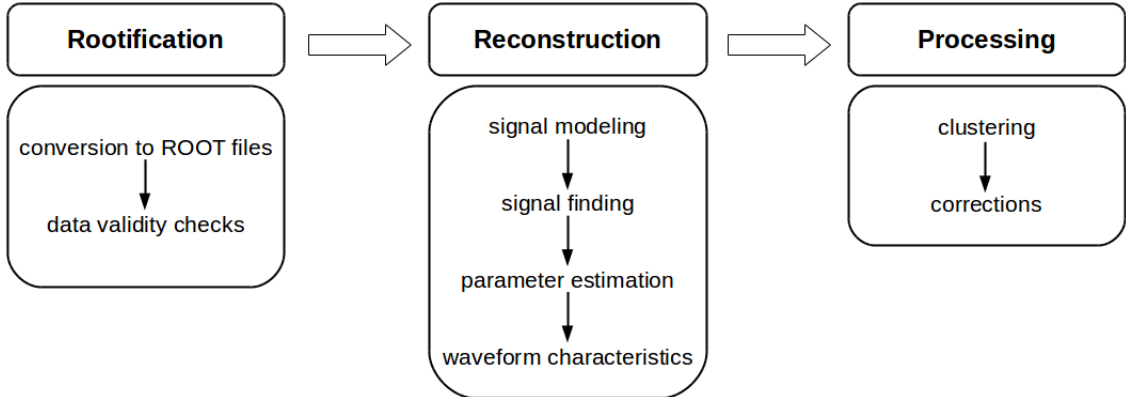


**Figure 4.2:** Flowchart of the EXO-200 processing chain.

### 4.2.1 Rootification

“Rootification” is the conversion of binary data files to ROOT [33] files. For a run to be used in the physics analyses, it must meet a few initial requirements; these low-level checks of data validity

are also performed here. The run length must be  $>1800$  seconds; this ensures that there are enough statistics to calculate the higher-level checks. The average solicited trigger rate must be within 0.5% of its nominal value, 0.1 Hz, and the calculated livetime must be no more than 30 seconds different from the run duration. These requirements ensure there is no reduction in livetime due to noise or a malfunctioning DAQ. A subset of events are sent to an online monitoring system in real time; this system can be accessed on-site at WIPP and remotely.

### 4.2.2 Reconstruction

Reconstruction is broken down into three major sections: signal finding, signal parameter estimation, and determination of waveform characteristics. Noise and muon tagging also occur during this process.

First, signal models are developed for all channels. Unshaped signals for the U-wires and V-wires are created using EXO-200 GEANT4-based [16] Monte Carlo simulation software (an in-depth discussion of the signal simulation is given in [12]); a step function is used as unshaped APD signals. These are then shaped with transfer functions determined by the front end electronics.

Signal searches occur on waveform traces. There are two methods used to search for signals: matched filter method and waveform unshaping. The matched filter method [78] is applied, used here because it is easy to implement and has been shown to have a stable performance over time. However, it is designed to find single pulses and does not perform well when there are multiple signals that arrive close together in time. To handle this, after the waveform is identified by the matched filter, an algorithm is applied to “unshape” the signal, which results in the original charge deposited. Once the original charge is found, it is reshaped with a  $2 \mu\text{s}$  triangular, or moving average, filter (such as in [64]). The reshaped waveform is then analyzed with a peak-search algorithm to search for multiple signals.

Amplitudes of the channel signals are calculated by fitting the waveforms to their signal models. A  $\chi^2$  function is built using the signal model, the data, and the output of the previous signal finding stage, which is then minimized using MIGRAD [63]. This gives signal amplitudes, times, and errors, in addition to the overall value of the minimized  $\chi^2$  function. The results of the fits to the two APD sum signals are then used to fit individual APD channels separately and calculate the amplitudes of each channel.

It is possible for charge to drift close to a U-wire channel to induce a signal without actually being collected on that channel, while being collected on a neighboring channel. Identification of the induction signal is important so that it is not mistakenly reconstructed as a low-energy charge cluster, which could cause events that should be categorized as single-site to be mistakenly classified as multi-site.

To differentiate between U-wire induction signals and low energy U-wire signals, several characteristics are calculated from the U-wire waveforms, including pulse timing, the pulse integral, the fit  $\chi^2$ , and the nearest neighbor amplitude. A full discriminator is built from these values, the U-wire induction signal rejection efficiency of which is calculated to be 77%. The acceptance efficiency for collection signals with at least 250 keV of deposited energy is  $>99.9\%$ .

### 4.2.3 Processing

After individual channel signals have been reconstructed, they are associated in a process called “clustering.” The processing step also includes recursive database corrections, discussed in section 4.3, to account for varying detector performance.

Once signal parameters have been calculated, corrections accounting for variations in channel gain (as in section 4.3) are applied; following these corrections, signals are grouped based on their channels, e.g., U-wires with other U-wires. The z-position of the event is determined by associating the U-wire bundles with APD bundles and determining the difference in time between them. Finally, the U- and V-wire bundles are grouped together, forming a fully 3-D reconstructed cluster.

U-wire signals are bundled together based on signal arrival time; adjacent channels that see signals within  $3.5 \mu\text{s}$  of each other are bundled together. The time associated with each bundle is

found by calculating the amplitude-weighted average of the signals.

V-wire signals are also bundled according to time; however, the timing works differently than the U-wire signals. The V-wire channels further from the drifting charge are shielded by the nearby wires as the charge nears the V-wire plane. Because of this, the V-wire signals that have the lowest charge are reconstructed earlier in time than the V-wire signal with the largest amplitude, which is taken as the “central” signal. Therefore the relationship used to determine the V-wire signal bundling is

$$|t_i - t_0 - (2.97\mu\text{s}/\text{chan})\Delta V| \leq 4.5\mu\text{s} \quad (4.1)$$

where  $t_0$  is the time of the signal on the channel with the “central” signal,  $t_i$  is the time of the signal on the channel being investigated, and  $\Delta V$  is defined as the absolute channel number -difference of the two signals, which takes into account the linear relationship between the difference in time and the number of channels between the signal and the central signal. The time for the V-wire bundle is given only by the time of the central signal as using a weighted time average here reduces the ability to correlate U- and V-wire bundles later.

APD signals are bundled if they arrive within  $6\ \mu\text{s}$  of one another, with no position requirement. The overall time of the scintillation bundle is a weighted average of the time and energy of the individual signals.

Once the bundles are calculated for each type of channel, a z-position for the event must be determined. To do this, all scintillation bundles that occur between  $3\ \mu\text{s}$  after and  $3\ \mu\text{s}$  plus the maximum drift time before the U-wire bundle are examined; the scintillation bundle with the smallest absolute time difference from the U-wire bundle is chosen. If there is no scintillation bundle in that time frame, the z-position is not set, the U- and V-wires are not associated in a charge cluster, and the event position is not reconstructed further.

For events that have a reconstructed z-position, U- and V-wire bundles are associated into charge clusters using probability density functions (PDFs), described in detail in [12]. The PDFs are used to check that the time difference between the bundles is valid, that there is consistency between the signal amplitudes in the U- and V-wire bundles, and that the resulting coordinate is physically possible. These PDFs are dependent on the z-position of the U-wire bundle, which is why the event position cannot be reconstructed further if there is no associated scintillation bundle.

A cost function is created to measure how well U- and V-wire bundles match,

$$\text{cost} = \sum_{i=1,2,3} -\log P_i, \quad (4.2)$$

where the sum is over the three PDFs. A lower cost indicates a higher likelihood for a given configuration. The matching algorithm tests all combinations of U- and V-wire bundles; the best matching configuration is where the sum of the cost divided by the number of connections is minimal, where the number of connections is either the number of U-wire bundles or V-wire bundles, whichever is smaller. Once the configuration is determined, a charge cluster is created for these connections and it is associated with the scintillation bundle that was connected to the U-wire bundle. The x-y position of the event is reconstructed using position information of the charge cluster.

Clustering sometimes fails to associate bundle types together and therefore does not create a 3D position for an event. This can occur due to clustering errors, or due to signals falling below detection thresholds; this reduces the efficiency of reconstructing the position of events that have a large scintillation signal but a small charge signal. Clustering may also skip an event if there are too many signals found.

Events that have charge clusters contained in a volume with a characteristic dimension of 2-3 mm are labeled as single-site (SS) events. This volume is expected for most  $2\nu\beta\beta$  and  $0\nu\beta\beta$  events in LXe; alpha and beta events are also expected to be single-site events. Otherwise, the event is labeled as multi-site (MS) events. Due to Compton scattering, which is predominant in the energy range of interest (700 keV - 3500 keV), the majority of gamma events are categorized as MS, producing two or more charge deposits that are separated by several centimeters.

### 4.3 Detector Performance

Several detector characteristics are monitored via the online monitoring system, and corrections based on these values are implemented during the processing stage. These corrections include channel-based, position-based, and time-based corrections.

#### 4.3.1 Channel Gains

U-wire channel gains were measured previous to Run 2 using a pulser coupled to the front-end electronics; the gain was calculated by a linear fit to the measured amplitude versus the injected charge. While running, U- and V-wire gains are monitored daily using a charge injection system that is integrated into the front-end electronics. The gain corrections are implemented on each channel during the processing stage of the data preparation.

APD gains are monitored weekly using an external laser pulser. The APD signals are not explicitly gain corrected on a channel-by-channel basis, as the gain variations are absorbed into a post-processing algorithm that removes coherent noise from the APDs [37].

#### 4.3.2 Energy Resolution

The energy resolution of the detector is not straightforwardly the scintillation or ionization energy resolution, but instead a “rotated” energy resolution that combines these measurements,

$$E_R = E_S \cdot \sin(\theta^R) + E_I \cdot \cos(\theta^R), \quad (4.3)$$

where  $E_R$  is the rotated energy and  $\theta^R$  is the rotation angle. The combination of the two measurements greatly improves the energy resolution over using either signal individually, illustrated with  $^{228}\text{Th}$  source calibration data in Figure 4.3.

The energy resolution of the ionization channel is fairly constant in time with a value of  $\sigma/E = 3.5\%$  and  $4\%$  at 2615 keV for SS and MS events, respectively. Scintillation-only energy resolution varies with time due to coherent noise across the APDs; this is expected to improve with the next front-end electronics upgrade. Because of this scintillation-only variation, the optimal rotation angle also varies. The rotation angle is calculated weekly from  $^{228}\text{Th}$  source calibration data and the rotated energy is calculated for each period that the rotation angle is calculated.

The amount of scintillation collected by the APDs is dependent on the event location; this is caused by differences in the solid angle covered by the APDs and by their gain differences. A “light map” is generated to correct for these differences, created from  $^{228}\text{Th}$  calibration runs with the source placed at each anode, and three positions around the cathode plane. The light map correction improves the scintillation-only energy resolution at 2615 keV from 7.9% to 6.0% for SS events and from 8.1% to 6.3% for MS events. The light map correction is also implemented in the processing stage.

#### 4.3.3 Electron Lifetime

A time-based correction to account for the purity of the LXe is also applied here. Electronegative impurities in the LXe can cause decay electrons to be captured before drifting to the wire grids. This attenuation is described by

$$N_e(t) = N_0 \exp(-t/\tau_e) \quad (4.4)$$

where  $N_0$  is the original number of electrons,  $\tau_e$  is the electron lifetime, and  $t$  is the drift time. The electron lifetime is measured every few days using  $^{228}\text{Th}$  source calibration runs and is calculated from a fit to equation 4.4. This value varies due to changes in the xenon recirculation rate, interruptions due to pump maintenance or power failure, and adding xenon to the detector system. To account for this, a piecewise polynomial is fit to the measured  $\tau_e$  history. A correction factor of  $\exp(t/\tau_e)$  is applied to all ionization signals.

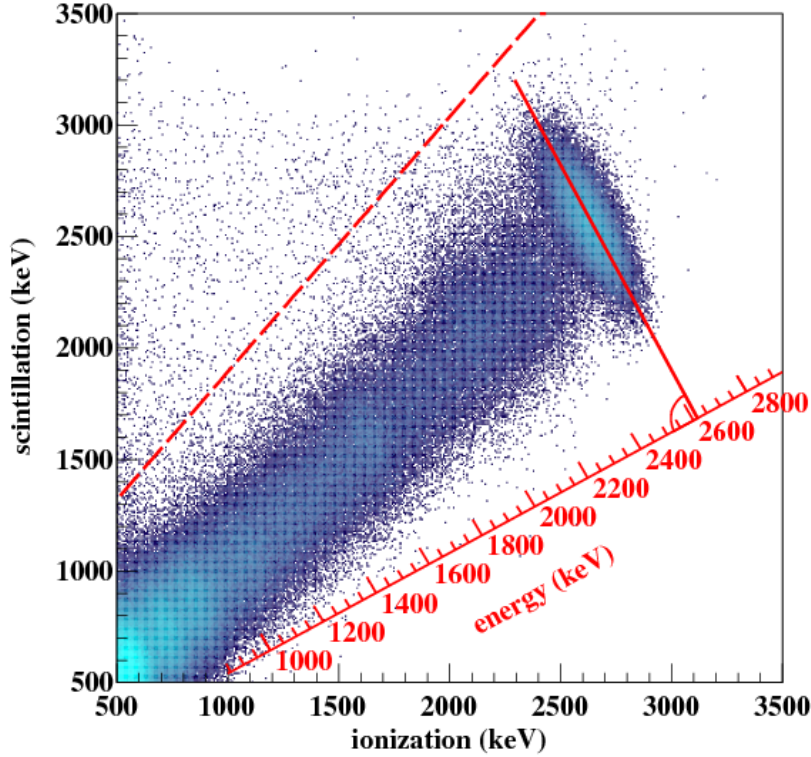


**Figure 4.3:** Anti-correlation of scintillation and ionization signals. The energy resolution is improved by using the linear combination of both signals [8].

Uncertainty in this correction, or periods where this correction is changing quickly, can decrease the energy resolution. To avoid this, periods of time in which the electron lifetime is less than 1 ms are removed. To ensure stability of this measurement, four or more consecutive measurements of similar electron lifetimes over several days with constant xenon recirculation are required. Throughout these measurements, the electron lifetime must not increase at a rate of >50% or decrease at a rate of >25% of the previous measurement per day.

## Chapter 5: Machine Learning

Most generally, machine learning is the ability of a learning program to perform accurately after experiencing a data set on which to train. This training set often comes from a representative distribution of the overall dataset, and the learner will build a model based on what it has learned from the training set and apply it to new cases. Machine learning algorithms are typically sorted into two categories, based on the amount of feedback available to the learner: supervised and unsupervised. Both types are provided a set of features, which are the learning inputs. Supervised algorithms, however, are given a set of targets, or outputs; unsupervised algorithms are not given these truth values while training.

Unsupervised learning algorithms handle data that do not come with a corresponding set of target values. These algorithms focus on clustering, density estimation, and visualization. Clustering algorithms are given a data set, and the learner finds patterns within that data set and groups similar types of data. Density estimation algorithms determine the distribution of data within the input space. Visualization algorithms project high-dimensional data to a 2- or 3-dimensional space.

Supervised learning algorithms can be further split into two large categories: classification and regression. Classification algorithms sort data into discrete categories based on their features; for example, this type of algorithm is useful for handwriting recognition of the alphabet. Regression algorithms are used when the target is a continuous output; for example, the prediction of the value of a house based on age, size, number of rooms, etc.

The rest of this work utilizes a type of supervised algorithm known as decision trees, which are used for both classification and regression problems. This work also focuses on regression algorithms as this will be used to reconstruct the position of events in the EXO-200 detector. The rest of this chapter focuses on the subset of regression algorithms that were tested in preparation for use in subsequent chapters.

### 5.1 Bias-Variance Tradeoff

The two main sources of error for machine learning algorithms are bias and variance. -Minimizing these errors is essential so that the algorithm is capable of generalizing beyond the training set. However, it is generally impossible to rid the algorithm of both bias and variance.

Bias comes from error in the assumptions in the algorithm, whereas variance comes from being too sensitive to small fluctuations in the data. High bias will cause an algorithm to miss connections between features and targets; this is called underfitting. For example, this could come from using a linear fitter to approximate a non-linear function; the variance may be small as it would not be particularly sensitive to large fluctuations in the training set, but it would certainly underfit a non-linear function. High variance will cause overfitting, if the algorithm is too sensitive to slight changes in the training set. The learner will be able to predict the targets of the training set perfectly, while being unable to properly predict the targets of other datasets.

There are steps that can be taken to decrease bias and variance, though decreasing one usually tends to increase the other. Adding features to the training set tends to decrease bias, at the expense of adding variance. Increasing the samples in the training set tends to decrease variance. Most learning algorithms have tunable parameters that control the acceptable level of bias and variance. In particular, many decision tree algorithms allow for the control of the depth of the tree, or the number of decisions made before final classification. If the tree is too deep, it will be too specific to the training set and will not generalize well to other datasets.

## 5.2 Linear Regression

Linear regression algorithms are an attractive set of learners due to the lack of complexity of the algorithm, low cost of usage, and ease of implementation. These methods in which the target value is estimated as the linear combination of the input variables; that is, if  $\hat{y}$  is the predicted value, then

$$\hat{y}(w, x) = w_0 + w_1 x_1 + \dots + w_p x_p \quad (5.1)$$

I started with the ordinary least squares (OLS) method as it was the most straightforward method. The OLS method works by fitting a linear model with coefficients  $w = (w_1, \dots, w_p)$  to minimize the residual sum of squares between the observed responses in the dataset and the responses predicted by the linear approximation. Mathematically it solves

$$\min_w \|Xw - y\|_2^2 \quad (5.2)$$

where  $X$  and  $y$  are the features and targets, respectively, and  $w$  are the coefficients determined by the algorithm. The coefficients, however, rely on the independence of the model terms; when terms are correlated, the least-squares estimate becomes sensitive to random errors in the training set, producing a high variance. Performance of the OLS algorithm is shown in Figure 5.1.

## 5.3 Decision Trees

Decision trees ([32], [86], [53]) can be visualized as a flowchart in which each internal node is a test of an attribute of the data, each branch is the outcome of that test, and each leaf is the decision after computing all attributes. Decision trees are most commonly used for classification, but can be expanded to regression problems as well.

Decision trees are beneficial because they are simple to understand, and the trees can be visualized. The data do not need to be prepared in any particular way in advance; it can simply be fed into the algorithm. Decision trees can handle numerical data, as well as multi-output problems. The cost of constructing the tree varies slightly depending on the algorithm used; the DecisionTreeRegressor (DTR) from scikit-learn [82] costs  $O(n_{features} n_{samples} \log(n_{samples}))$  to construct. The cost of predicting the data is  $\log(n_{samples})$ .

It is most attractive, however, because it is not a black box. For an observable condition in the data, the explanation for the result can be explained with boolean logic. It is also particularly attractive because it is easy to validate the model using statistical tests, so that the reliability of the model can be calculated.

Given training vectors  $x_i \in R^n$ ,  $i = 1, \dots$ , and a label vector  $y \in R^l$ , a decision tree partitions the space recursively so that samples with the same labels are grouped together. Let the data at node  $m$  be represented by  $Q$ . For each candidate split  $\theta = (j, t_m)$  consisting of a feature  $j$  and threshold  $t_m$ , partition the data into  $Q_{left}(\theta)$  and  $Q_{right}(\theta)$  subsets:

$$\begin{aligned} Q_{left}(\theta) &= (x, y) | x_j \leq t_m \\ Q_{right}(\theta) &= Q \setminus Q_{left} \end{aligned}$$

The impurity at  $m$  is computed using an impurity function  $H()$ , the choice of which depends on whether the algorithm is being used for classification or regression.

$$G(Q, \theta) = \frac{n_{left}}{N_m} H(Q_{left}(\theta)) + \frac{n_{right}}{N_m} H(Q_{right}(\theta)) \quad (5.3)$$

Selecting the parameters that minimize the impurity

$$\theta^* \operatorname{argmin}_{\theta} G(Q, \theta) \quad (5.4)$$

And recurse for subsets  $Q_{left}(\theta^*)$  and  $Q_{right}(\theta^*)$  until the maximum allowable depth is reached,  $N_m < \min_{samples}$  or  $N_m = 1$ .

DTR can be used for multi-output problems where there are several outputs to predict, so instead of outputting an array of values, the targets are a 2d array of size of  $[n_{samples}, n_{outputs}]$ . When there is no correlation between the targets, the simple way to handle multi-output problems is to build  $N$  independent models, where  $N$  is the number of outputs, then independently predict each output. However, it is likely that targets related to the same inputs are themselves correlated. Therefore it can be a better approach to build one model which is capable of predicting the outputs simultaneously. This provides a reduction in training time as only one estimator is built; the resulting estimator is also usually better at generalizing to other datasets. Performance of DTR is shown in Figure 5.2.

While decision trees do not generally have a problem with large bias, it is easy to overfit the data set, especially if the decision tree is deep. They can be unstable due to small variations in the data, because a completely different tree can be generated if the algorithm is too sensitive. However, these drawbacks can be avoided by using ensemble methods. Ensemble methods use multiple learning algorithms in conjunction to improve performance over what is possible with a single method. Methods to correct for overfitting are to include a random forest approach (decision tree forests), and to include gradient boosting (boosted decision tree), which will be discussed further in this chapter.

Boosted decision trees allow for many iterations over the same tree while minimizing a loss function at each iteration. The boosted decision tree used in this work is Adaboost [47] which fits a sequence of weak learners, or models that are only slightly better than random guesses, on repeatedly modified versions of the data. The final prediction is made with a weighted sum of all predictions.

The data are modified at each boosting iteration by applying a weight to each training sample. Initially, the weights are  $w_i = 1/N$  so that the first step is training on the original data. At each iteration, each weight is modified such that training examples that were not predicted correctly by the boosted model of the previous step have increased weights, and those that were predicted correctly have a decreased weight. The learning algorithm is then reapplied the reweighted data. The end result is that examples that are particularly difficult to predict get the largest weights, and each subsequent learner is forced to concentrate on examples poorly reconstructed by the previous ones [53]. Performance of the Adaboosted-DTR algorithm is shown in figure 5.3. The boosting is performed 100 times.

## 5.4 Validation Methods

There are many methods to quantify the quality of the predictions, both during the training and after testing. The methods used within the DTR and Adaboosted-DTR algorithms to optimize their performance, as well as the method used to test the quality of the predictions on the testing set, are detailed here.

### 5.4.1 Cross-Validation

Though splitting the data into testing and training sets will improve the ability of the algorithm to generalize to other data sets, it is still possible to overtrain the algorithm on the testing set, changing the parameters of the training such that the training set is perfectly predicted. In this case, it can be beneficial to reserve more data for a validation set, so that the algorithm can be tested and tuned to work well with the validation set, and tested on the testing set after all parameter tuning has been completed.

However, holding back a validation and a testing set requires leaving a large portion of the data out of the training, and is not always possible for datasets with low statistics. Cross-validation approaches have been developed in this case, so that the training data can be validated before the learner is applied to the testing set. The basic approach is a  $k$ -fold cross-validation in which the training set is split into  $k$  smaller sets. The model is trained using  $k - 1$  of the folds as training data. The resulting model is tested on the remainder of the data. The performance measure is the average of the values computed in the loop. This is easily implemented in the scikit-learn `cross_val`

package, which allows for  $k$ -fold cross-validation of all algorithms, as well as other cross-validation methods.

### 5.4.2 Mean Squared Error

The mean squared error (MSE) function is the risk metric that corresponds to the expected value of the squared error loss. The DTR algorithm uses this function as the feature selection criterion to reduce variance. For continuous targets, for node  $m$ , which represents a region  $R_m$  with  $N_m$  observations, MSE is:

$$c_m = \frac{1}{N_m} \sum_{i \in N_m} y_i H(X_m) = \frac{1}{N_m} \sum_{i \in N_m} (y_i - c_m)^2 \quad (5.5)$$

### 5.4.3 Coefficient of Determination

The coefficient of determination, or  $R^2$ , indicates how well the data fit a particular statistical model. If  $\hat{y}_i$  is the predicted value of the  $i$ -th sample, and  $y_i$  is the corresponding true value,  $R^2$  estimated over  $n_{samples}$  is defined as

$$R^2 = 1 - \frac{\sum_{i=0}^{n_{samples}-1} (y_i - \hat{y}_i)^2}{\sum_{i=0}^{n_{samples}-1} (y_i - \bar{y})^2} \quad (5.6)$$

where  $\bar{y} = \frac{1}{n_{samples} \sum_{i=0}^{n_{samples}-1} y_i}$ . The best possible score is 1; the score may be negative if the algorithm is being used to predict data types that were not included in the training set. The scikit-learn package uses this scoring function as a default to calculate how well the algorithms perform on the testing set.

## 5.5 Results

To test the performance of these algorithms, we construct a data set of events with one scintillation cluster and one charge cluster. The features used are the 74 APD channel signals, U-wire channel signals, and the  $z$ -position. The targets are the  $x$ -position,  $y$ -position, and corrected scintillation counts. We present the results of the algorithm as the difference between the truth values of the targets from the testing set and the machine-learned target values for the  $x$ - and  $y$ -positions, and as the standard error on the corrected scintillation counts. Each set of results is fit with two Gaussians, and is shown on a log scale to show the agreement in the tails.

The results from the OLS method are shown in Figure 5.1. These results are fairly mediocre, but the algorithm performs surprisingly well for being restricted to a linear fit. However, the DTR algorithm greatly outperforms the OLS method, shown in Figure 5.2. The downside to the DTR method is that the method uses only one tree, which is maximally overtrained to get the best results on the training set. This causes a poorer performance on the testing set, as it cannot generalize well. This is shown in the results of the Adaboosted-DTR in Figure 5.3. Because the Adaboosted-DTR method requires that the learner changes over every iteration of the boosting, it reduces the variance of the fit, and improves the performance of the learner on the testing set. For this reason, we continue the analysis using only the Adaboosted-DTR.

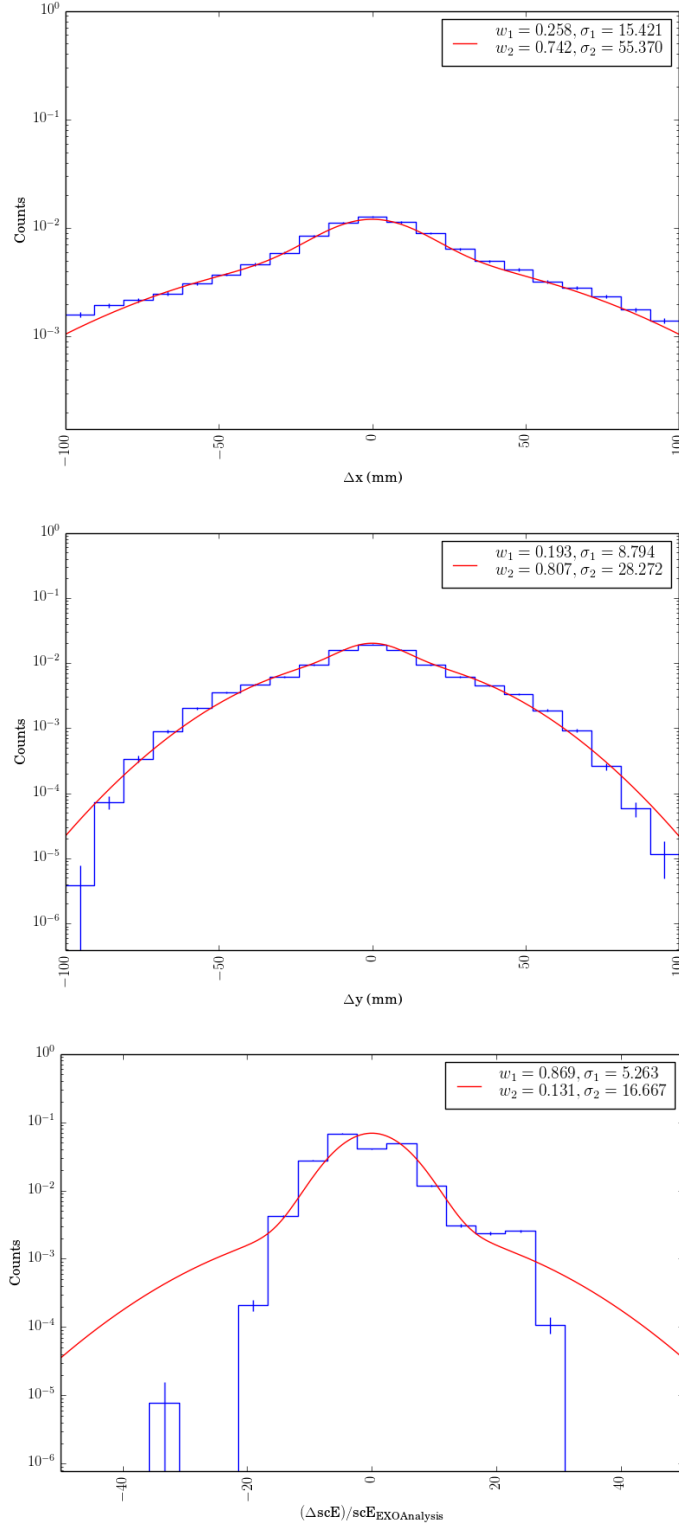


**Figure 5.1:** Differences between the OLS machine learned output and the truth values for the testing set. The fit is a two Gaussian fit, with the weights and  $1 \sigma$  values of each Gaussian shown. This algorithm does not perform as expected on the corrected scintillation counts, as the two Gaussian fit does not properly describe these results. The coefficient of determination is 0.8167.

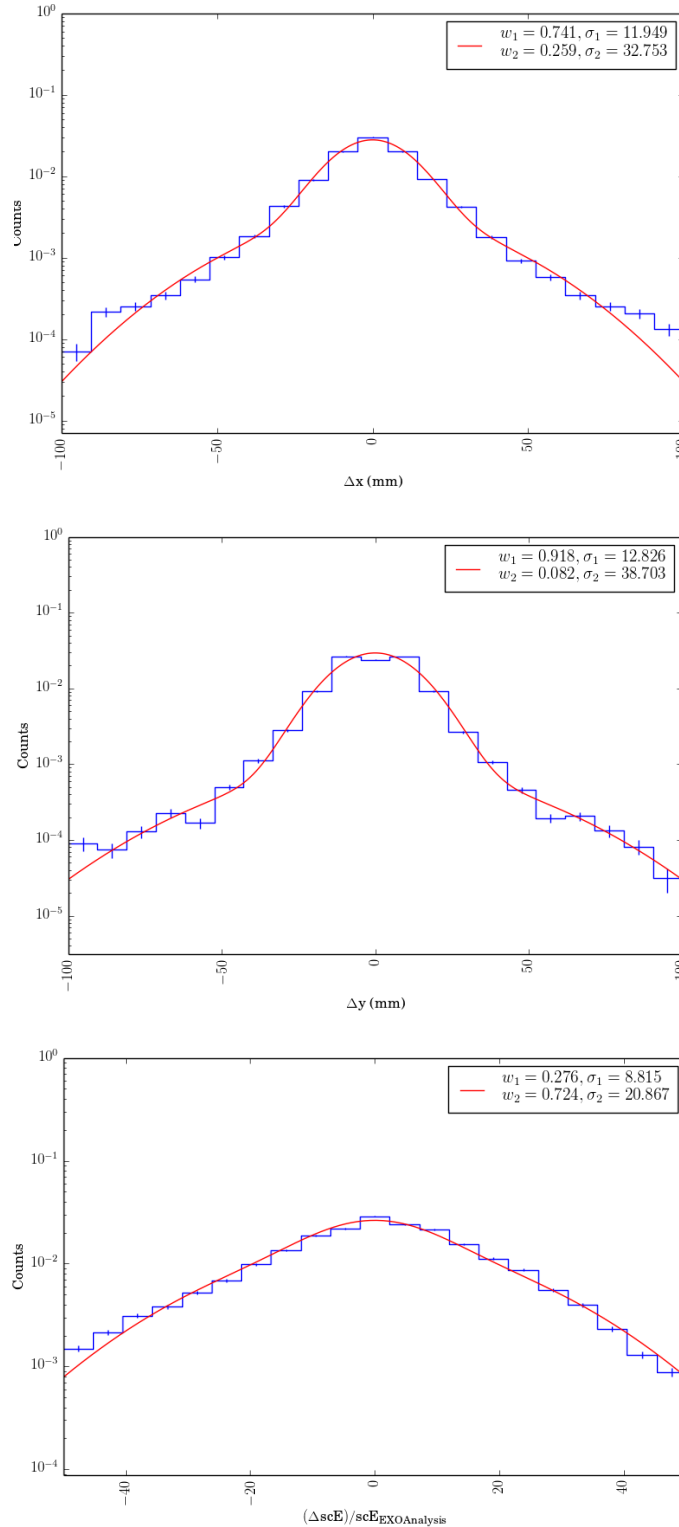


**Figure 5.2:** Differences between the DTR machine learned output and the truth values for the testing set. The fit is a two Gaussian fit, with the weights and  $1\sigma$  values of each Gaussian shown. The coefficient of determination is 0.945.

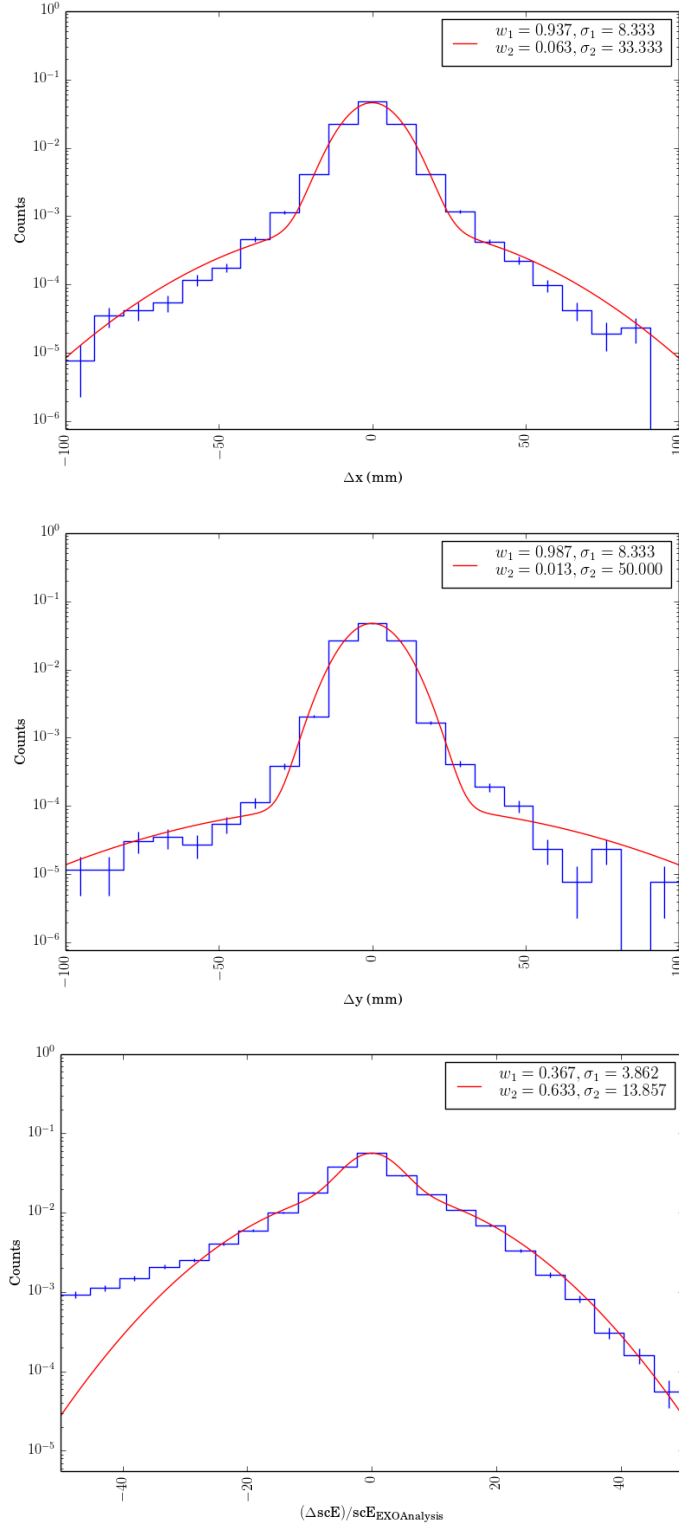


**Figure 5.3:** Differences between the Adaboosted-DTR machine learned output and the truth values for the testing set. The fit is a two Gaussian fit, with the weights and  $1 \sigma$  values of each Gaussian shown. Each variable must be trained and testing separately as the Adaboost method does not allow for multi-output; the coefficients of determination are:  $R_x^2$ : 0.984;  $R_y^2$ : 0.992;  $R_{scE}^2$ : 0.952.

## Chapter 6: Alpha Ion Studies

Reducing and constraining backgrounds is of utmost importance to the  $2\nu\beta\beta$  and  $0\nu\beta\beta$  analyses. It is particularly important to understand the contribution of  $^{222}\text{Rn}$  and its progeny to the overall background (discussed in detail in [14]). This is due to  $^{214}\text{Bi}$ , which has a  $\gamma$  line at 2448 keV, near the  $\beta\beta$  Q-value, as seen in Figure 6.1.

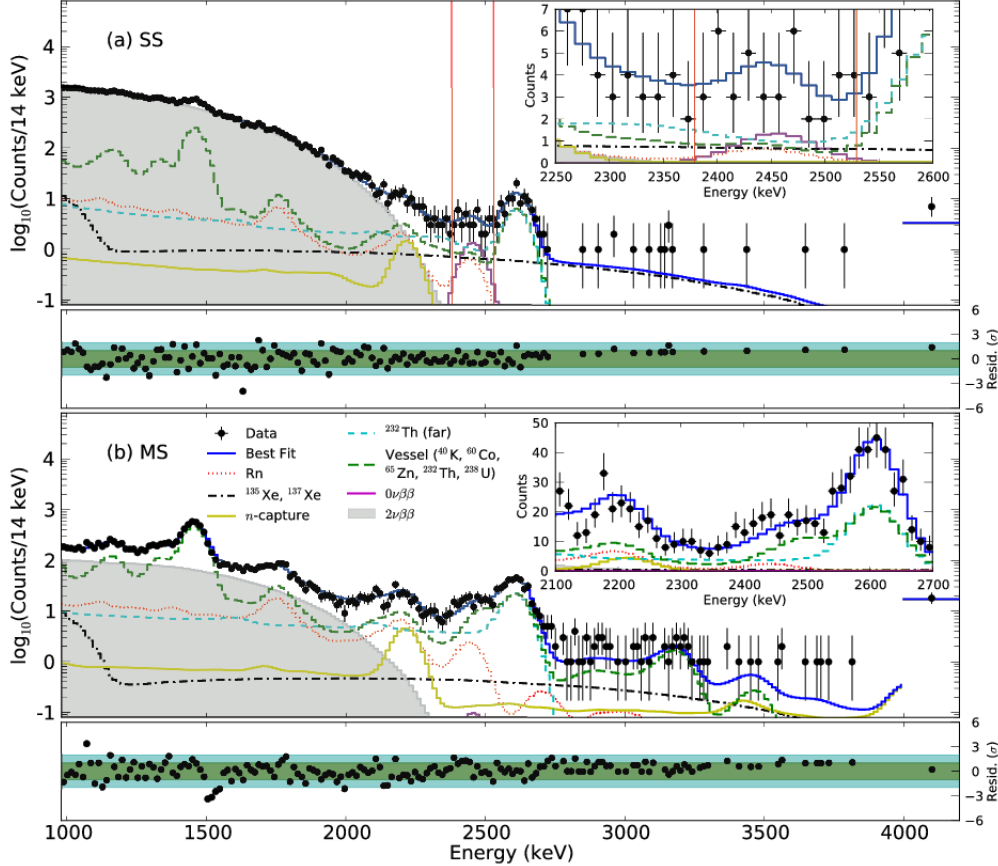


**Figure 6.1:** Summed electron energy for (a) single-site events and (b) multi-site events. Insert is zoomed into  $0\nu\beta\beta$  decay region of interest. The vertical red lines in the SS spectrum show the  $\pm 2\sigma$  region of interest. Within the region of interest is the 2448 keV  $\gamma$  line from the  $^{214}\text{Bi}$  decay [35].

The combination of scintillation and ionization signals allows for excellent particle discrimination, illustrated in Figure 6.2. Ionization energy from  $\beta$  decays is large, while the scintillation signal is small. In contrast, the ionization signal from  $\alpha$  decays is low, while the scintillation signal is large. This is due to the high density of the ionization cloud when the  $\alpha$  decay occurs, leading to more recombination and therefore fewer electrons being collected at the U-wires.

For events that are fully reconstructed, as in Figure 6.2(b), the different populations of the  $^{222}\text{Rn}$  progeny are distinguishable. These decays are shown as three separate peaks with mean scintillation counts of 38766, 42377, and 54254 counts for  $^{222}\text{Rn}$ ,  $^{218}\text{Po}$ , and  $^{214}\text{Po}$  decays, respectively [15], shown in region A. Events that occur in region B are  $\alpha$  decays that occur on or near the surfaces of

the TPC (cathode, anodes); due to the proximity to these surfaces, the electric field in these areas differs from the constant electric field over the rest of the TPC, and the charge and scintillation signals of these events become distorted. Because of this smearing, we restrict the  $\alpha$  events used in this analysis to those in region A. Region C are the  $\beta$  and  $\gamma$  events. We remove region C with a cut of (raw scintillation counts / purity corrected charge energy)  $< 33.864$ .

While the populations of  $^{222}\text{Rn}$ ,  $^{218}\text{Po}$ , and  $^{214}\text{Po}$  are well-defined using the light map corrected scintillation energy, this necessarily excludes events that do not have a fully reconstructed 3D position. This is because the light map correction is a position-based correction to the scintillation energy, so it requires that there is a reconstructed position to which the correction can be applied. Events that do not have a V-wire signal do not have a reconstructed  $x$ - and  $y$ -position; therefore the number of corrected scintillation counts is set to 0. Lack of V-wire signal is due to the ionization energy of the decay falling below the V-wire threshold of  $\sim 200$  keV. Due to the large amount of recombination, the  $\alpha$  events tend to be within the range of 100-300 keV, and therefore not all  $\alpha$  events produce a V-wire signal. These events are not included in Figure 6.2(b).

Due to the low background nature of EXO-200, the populations of  $^{222}\text{Rn}$  and its progeny are always low; to expand our data set as much as possible, we are required to use events that have had no corrections applied to the scintillation counts. These uncorrected events are shown in Figure 6.2(a). The populations are not well-defined here; however, region A, between 28000-50000 raw scintillation counts, corresponds to the populations of  $^{222}\text{Rn}$  and  $^{218}\text{Po}$ . For the following analysis, which focuses solely on  $^{222}\text{Rn}$  and  $^{218}\text{Po}$ , we define “bulk events” as those that have between 28000-50000 raw scintillation counts, with a purity corrected charge energy  $< 210$  keV, and  $20 < |z| < 172$  mm.

## 6.1 Application of Machine Learning Techniques

It is beneficial to have the fully reconstructed positions for the  $\alpha$  events that do not have a V-wire signal. To reconstruct the positions of these events, we use the Adaboosted-DecisionTreeRegressor (ADTR), the boosted decision tree algorithm discussed in chapter 5. The data set used for the training and testing sets are events that fall into Regions A and B in Figure 6.2; these are events with one scintillation cluster and one charge cluster. These events are taken from the Run2 data set, used for the most recent  $0\nu\beta\beta$  analysis [35], along with some additional runs not included in the  $0\nu\beta\beta$  analysis due to reduced purity. These low-purity runs were close in time to xenon feeds, in which xenon that has not been recirculating through the purifiers is fed into the system. While the purity is too low to be included in the  $0\nu\beta\beta$  analysis, we include them here because the radon content also increases during these times, which is beneficial for this analysis. The total livetime for this data set is 572.8 days [15].

The total number of one scintillation cluster, one charge cluster events in the overall dataset is 215434. Out of these, 90118 events are fully reconstructed and can be used for training and testing; 70% of these are used for training, with 30% being reserved for testing. The features for each event are the 74 APD channel signals, the U-wire signal, and the  $z$ -position; the targets are the  $x$ - and  $y$ -positions, and the corrected scintillation counts. While the corrected scintillation counts are not explicitly used in this analysis, it provides a good crosscheck for the energies of the  $^{222}\text{Rn}$  and  $^{218}\text{Po}$ , which ensures that the results from ADTR are not unphysical.

## 6.2 Coincidence Technique

A method of studying  $\alpha$  decays is to look for coincidences of two decays. The viable coincidences for this study,  $^{222}\text{Rn}$  and  $^{218}\text{Po}$ , are shown in red in Figure 6.4. We investigate only these because of the short half-life (3.1 minutes) of the second day, making it relatively easy to associate the decays with few false coincidences. In general, investigating the  $^{214}\text{Bi}-^{214}\text{Po}$  coincidences is also viable, however, we restrict this analysis to  $\alpha-\alpha$  coincidences only as the  $^{214}\text{Bi}-^{214}\text{Po}$  coincidences often occur in the same event frame due to the short half-life of  $^{214}\text{Po}$ , which complicates using ADTR to reconstruct event positions.

For this analysis, we restrict the coincidence candidate events used to be bulk events only, which have the most reliable energy information due to being far from the cathode and anodes, and allows

for a direct comparison to previous work, which utilized bulk events. Again, these events have between 28000-50000 raw scintillation counts, a purity corrected charge energy of  $<210$  keV, and  $20 < |z| < 172$  mm.

To be considered a coincidence, two candidate events must occur no more than 3 minutes apart, and have a charge signal on the same or adjacent U-wire or have an ADTR-reconstructed  $x - y$  separation of no more than 30 mm. The half-life of the  $^{218}\text{Po}$  decay is 3.1 minutes; the time coincidence is set to a similar scale to minimize the acceptance of false coincidences. The events are not expected to drift far apart radially, so the events are required to land on either the same or adjacent U-wire. Previous work has shown that using this requirement restricts the false coincidence probability to  $<2\%$  [15]. However, this is a particularly stringent requirement, as the U-wires are only 9 mm apart. Because an  $x - y$  separation of 30 mm is considered to be characteristic of a valid coincidence [15], we also include events that occur within this radial distance,  $R_{\text{ADTR}} < 30\text{mm}$ , based on their ADTR-reconstructed positions.

Using  $R_{\text{ADTR}} < 30\text{mm}$  as the requirement for coincidences, we find 6632 coincidences, compared to 6431 using the U-wire requirement only. The previous results for this analysis using the U-wire requirement only resulted in 6507 coincidences; these numbers differ here due to differences in the way ambiguous coincidences are handled. Previously, coincidences for which the first event could be coincident with more than one other event within 180s were classified as ambiguous and removed. Here, ambiguous coincidences are any coincidences for which the second event is coincident with another event within 180s; this removes the possibility of accidentally including a coincidence in which the second event could also be coincident with another event.

Combining the results of the  $R_{\text{ADTR}}$  and U-wire requirement, we find a total of 6785 coincidences. This is a 5.5% increase in the data set from using the U-wire requirement alone.

To determine the probability of accepting a false coincidence based on the  $R_{\text{ADTR}}$  requirement, we use coincidences with both events fully reconstructed by the EXO Analysis software. Coincidences found to be within  $R < 30\text{mm}$  are taken to be true coincidences; we find that there are 296 such coincidences. The  $R_{\text{ADTR}}$  requirement finds 297, constructing 1 false coincidence. The U-wire requirement finds 287 coincidences, missing 11 true coincidences and falsely reconstructing 2. The combination of the  $R_{\text{ADTR}} < 30\text{mm}$  and  $U \leq 9\text{mm}$  requirements, therefore, constructs 2 false coincidences out of 298 total coincidences found with fully reconstructed events ( $<1\%$ ). Because of the small data set available to test for false coincidences, we conservatively set the false coincidence probability to 1%.

The differences between  $x_{\text{ADTR}}$  and  $y_{\text{ADTR}}$  and their respective truth values, shown in Figure 5.3, are fit with two Gaussians; however, because of the high weight of the narrower Gaussian for set of differences, we approximate these errors to be Gaussian and use  $\sigma_1$  as the errors on  $x_{\text{ADTR}}$  and  $y_{\text{ADTR}}$ . Adding these in quadrature, we find an error on the radial distance for each event to be 9.279 mm. This more than likely contributes to the construction of false coincidences throughout the set.

The coincidences are ordered in time only; to check the validity of this matching, we crosscheck the energies of the events within the coincidence. All but 77 coincidences have the first event having less ADTR-reconstructed scintillation energy than the second event, and for these the difference between the energies is on the same order as the error on the ADTR-reconstructed scintillation counts. Both raw and ADTR-reconstructed corrected scintillation counts versus  $z$ -position are shown in Figure 6.5. Though using the corrected scintillation energies cannot definitively tell us whether ordering in time is sufficient for accepting coincidences, the ADTR-reconstructed corrected scintillation energies do correctly implement the light map corrections, which shows that the results of ADTR are not unphysical.

### 6.3 Ion Velocity

Behavior of ions in LXe is of particular interest for nEXO, the next-generation EXO experiment, which will be scaled up to about 5 tonnes of LXe. A possibility for nEXO is the idea of barium tagging, in which the daughter  $^{136}\text{Ba}$  ion can be identified and extracted from the LXe upon  $^{136}\text{Xe}$  decay. The ability to do this would eliminate all backgrounds other than the background from  $2\nu\beta\beta$

decay [94], [75]. However, there are still some questions about barium tagging in LXe that need to be answered before it can be implemented. These questions include characterizing how the barium moves in the detector over the amount of time it would take to capture it. We can contribute some information to these questions by measuring the ion velocity of the charged  $^{218}\text{Po}$ . By taking the electric field into consideration we can calculate a mobility for the  $^{218}\text{Po}$  ions. This is also why we do not include the events that occur close to the cathode and anodes into this analysis and instead only choose a range in  $z$  where the electric field is constant.

With coincidence information, the  $^{218}\text{Po}$  drift distance and time can be calculated. The drift distance is simply the  $\Delta z$  between the two events; the drift time is the  $\Delta t$  between the two events. The drift time versus the drift distance is shown in Figure 6.6. Positive displacement in  $z$  is designated as toward the cathode. There are two populations: neutral  $^{218}\text{Po}$  that do not drift far, and ionized  $^{218}\text{Po}$  that drift toward the cathode. The mean velocity of  $^{218}\text{Po}$  is shown in Figure 6.7.

There are 77 events that fall outside of the range  $[-1,3]$  mm/s; note that these are events are not part of the coincidences with the first event having a higher number of ADTR-reconstructed corrected scintillation counts. We reject the coincidences with clearly unphysical ion velocity on the ground that they are either physically correlated but poorly reconstructed due to the position errors associated with using ADTR, or altogether physically uncorrelated. This is 1.13% of the coincidences that we have reconstructed, which is what was expected based on the estimate of the false coincidence probability. We therefore restrict our analysis to be within  $v = [-1,3]$  mm/s to exclude these false coincidences.

The peak for the ion velocity is rather broad; previous work finds two ion velocities for this population. The average ion velocity decreases as the  $^{218}\text{Po}$  drift time increases, which can be seen in Figure 6.8. This is possibly explained that the  $^{218}\text{Po}$  ions initially move with a velocity  $v_1$  and while drifting, a reaction or charge transfer occurs resulting in a larger molecular ion or reduction of the charge of the ion, at which point the ion moves with a lower drift velocity  $v_2$ . The velocity distributions of data sets with different electron lifetimes are compared, and a model generated to include both velocities, the electron lifetime, the ion reaction and neutralization time constants, and a diffusion constant. The best fit velocities for this model with  $1\sigma$  errors are  $v_1 = 1.48 \pm 0.01$  mm/s and  $v_2 = 0.83 \pm 0.01$  mm/s.

The best fit velocity with  $1\sigma$  errors from this analysis is  $v = 1.153 \pm 0.42$  mm/s. The large errors on this measurement suggest that the model that gives two separate ion velocities is correct, as both velocities fall into the range given by the  $1\sigma$  values. Despite the large errors, this measurement is consistent with the previous work.

## 6.4 $^{218}\text{Po}$ Ionization Fraction

To avoid biasing toward neutral  $^{218}\text{Po}$ , a  $\Delta t$  cut is introduced to remove any events that, were the  $^{218}\text{Po}$  ionized, would have drifted out of the detector volume. We calculate this using a maximum drift velocity of 2.5 mm/s

$$\Delta t = z_{Rn} / (2.5 \text{ mm/s}) \quad (6.1)$$

where  $z_{Rn}$  is the location of the  $^{222}\text{Rn}$  decay, and therefore the starting point for the  $^{218}\text{Po}$  drift. Using a maximum drift velocity of 2.5 mm/s, 2584 coincidences remain. 1303 of these events are between 0.5 mm/s and 2.5 mm/s, giving a  $50.4\% \pm 1.7\%$  ionization fraction, where the error is statistical. This is in agreement with the ionization fraction previously reported, which was  $50.3\% \pm 3.0\%$ .

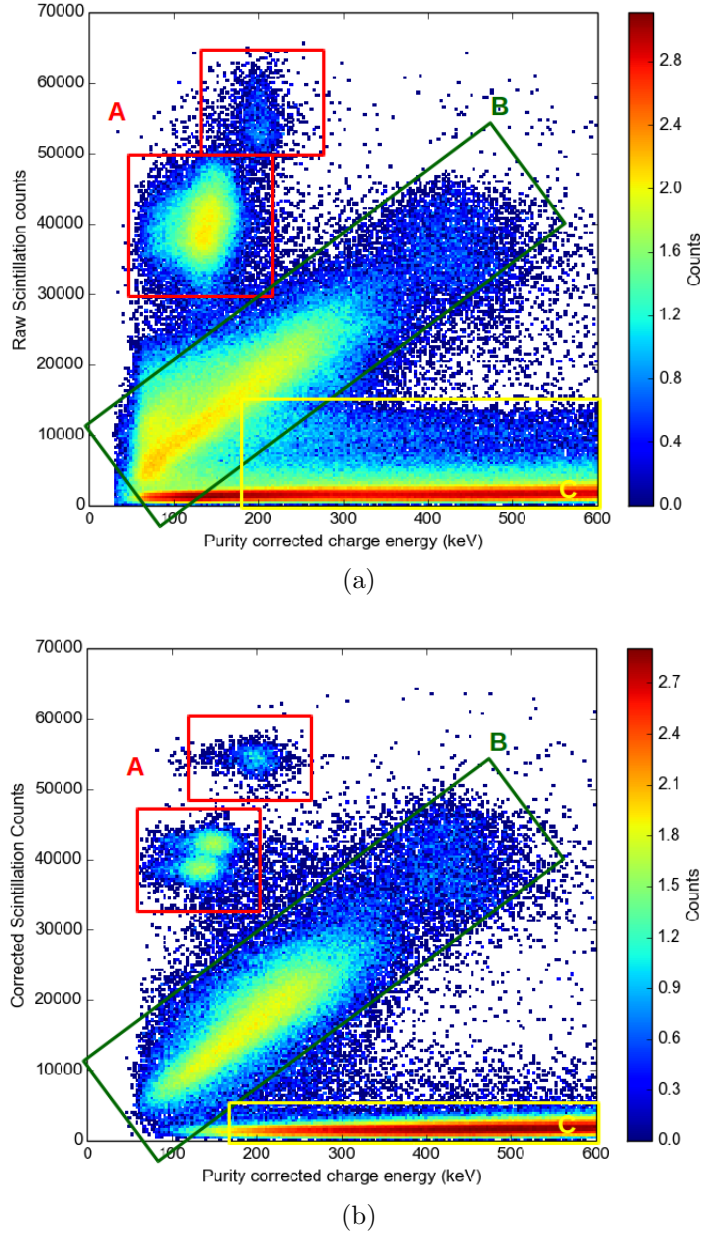
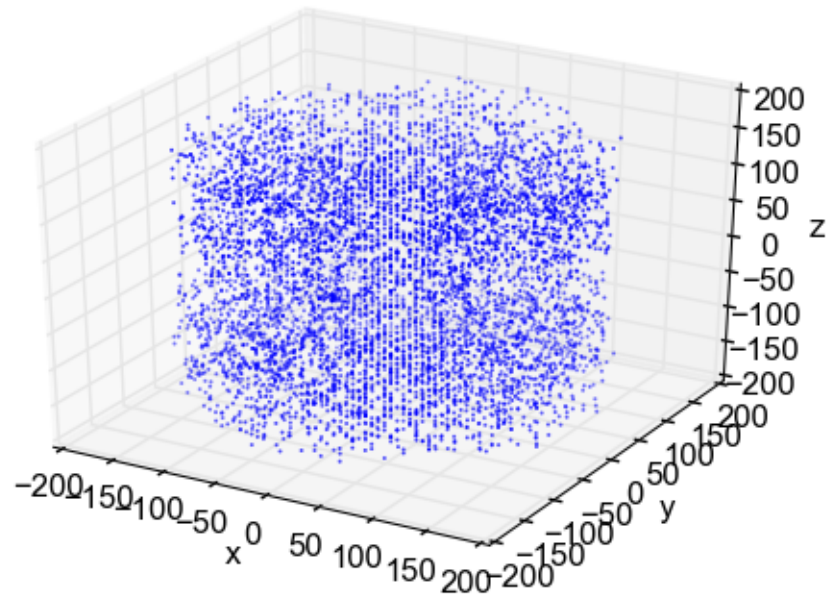
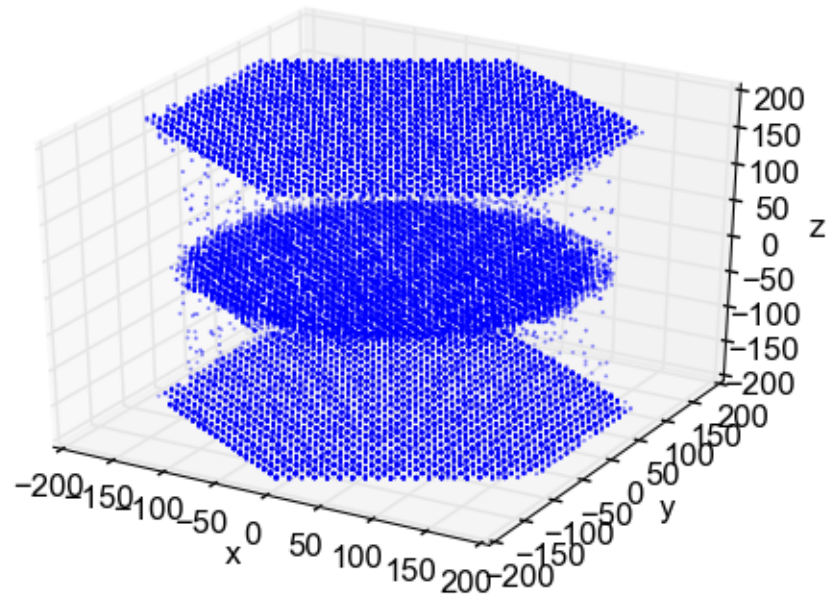


**Figure 6.2:** (a) Raw (before corrections are applied) scintillation counts and (b) corrected scintillation counts versus purity corrected charge energy. Only events that are fully position reconstructed have enough information to be corrected; therefore, events that do not have a V-wire signal are not included in (b). Region A, red, corresponds to bulk  $\alpha$  events; because this analysis handles events that do not have complete position reconstruction, bulk is defined as: between 28000 - 50000 raw scintillation counts, purity corrected charge energy less than 210 keV, and  $20 < |z| < 172$  mm. Once corrections are applied to the scintillation counts, the populations of  $^{222}\text{Rn}$  and its progeny can be seen with mean scintillation counts of 38766, 42377, and 54254 for  $^{222}\text{Rn}$ ,  $^{218}\text{Po}$ , and  $^{214}\text{Po}$ , respectively [15]. Region B, green, are  $\alpha$  decays that occur on surfaces; the signal is smeared such that they are not able to be identified based on their energies. Region C, yellow, are  $\beta$  and  $\gamma$  decays. There is less overlap in these regions in (b) due to the light map correction, which implements an  $z$ -position-dependent energy correction, allowing for a larger separation in populations of events.



A



B

**Figure 6.3:** Locations of events in region A and B as defined in Figure 6.2.

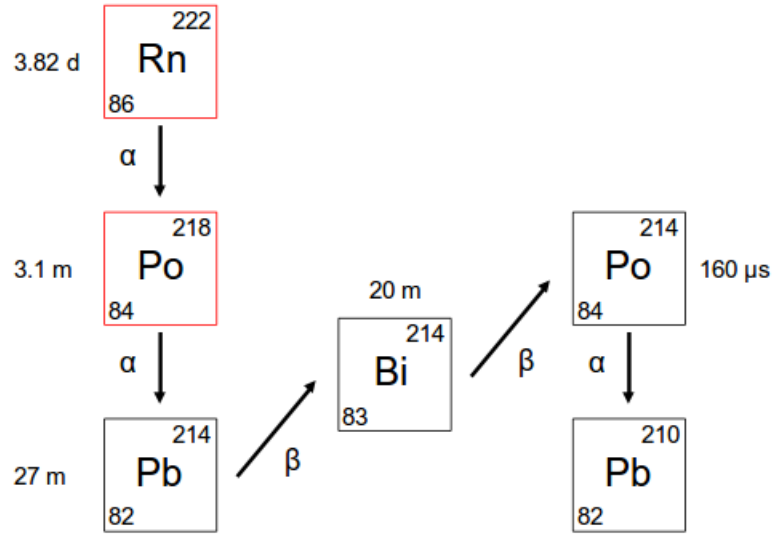


**Figure 6.4:** Radon decay chain, including half-lives of the decays. Highlighted in red are the progeny of interest for this work. Decays displayed vertically are  $\alpha$  decays, and decays moving toward the right of the figure are  $\beta$  decays.

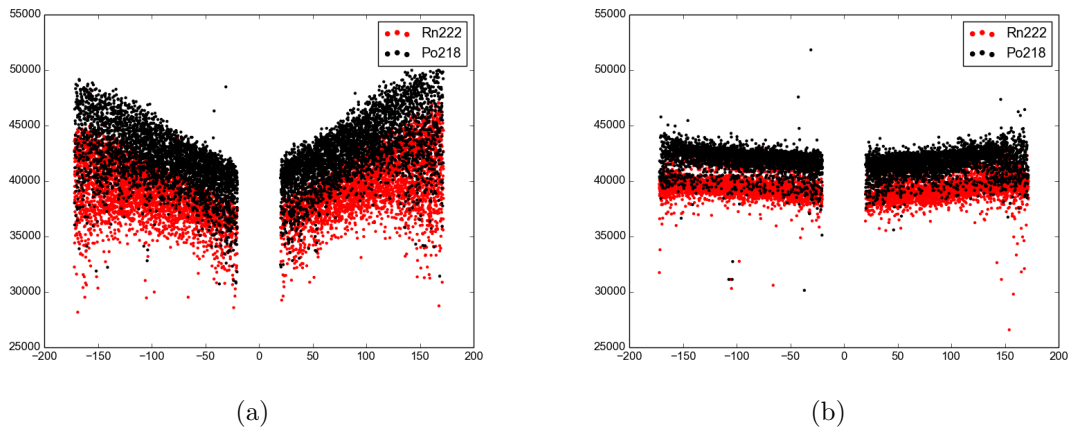


**Figure 6.5:** (a) Raw scintillation counts and (b) ADTR-reconstructed corrected scintillation counts versus  $z$  position of coincident pairs for events in the bulk; events assigned as  $^{222}\text{Rn}$  are in red and  $^{218}\text{Po}$  in black based on ordering in time. The ADTR-reconstructed corrected scintillation counts shows a reduction in the  $z$ -position dependence of the scintillation energy; this lends confidence to using the ADTR method for this work.

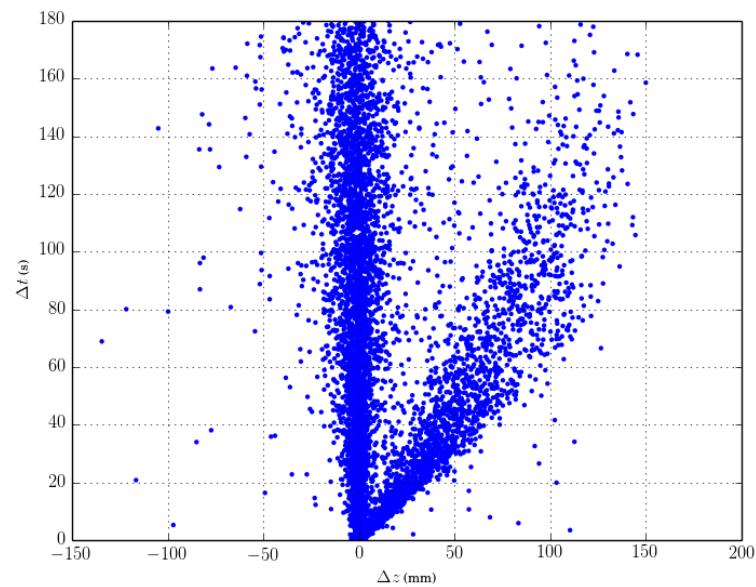


**Figure 6.6:**  $^{218}\text{Po}$  drift time versus drift distance. The population at  $z = 0$  are neutral  $^{218}\text{Po}$ , which do not drift a long distance before decaying. The population in  $+z$  are  $^{218}\text{Po}$  ions. Positive displacement is movement toward the cathode.

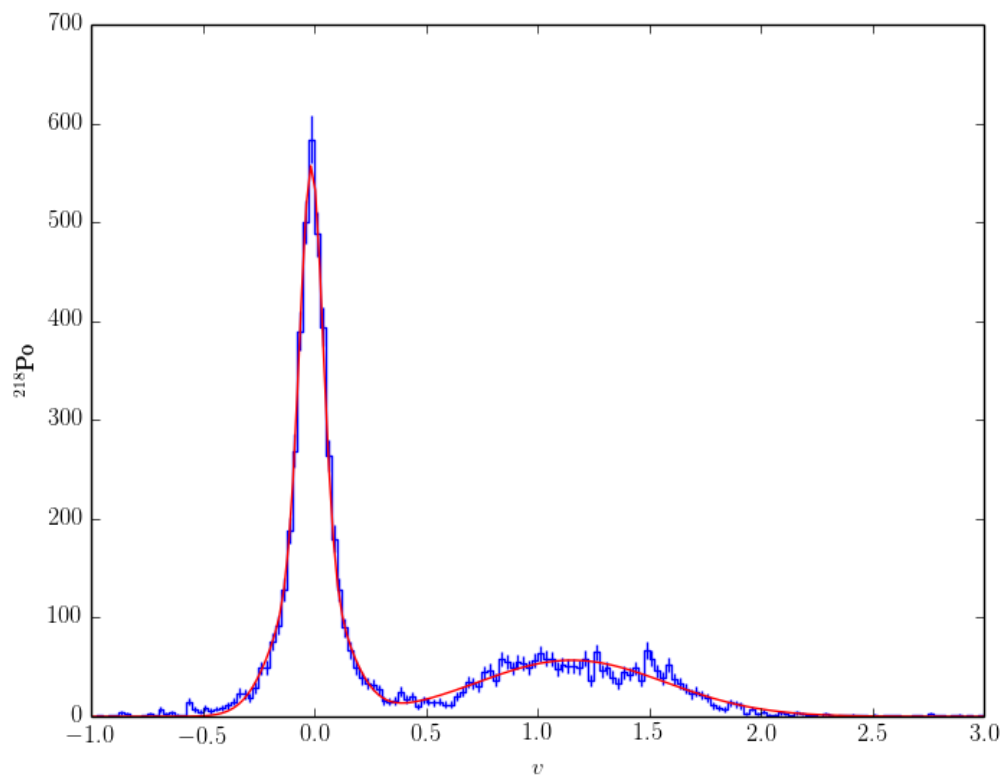


**Figure 6.7:** Mean velocity of  $^{218}\text{Po}$  atoms and ions. Gaussian fit gives a mean ion velocity of  $v = 1.153 \pm 0.42$  mm/s where the error is the  $1\sigma$  value of the fit.

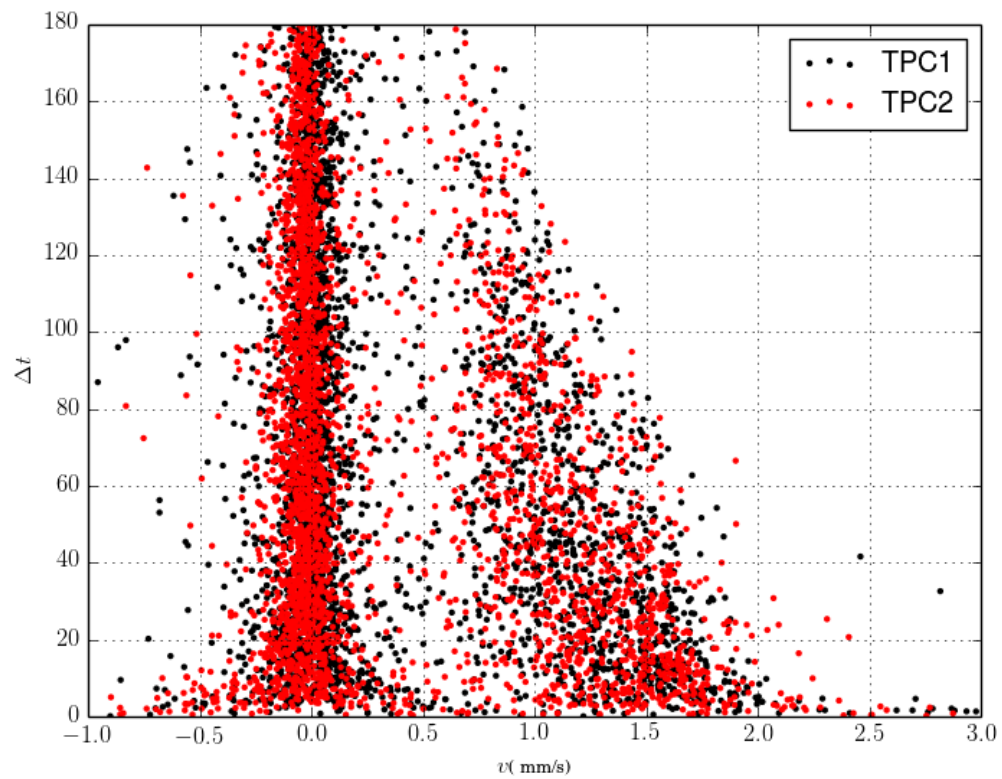


**Figure 6.8:**  $^{218}\text{Po}$  drift time versus  $^{218}\text{Po}$  drift velocity. The ion velocity decreases as the drift time increases. This points to the possibility of two ion velocities.

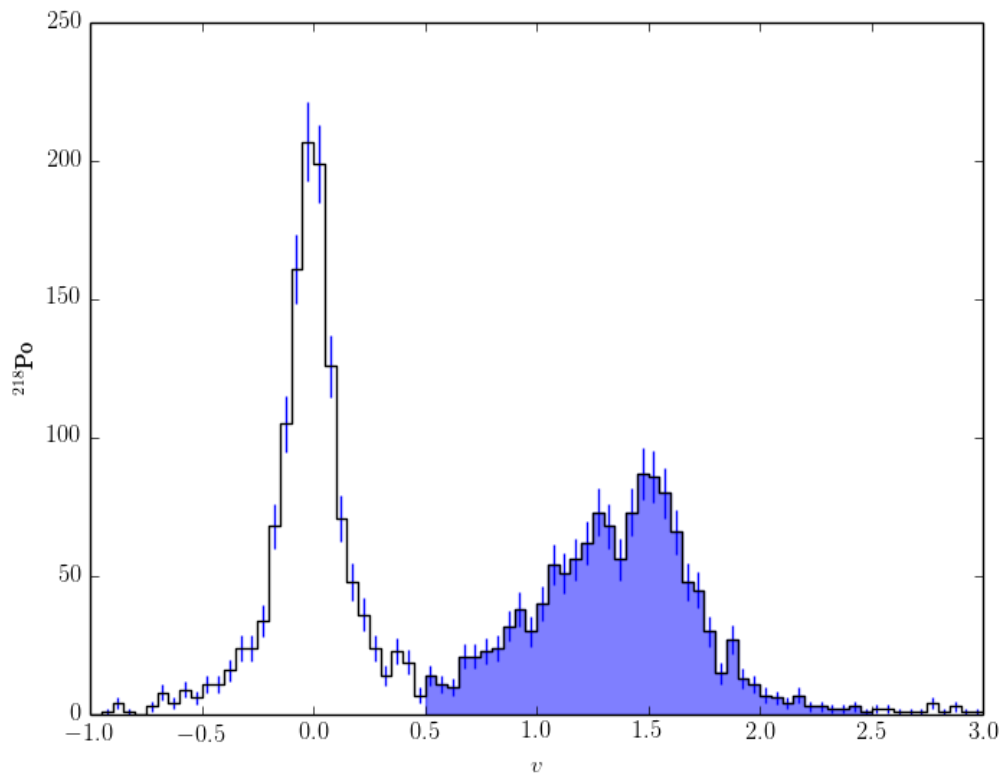


**Figure 6.9:** Velocity of  $^{218}\text{Po}$  that passes the  $\Delta t$  cut that is implemented to avoid biasing toward neutral  $^{218}\text{Po}$ . This cut eliminates events that, were they charged, would have drifted out of the analysis volume. The blue area, corresponding to  $v = 0.5\text{--}2.5 \text{ mm/s}$ , is integrated to determine the number of ions.

## Chapter 7: Surface Studies

It is possible to apply the fits from the Adaboosted-DecisionTreeRegressor (ADTR) to other types of events which do not have a position reconstruction, e.g. events that occur along the cathode, anodes, and Teflon reflectors along the walls of the LXe vessel, as long as these events are in the same range of raw scintillation counts so that ADTR provides valid predictions. We investigate events that have one scintillation cluster and one charge cluster (1CC) events that are not in the bulk, and events that have one scintillation cluster but do not have a charge cluster (0CC). The 0CC events are particularly interesting to investigate because there is no position information available at all due to the lack of U-wire signal. Using a technique not currently used in the EXO Analysis framework is the only way to reconstruct the positions of these events.

By reconstructing the positions of the surface events, we can investigate whether there are patterns or anomalies on the surfaces, which could point to the Teflon charging up, or “hotspots” on the Teflon reflectors due to contamination during cleaning and installation.

### 7.1 Motivation

Net electric charge is generated in liquids near solid surfaces or near interfaces between liquid and air. This can be a hazard, especially when involving liquid hydrocarbons that have a low electrical conductivity [61]. Many studies have been done on this to reduce the flow of charge, especially in gasolines and other flammable material, to decrease the risk of discharges and sparks. In particular, these problems arise with the flow of liquid hydrocarbons through filters or short pipes.

Consider a pipe of length  $L$  as shown in Figure 7.1. If a nonconducting fluid flows through this pipe with a mean velocity  $v$ , and has some initial charge  $q_i$  per unit length of pipe, this corresponds to a convection current  $I_i = q_i v$  entering the pipe. The liquid also leaves the pipe with some charge  $q_u$ , causing an exit current of  $I_u = q_u v$ . The value of  $I_u$  depends on the magnitude of  $I_i$ , the resistivity of the fluid, the time  $t$  that the fluid is within the pipe, and the amount of charge separation between the fluid and the pipe [93].

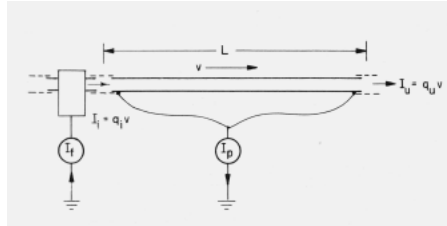


**Figure 7.1:** Electric current resulting from fluid flow [93].

When there is flow throughout the pipeline, the charge can be carried over large distances. It can also be discharged back to the pipe walls, reservoir, or component surfaces; the discharge rate is controlled by the characteristics of the fluid and its additives. The charge relaxation is described by

$$q_t = q_i e^{-\frac{t}{\tau}} \quad (7.1)$$

$$\tau = \frac{\epsilon \epsilon_0}{K} \times 10^{12} \quad (7.2)$$

where  $q_t$  is the charge at time  $t$ ,  $q_i$  is the initial charge,  $\tau$  is the charge relaxation time constant (37% charge decay),  $\epsilon$  is the dielectric constant of liquids,  $\epsilon_0$  is the absolute dielectric constant of a vacuum ( $8.854 \times 10^{-12}$  F/m), and  $K$  is the fluid rest conductivity (pS/m).

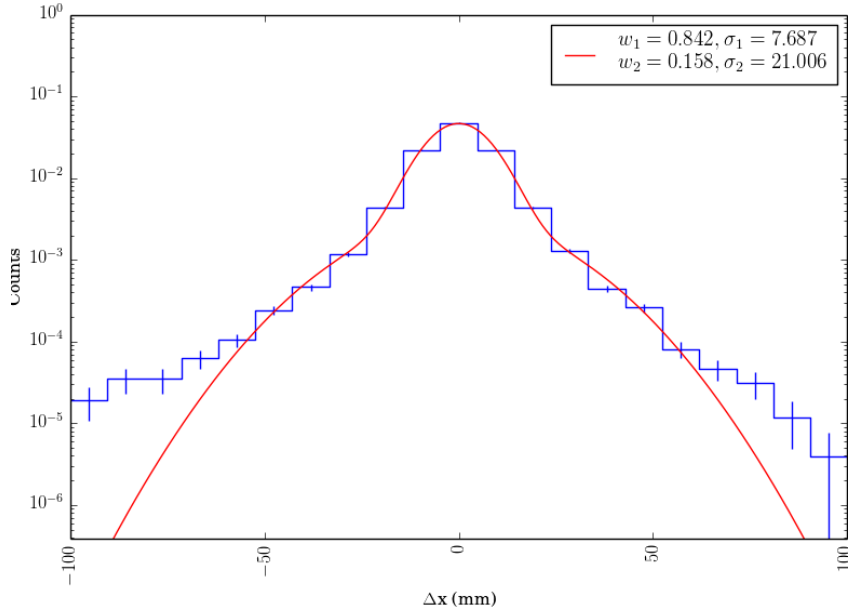


**Figure 7.2:** Difference in ADTR-reconstructed  $x$ -position and  $x$ -position for 1CC events reconstructed by the EXO Analysis software. The coefficient of determination is  $R_x^2$ : 0.983.

If the component walls are conductive, then a charge will be induced on the walls, which is of opposite polarity to the fluid. If the exterior surface is grounded, the net charge will be zero. If not, charge will accumulate on the surfaces and eventually discharge. This will generate an electrostatic discharge where the charge discharges to a surface at lower voltage. This happens especially with filters inside the pipe [60]. If the filter is made of a nonconductive material it will acquire a charge when the fluid charges. The charge will not be able to dissipate into the filtration system due to the high resistivity of the material. The filter will act as a capacitor and charge until the voltage is great enough to overcome the gap and discharge to a lower potential.

In the worst scenarios, this can cause a high-energy spark, and if this discharge happens in air, it could have harmful effects. For EXO-200, luckily, this is not a concern; however, it is possible that, as the xenon flows through the LXe vessel, the vessel acts as a pipe, and the cathode may act as a filter. If ions drift preferentially toward particular regions of the Teflon, this may point to some charging of the Teflon due to the xenon flow. By investigating the Teflon surfaces it may be possible to identify “hot spots” as well, indicating a dirty portion of the Teflon.

## 7.2 Training and Testing

For these studies, we train the ADTR on the same set of reconstructed alpha events as in chapter 6; however, since the reconstruction will be applied to events that do not have charge information, we perform a scintillation-only reconstruction using the 74 APD channels as features. The targets for this study are the  $x$ -,  $y$ -, and  $z$ -positions of the events, as well as the corrected scintillation counts. The scintillation-only reconstruction performs only slightly worse than the reconstruction that includes the charge information, which is not unexpected. The difference in positions, however, illustrated in Figures 7.2, 7.3, 7.4, and 7.5, increases only slightly.

For studying the detector surfaces we used two sets of data. First, we reuse the alpha-like events with one scintillation cluster and one charge cluster (1CC). However, for these studies we do not disregard the events that occur on the surfaces (i.e., outside of region A defined in Figure 6.2), though the bulk and surfaces are handled separately here.

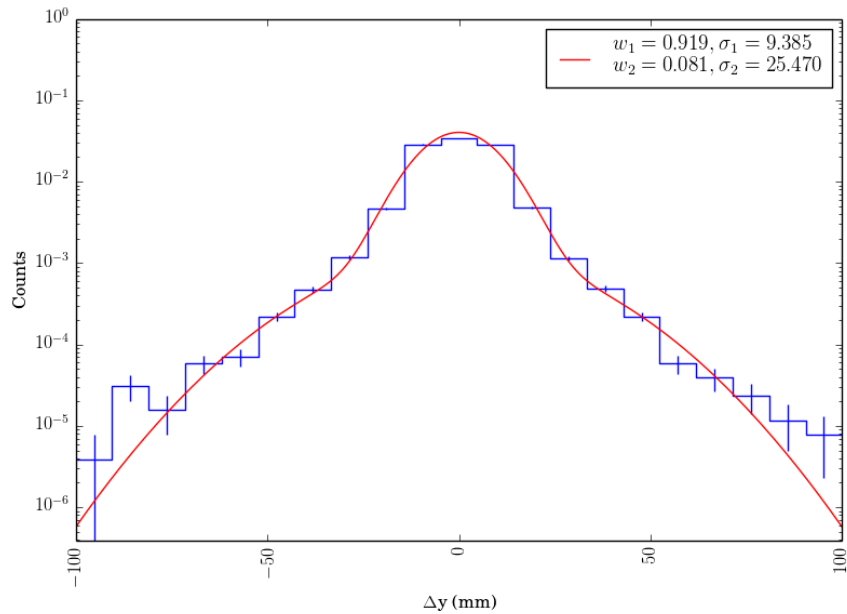


**Figure 7.3:** Difference in ADTR-reconstructed  $y$ -position and  $y$ -position for 1CC events reconstructed by the EXO Analysis software. The coefficient of determination is  $R_y^2$ : 0.984.

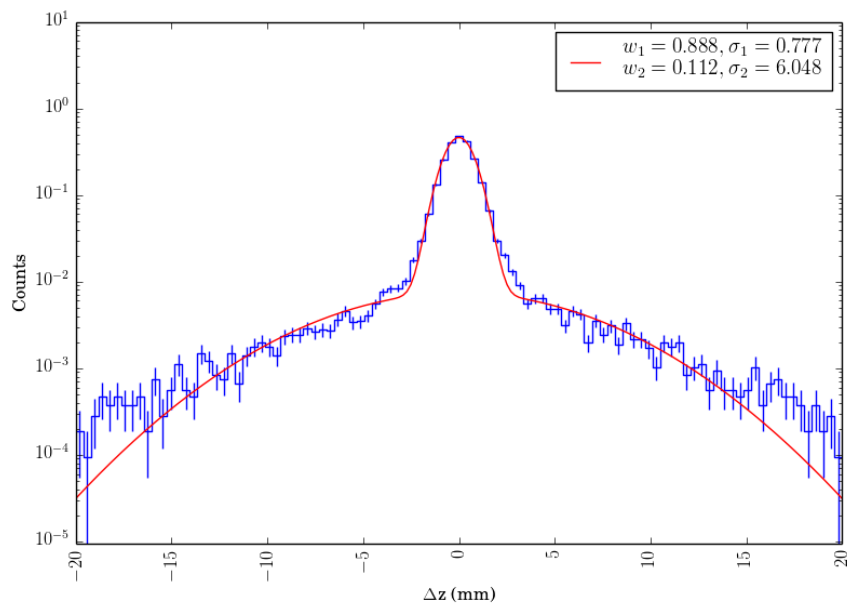


**Figure 7.4:** Difference in ADTR-reconstructed  $z$ -position and  $z$ -position for 1CC events reconstructed by the EXO Analysis software. The coefficient of determination is  $R_z^2$ : 0.998.

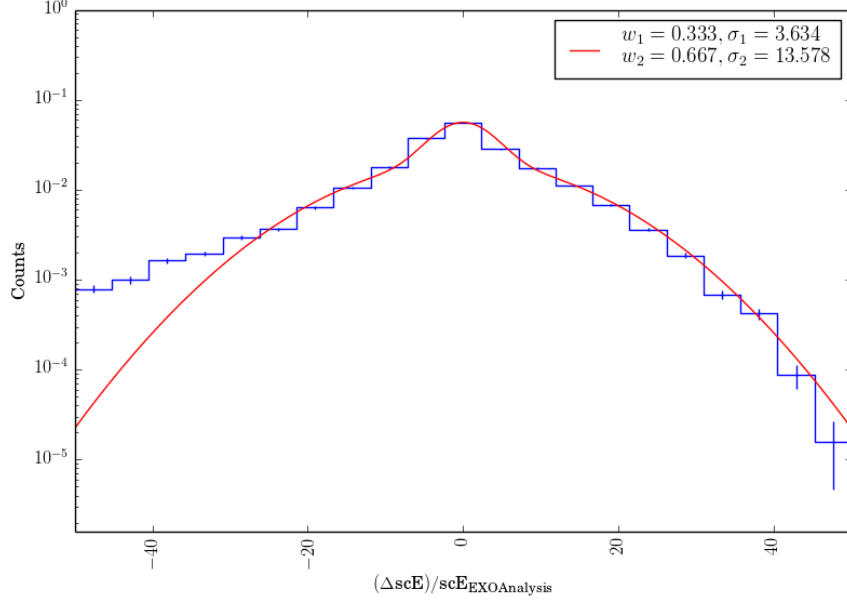


**Figure 7.5:** Difference in ADTR-reconstructed corrected scintillation counts and corrected scintillation counts for 1CC events reconstructed by the EXO Analysis software. The coefficient of determination is  $R^2_{scE}$ : 0.949.

Second, we study events that have one scintillation cluster, but no charge cluster (0CC). These events with no charge cluster are thought to be those that occur close to the Teflon, such that the ionization cloud is disrupted and therefore falls below even the U-wire threshold. Studying these events is inherently difficult because not only is no charge available to constrain the spatial reconstruction, but by definition there is no well-reconstructed data sample exist to tune more refined reconstructions. Monte Carlo reconstructions are not a possibility here for the same reason as in the alpha decay studies; that is, the scintillation signals are not well modeled in the EXO-200 Monte Carlo, and any training done on these signals would be unreliable. To ensure that the 0CC predictions are as valid as possible, we specifically choose the events that fall into the range of 28000-50000 raw scintillation counts, since we have already demonstrated that the ADTR results are trustworthy in this region.

### 7.3 1CC Events

The breakdown of the locations of the 1CC events is given in Table 7.1. We restrict the investigation of the events that occur at high radius to those that have a number of raw scintillation counts between 28000 and 50000, as these are the events for which ADTR has been verified. We split these events between those with a z-position between  $20 < |z| < 172$  mm; this is because the Teflon reflectors begin at 18.43 mm from the cathode, and the electric field varies close to the cathode and anodes, so we treat these areas separately. To investigate the region near the Teflon, we implement a radial cut at  $R = 172$  mm. We choose this radius because the Teflon reflectors are located at a radius of 183 mm with a width of 1.5 mm, with some overlap. The event radius, here, is calculated using the ADTR-reconstructed  $x$ - and  $y$ -positions.

Events outside of the fiducial  $z$  range are illustrated in Figure 7.6(a). We investigate these events separately from those that are inside the fiducial  $z$ , because the electric field is not necessarily uniform the closer the event is to the cathode or anodes. These events collect on the cathode and anodes, with slightly more on the cathode than either anode. The anodes have a similar number of events,

**Table 7.1:** Locations of 1CC events with raw scintillation counts in the range 28000-50000. Events used to investigate the Teflon reflectors are those that fall into the  $20 < |z| < 172$  mm &  $R > 172$  mm categories.

$R > 172$ mm	1097
$R < 172$ mm	48322
outside fiducial $z$	14834
$20 <  z  < 172$ mm	34585
$20 <  z  < 172$ mm & $R > 172$ mm	890
Total	49919

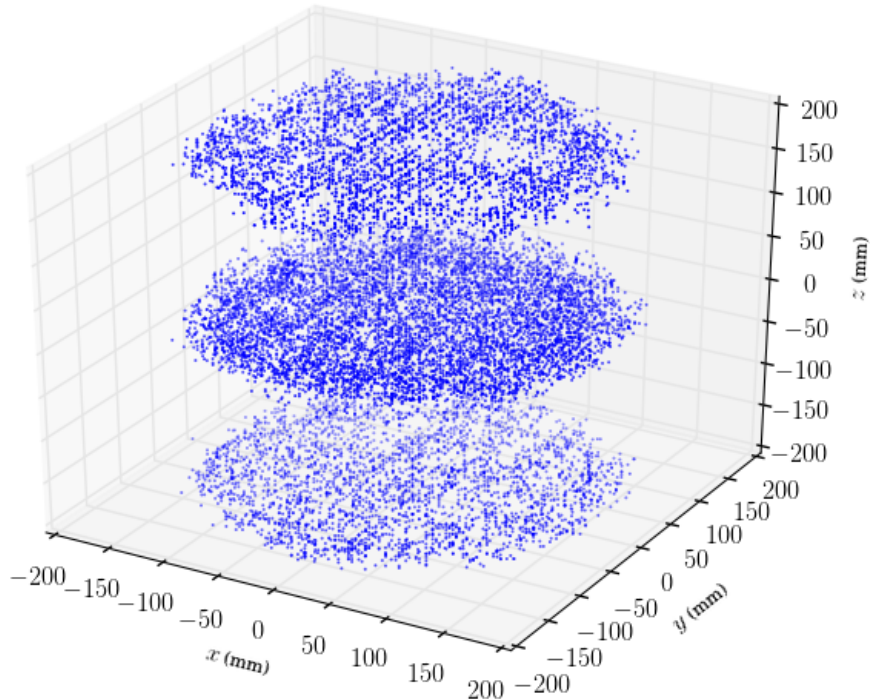


**Figure 7.6:** 1CC events outside of the fiducial  $z$ , without radial cuts applied. The accumulation of events on the cathodes and anodes is apparent here.

which is expected. Clustering on the cathode is especially expected, due to positively charged ions drifting toward the cathode and remaining there until they decay. There are no cuts on these events based on number of scintillation counts, so these events are not necessarily  $^{218}\text{Po}$ , and could be  $^{222}\text{Rn}$  progeny with a longer half-life.

The distribution of events within  $20 < |z| < 172$  mm and  $R > 172$  mm along  $z$  is shown in Figure 7.5. There appears to be more events in TPC2 than TPC1, however, with the low statistics it is difficult to make any determinations about the distributions.

## 7.4 0CC Events

The breakdown of the locations of 0CC events are given in Table 7.2. Again, all events considered here have between 28000 and 50000 raw scintillation counts, because events in this range of scintillation counts are the ones on which the ADTR is trained, and therefore the algorithm is most reliable. It is worth mentioning that, out of the total number of events in this range of raw scintillation counts, <1% are reconstructed with a radius greater than that of the detector. This serves as an excellent validation of the ADTR method, in that the reconstruction that is learned from similar fully reconstructed events can be applied to those that we do not have a way to validate, and still return physical results.

Again, to investigate the events that are occurring near the Teflon reflectors, we again restrict the  $z$ -position of these events to the range  $20 < |z_{\text{ADTR}}| < 172$  mm.

**Table 7.2:** Locations for 0CC events. Events that are within  $20 < |z| < 172$  mm and  $R > 172$  mm categories are used to investigate the Teflon reflectors. All events have between 28000-50000 raw scintillation counts.

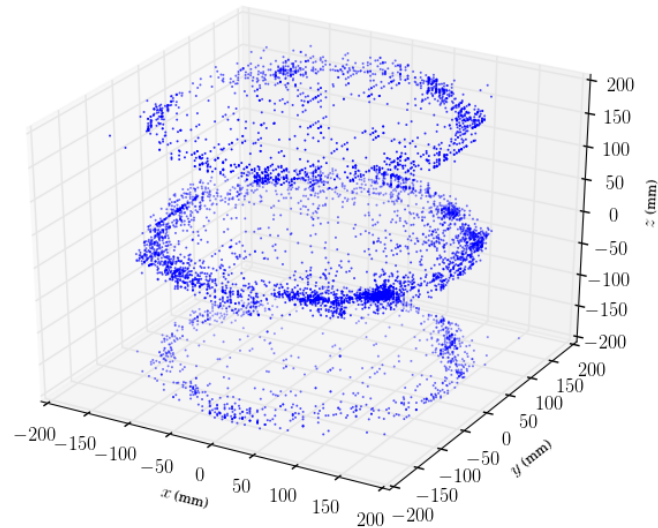
$R > 172$ mm	3207
$R < 172$ mm	16477
outside fiducial $z$	6217
$20 <  z  < 172$ mm	13467
$20 <  z  < 172$ mm & $R > 172$ mm	2766
Total	19684

There is a much smaller percentage of cathode and anode events in the 0CC population; these events are illustrated with and without radial cuts in Figure 7.7. 0CC events within  $20 < |z| < 172$  mm are shown in with and without radial cuts Figure 7.8. While there are some projection effects on the left and right sides of the figures, there is a clear feature in TPC1 ( $+z$ ).

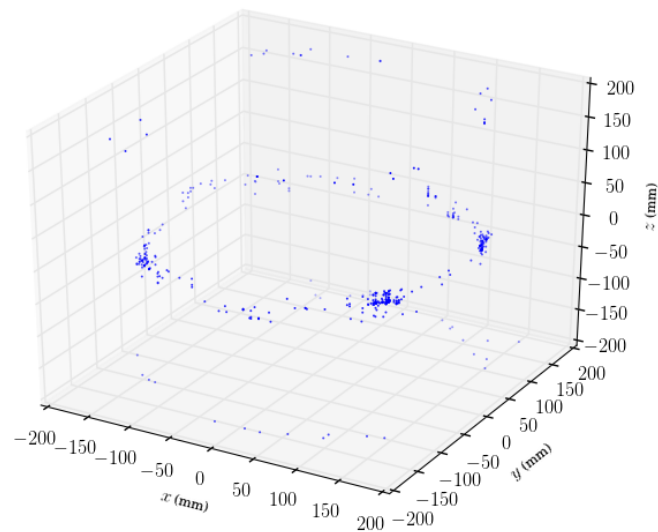
## 7.5 Non-Uniformity

The  $z$ -distributions of the 1CC (Figure 7.5) and 0CC (Figure 7.5) events are tested separately to determine consistency with a uniform distribution using the Kolmogorov-Smirnov test. We use only the  $R > 172$  mm events that fall inside the fiducial  $z$ , due to the Teflon reflectors starting 18.43 mm away from the cathode.

For the 1CC Teflon events, we fail to reject that the event distribution along the  $z$ -axis is uniform in TPC1; however, we find that the distribution is not consistent with a uniform distribution for TPC2 with  $p = 0.1$ . The cumulative distribution functions (CDFs) for the distribution of events along the  $z$ -axis are shown in Figure 7.10. However, there are only 890 events in this set, so we also look to the 0CC events. The CDFs for the 0CC events are shown in Figure 7.12. The  $z$ -position distribution for both TPCs are inconsistent with a uniform distribution with  $p < 0.0001$ .

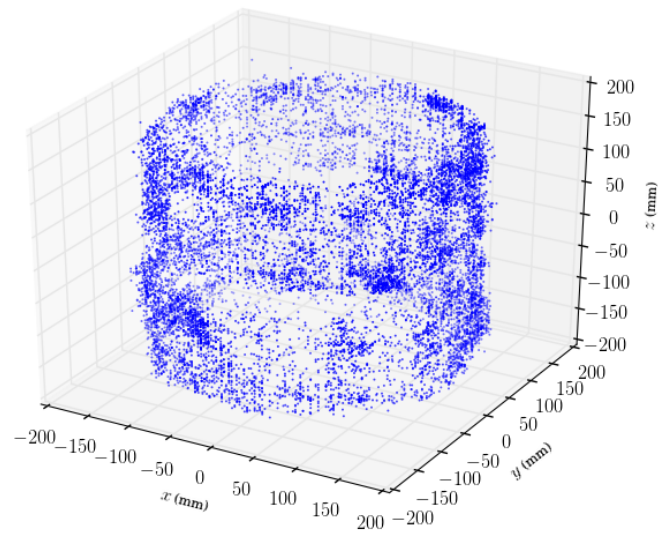


(a)

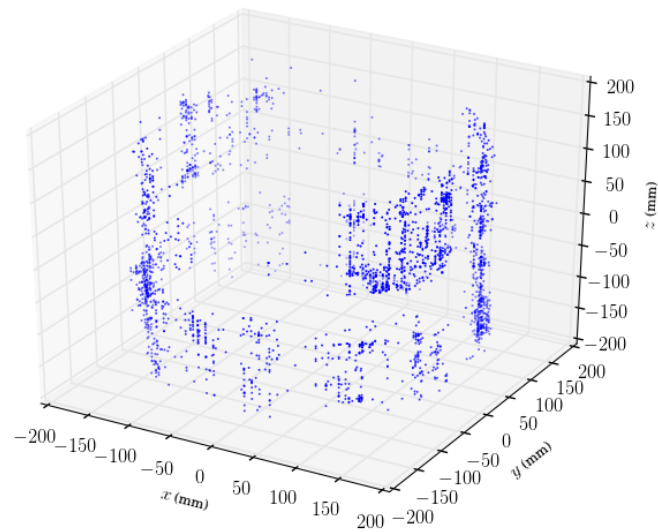


(b)

**Figure 7.7:** 0CC events that occur outside of the region  $20 < |z| < 172$  mm (a) without and (b) with the  $R > 172$  mm requirement.



(a)



(b)

**Figure 7.8:** 0CC events that occur within  $20 < |z| < 172$  mm (a) without and (b) with the  $R > 172$  mm requirement.

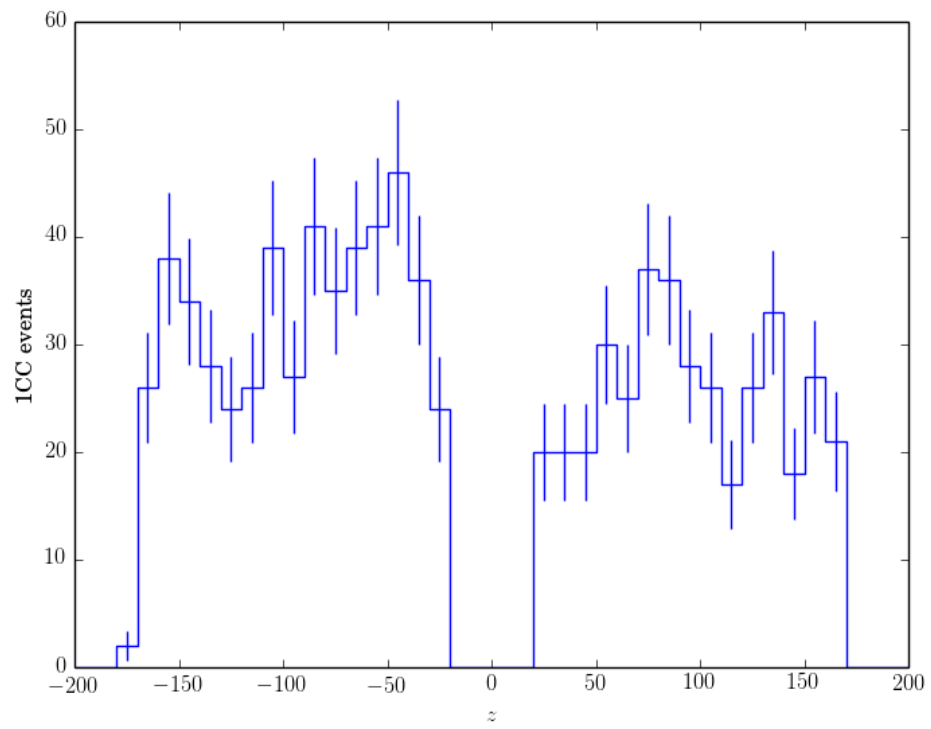
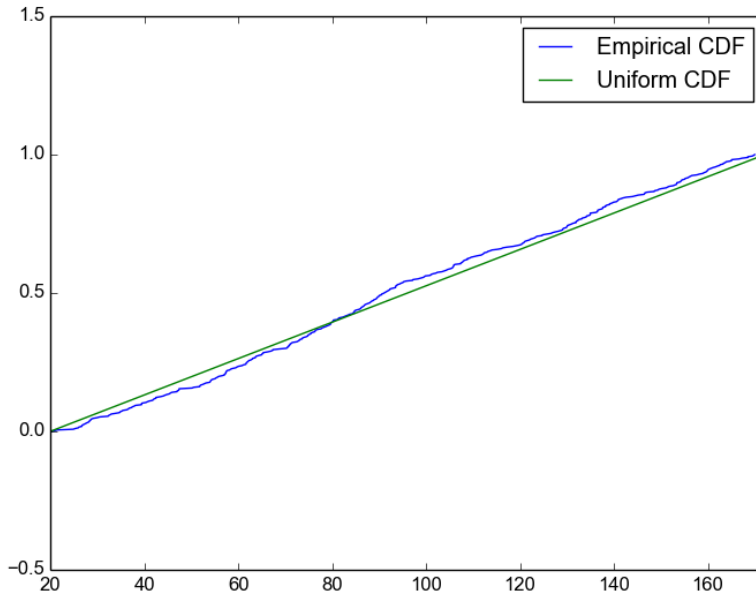
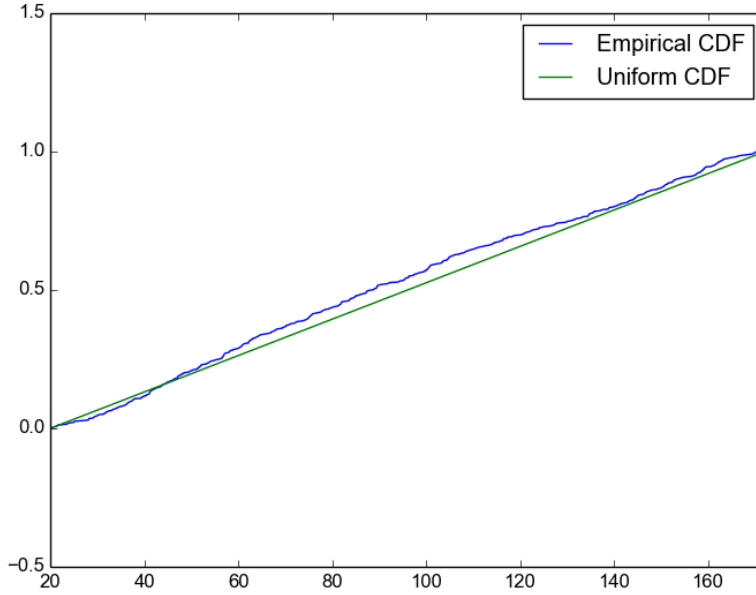


**Figure 7.9:**  $z$ -distribution of all 1CC events with  $20 < |z| < 172$  mm and  $R > 172$  mm.



(a)



(b)

**Figure 7.10:** Cumulative distribution functions (CDFs) for 1CC  $R > 172\text{mm}$  events in (a) TPC1 and (b) TPC2. Blue is the empirical CDF of the distribution of events in  $|z|$ ; green is the CDF for a uniform distribution. There is a slight deficit in events toward the cathode in both TPCs. The distribution of events along the  $z$ -axis is not inconsistent with a uniform distribution in TPC1, but is inconsistent with a uniform distribution in TPC2.

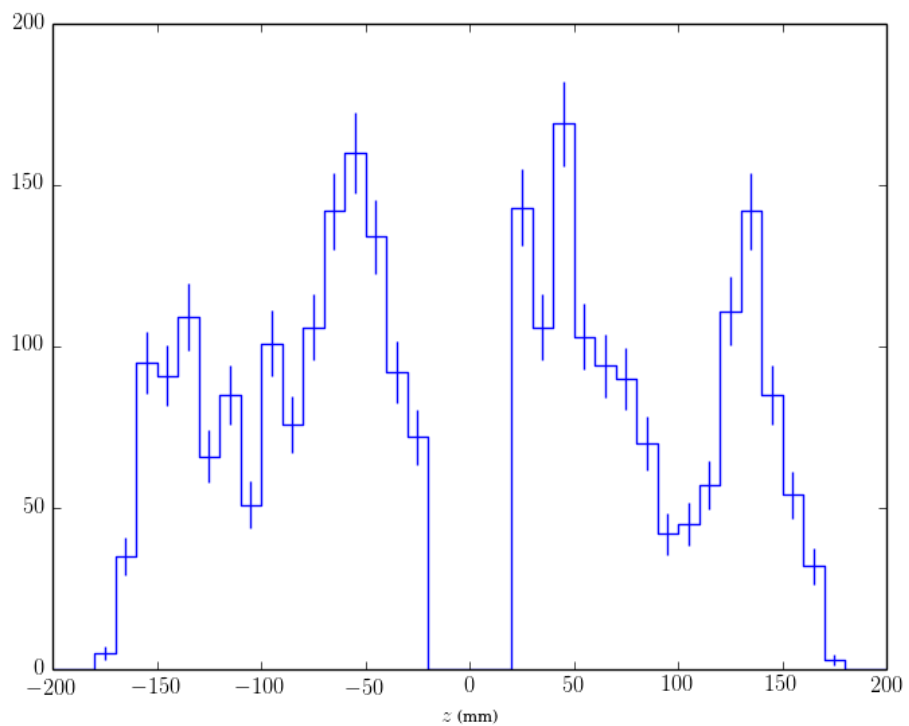
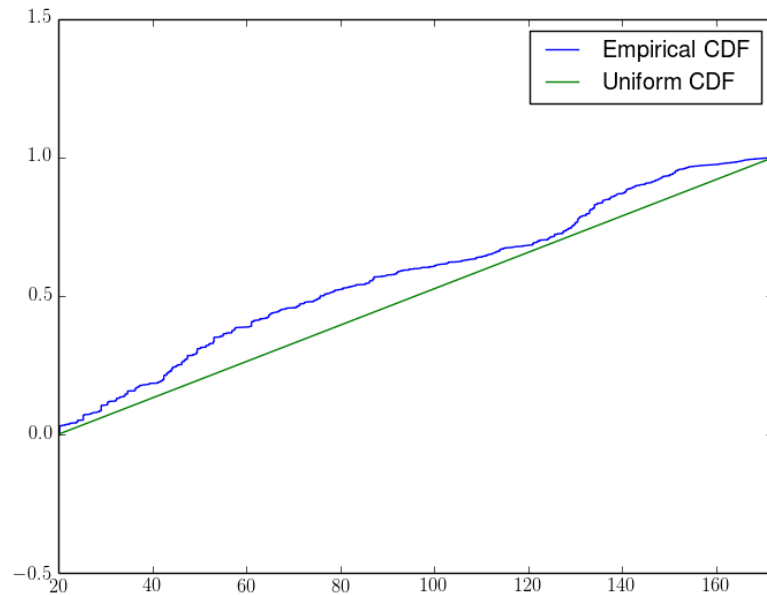
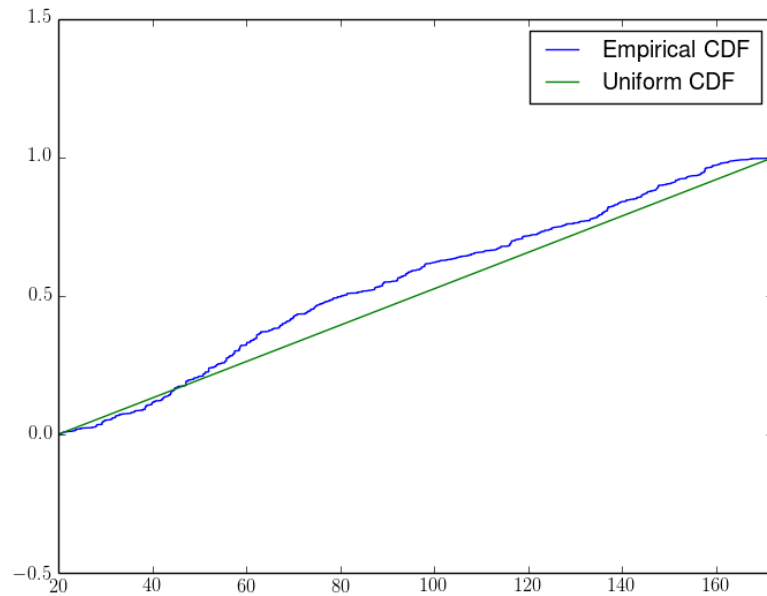


**Figure 7.11:**  $z$ -distribution of all 0CC events with  $20 < |z| < 172$  mm and  $R > 172$  mm.



(a)



(b)

**Figure 7.12:** Cumulative distribution functions (CDFs) for 0CC  $R > 172\text{mm}$  events in (a) TPC1 and (b) TPC2. Blue is the empirical CDF of the data; green is the CDF for a uniform distribution. The distribution of events along the  $z$ -axis is not consistent with a uniform distribution in either TPC.

## Bibliography

- [1] Vaga Industries, <http://www.vaga.com/>.
- [2] ANSYS, Maxwell 2D, <http://www.ansys.com/>.
- [3] 3M Novec 7000, <http://www.3m.com/>.
- [4] Aurubis, <http://www.aurubis.com/en/home/>.
- [5] J. Abdurashitov et al. Results from sage. *Phys. Lett.*, B328:234–248, 1994.
- [6] K. Abe et al. Observation of Electron Neutrino Appearance in a Muon Neutrino Beam. *Phys. Rev. Lett.*, 112:061802, 2014.
- [7] S. Abe et al. Precision Measurement of Neutrino Oscillation Parameters with KamLAND. *Phys. Rev. Lett.*, 100:221803, 2008.
- [8] N. Ackerman et al. Observation of two-neutrino double-beta decay in  $^{136}\text{Xe}$  with the exo-200 detector. *Phys. Rev. Lett.*, 107:212501, Nov 2011.
- [9] P. A. R. Ade et al. Planck 2015 results. XIII. Cosmological parameters. 2015.
- [10] M. Agostini et al. Results on Neutrinoless Double- $\beta$  Decay of  $^{76}\text{Ge}$  from Phase I of the GERDA Experiment. *Phys. Rev. Lett.*, 111(12):122503, 2013.
- [11] Q. R. Ahmad et al. Measurement of the rate of  $\nu_e + d \rightarrow p + p + e^-$  interactions produced by  $^8\text{B}$  solar neutrinos at the Sudbury Neutrino Observatory. *Phys. Rev. Lett.*, 87:071301, 2001.
- [12] J. B. Albert et al. Improved measurement of the  $2\nu\beta\beta$  half-life of  $^{136}\text{Xe}$  with the exo-200 detector. *Phys. Rev. C*, 89:015502, Jan 2014.
- [13] J. B. Albert et al. Cosmogenic Backgrounds to  $0\nu\beta\beta$  in EXO-200. 2015.
- [14] J. B. Albert et al. Investigation of radioactivity-induced backgrounds in EXO-200. *Phys. Rev.*, C92(1):015503, 2015.
- [15] J. B. Albert et al. Measurements of the ion fraction and mobility of  $\alpha$ - and  $\beta$ -decay products in liquid xenon using the exo-200 detector. *Phys. Rev. C*, 92:045504, Oct 2015.
- [16] J. Allison, K. Amako, J. Apostolakis, et al. Geant4 developments and applications. *Nuclear Science, IEEE Transactions on*, 53(1):270–278, Feb 2006.
- [17] P. Anselmann et al. Solar neutrinos observed by gallex at gran sasso. *Phys. Lett.*, B285:376–389, 1992.
- [18] J. Argyriades et al. Measurement of the Double Beta Decay Half-life of Nd-150 and Search for Neutrinoless Decay Modes with the NEMO-3 Detector. *Phys. Rev.*, C80:032501, 2009.
- [19] J. Argyriades et al. Measurement of the two neutrino double beta decay half-life of Zr-96 with the NEMO-3 detector. *Nucl. Phys.*, A847:168–179, 2010.
- [20] R. Arnold et al. First results of the search of neutrinoless double beta decay with the NEMO 3 detector. *Phys. Rev. Lett.*, 95:182302, 2005.
- [21] V. N. Aseev et al. An upper limit on electron antineutrino mass from Troitsk experiment. *Phys. Rev.*, D84:112003, 2011.

- [22] M. Auger et al. The exo-200 detector, part i: detector design and construction. *Journal of Instrumentation*, 7(05):P05010, 2012.
- [23] M. Auger et al. Search for neutrinoless double-beta decay in  $^{136}\text{Xe}$  with exo-200. *Phys. Rev. Lett.*, 109:032505, Jul 2012.
- [24] F. T. Avignone, III, S. R. Elliott, and J. Engel. Double Beta Decay, Majorana Neutrinos, and Neutrino Mass. *Rev. Mod. Phys.*, 80:481–516, 2008.
- [25] J. N. Bahcall, N. A. Bahcall, and G. Shaviv. Present Status of the Theoretical Predictions for the  $^{36}\text{Cl}$  Solar-Neutrino Experiment. *Physical Review Letters*, 20:1209–1212, May 1968.
- [26] J. N. Bahcall and G. Shaviv. Solar Models and Neutrino Fluxes. *ApJ*, 153:113, July 1968.
- [27] A. M. Bakalyarov, A. Ya. Balysh, S. T. Belyaev, V. I. Lebedev, and S. V. Zhukov. Results of the experiment on investigation of Germanium-76 double beta decay: Experimental data of Heidelberg-Moscow collaboration November 1995 - August 2001. *Phys. Part. Nucl. Lett.*, 2:77–81, 2005. [Pisma Fiz. Elem. Chast. Atom. Yadra2,21(2005)].
- [28] A. S. Barabash and V. B. Brudanin. Investigation of double beta decay with the NEMO-3 detector. *Phys. Atom. Nucl.*, 74:312–317, 2011.
- [29] J. Barea and F. Iachello. Neutrinoless double-beta decay in the microscopic interacting boson model. *Phys. Rev.*, C79:044301, 2009.
- [30] J. Bernabeu. On the history of the PMNS Matrix... with today's perspective. *Nuovo Cim.*, C037(03):145–154, 2014.
- [31] S. M. Bilenky and C. Giunti. Neutrinoless double-beta decay: A brief review. *Mod. Phys. Lett.*, A27:1230015, 2012.
- [32] L. Breiman, J. Friedman, R. Olshen, and C. Stone. *Classification and Regression Trees*. Chapman & Hall, New York, 1984.
- [33] R. Brun and F. Rademakers. Root. *Nucl. Inst. and Meth. A*, 389:81, 1997.
- [34] J. Chadwick. Possible Existence of a Neutron. *Nature*, 129:312, 1932.
- [35] T. E.-. Collaboration. Search for majorana neutrinos with the first two years of exo-200 data. *Nature*, 510:229–234, 2014.
- [36] G. Danby, J.-M. Gaillard, K. Goulian, L. M. Lederman, N. Mistry, M. Schwartz, and J. Steinberger. Observation of High-Energy Neutrino Reactions and the Existence of Two Kinds of Neutrinos. *Physical Review Letters*, 9:36–44, July 1962.
- [37] C. Davis. *A Search for the Neutrinoless Double Beta Decay of Xenon-136 with Improved Sensitivity from Denoising*. PhD thesis, University of Maryland, 2014. Ph.D. Thesis.
- [38] R. Davis, D. S. Harmer, and K. C. Hoffman. Search for neutrinos from the sun. *Phys. Rev. Lett.*, 20:1205–1209, May 1968.
- [39] P. A. M. Dirac. The quantum theory of the electron. *Proc. Roy. Soc. Lond.*, A117:610–624, 1928.
- [40] DONUT Collaboration. Observation of tau neutrino interactions. *Physics Letters B*, 504:218–224, Apr. 2001.
- [41] G. Drexlin et al. The High Resolution Neutrino Calorimeter KARMEN. *Nucl. Instr. Meth.*, A289:490–495, 1990.
- [42] S. Eidelman et al. Review of particle physics. Particle Data Group. *Phys. Lett.*, B592:1–1109, 2004.

- [43] S. R. Elliott, A. A. Hahn, and M. K. Moe. Direct Evidence for Two Neutrino Double Beta Decay in  $^{82}\text{Se}$ . *Phys. Rev. Lett.*, 59:2020–2023, 1987.
- [44] S. R. Elliott and P. Vogel. Double beta decay. *Annual Review of Nuclear and Particle Science*, 52(1):115–151, 2002.
- [45] T. Feder. *Physics Today*, page 59, 1999.
- [46] E. Fermi. Tentativo di una teoria dell’emissione dei raggi beta. *Ric. Sci.*, 4:491–495, 1933.
- [47] Y. Freund and R. E. Schapire. A decision-theoretic generalization of on-line learning and an application to boosting. *Journal of Computer and System Sciences*, 55(1):119 – 139, 1997.
- [48] Y. Fukuda et al. Evidence for oscillation of atmospheric neutrinos. *Phys. Rev. Lett.*, 81:1562–1567, Aug 1998.
- [49] W. H. Furry. On transition probabilities in double beta-disintegration. *Phys. Rev.*, 56:1184–1193, 1939.
- [50] L. Gironi et al. First neutrinoless double beta decay results from CUORE-0. *AIP Conf. Proc.*, 1686:020011, 2015.
- [51] M. Goeppert-Mayer. Double beta-disintegration. *Phys. Rev.*, 48:512–516, 1935.
- [52] J. J. Gomez-Cadenas, J. Martin-Albo, M. Sorel, P. Ferrario, F. Monrabal, J. Munoz-Vidal, P. Novella, and A. Poves. Sense and sensitivity of double beta decay experiments. *JCAP*, 1106:007, 2011.
- [53] T. Hastie, R. Tibshirani, and J. Friedman. *Elements of Statistical Learning*. Springer, 2009.
- [54] W. C. Haxton. The Solar Neutrino Problem. *Annual Review of Astron and Astrophys*, 33:459–504, 1995.
- [55] K. S. Hirata et al. Observation in the Kamiokande-II Detector of the Neutrino Burst from Supernova SN 1987a. *Phys. Rev.*, D38:448–458, 1988.
- [56] K. S. Hirata et al. Real-time, directional measurement of  $^8\text{B}$  solar neutrinos in the kamiokande ii detector. *Phys. Rev. D*, 44:2241–2260, Oct 1991.
- [57] M. Hirsch, H. V. Klapdor-Kleingrothaus, and S. G. Kovalenko. New leptoquark mechanism of neutrinoless double beta decay. *Phys. Rev.*, D54:4207–4210, 1996.
- [58] M. Hirsch, H. V. Klapdor-Kleingrothaus, and S. G. Kovalenko. On the SUSY accompanied neutrino exchange mechanism of neutrinoless double beta decay. *Phys. Lett.*, B372:181–186, 1996. [Erratum: Phys. Lett.B381,488(1996)].
- [59] M. Hirsch, H. V. Klapdor-Kleingrothaus, and O. Panella. Double beta decay in left-right symmetric models. *Phys. Lett.*, B374:7–12, 1996.
- [60] P. W. Huber and A. A. Sonin. Electric charging in liquid hydrocarbon filtration: A comparison of theory and experiments. *Journal of Colloid and Interface Science*, 61(1):126 – 145, 1977.
- [61] P. W. Huber and A. A. Sonin. Theory for electric charging in liquid hydrocarbon filtration. *Journal of Colloid and Interface Science*, 61(1):109 – 125, 1977.
- [62] M. G. Inghram and J. H. Reynolds. Double beta-decay of Te-130. *Phys. Rev.*, 78:822–823, 1950.
- [63] F. James and M. Roos. Minuit - a system for function minimization and analysis of the parameter errors and correlations. *Computer Physics Communications*, 10(6):343 – 367, 1975.

- [64] V. T. Jordanov, G. F. Knoll, A. C. Huber, and J. A. Pantazis. Digital techniques for real-time pulse shaping in radiation measurements. *Nuclear Instruments and Methods in Physics Research Section A: Accelerators, Spectrometers, Detectors and Associated Equipment*, 353(1):261 – 264, 1994.
- [65] H. V. Klapdor-Kleingrothaus, A. Dietz, H. L. Harney, and I. V. Krivosheina. Evidence for neutrinoless double beta decay. *Mod. Phys. Lett.*, A16:2409–2420, 2001.
- [66] H. V. Klapdor-Kleingrothaus et al. Latest results from the Heidelberg-Moscow double beta decay experiment. *Eur. Phys. J.*, A12:147–154, 2001.
- [67] H. V. Klapdor-Kleingrothaus and I. V. Krivosheina. The evidence for the observation of  $0\nu\beta\beta$  beta beta decay: The identification of  $0\nu\beta\beta$  events from the full spectra. *Mod. Phys. Lett.*, A21:1547–1566, 2006.
- [68] H. V. Klapdor-Kleingrothaus, I. V. Krivosheina, A. Dietz, and O. Chkvorets. Search for neutrinoless double beta decay with enriched Ge-76 in Gran Sasso 1990-2003. *Phys. Lett.*, B586:198–212, 2004.
- [69] C. Kraus et al. Final results from phase II of the Mainz neutrino mass search in tritium beta decay. *Eur. Phys. J.*, C40:447–468, 2005.
- [70] D. S. Leonard et al. Systematic study of trace radioactive impurities in candidate construction materials for EXO-200. *Nucl. Instrum. Meth.*, A591:490–509, 2008.
- [71] E. Majorana and L. Maiani. A symmetric theory of electrons and positrons. In G. Bassani, editor, *Ettore Majorana Scientific Papers*, pages 201–233. Springer Berlin Heidelberg, 2006.
- [72] Z. Maki, M. Nakagawa, and S. Sakata. Remarks on the Unified Model of Elementary Particles. *Progress of Theoretical Physics*, 28:870–880, Nov. 1962.
- [73] J. Menendez, A. Poves, E. Caurier, and F. Nowacki. Neutrinoless double beta decay: The nuclear matrix elements revisited. *J. Phys. Conf. Ser.*, 312:072005, 2011.
- [74] P. Minkowski.  $\mu \rightarrow e\gamma$  at a Rate of One Out of  $10^9$  Muon Decays? *Phys. Lett.*, B67:421–428, 1977.
- [75] B. Mong et al. Spectroscopy of Ba and Ba<sup>+</sup> deposits in solid xenon for barium tagging in nEXO. *Phys. Rev.*, A91(2):022505, 2015.
- [76] B. N. L. National Nuclear Data Center. Double Beta ( $\beta\beta$ ) Decay Data. <http://www.nndc.bnl.gov/bbdecay/>, 2014.
- [77] R. Neilson et al. Characterization of large area APDs for the EXO-200 detector. *Nucl. Instrum. Meth.*, A608:68–75, 2009.
- [78] D. North. An analysis of the factors which determine signal/noise discrimination in pulsed-carrier systems. *Proceedings of the IEEE*, 51(7):1016–1027, July 1963.
- [79] I. Ogawa et al. Search for neutrino-less double beta decay of Ca-48 by CaF-2 scintillator. *Nucl. Phys.*, A730:215–223, 2004.
- [80] K. A. Olive et al. Review of Particle Physics. *Chin. Phys.*, C38:090001, 2014.
- [81] W. Pauli. Dear radioactive ladies and gentlemen. *Phys. Today*, 31N9:27, 1978.
- [82] F. Pedregosa, G. Varoquaux, A. Gramfort, V. Michel, B. Thirion, O. Grisel, M. Blondel, P. Prettenhofer, R. Weiss, V. Dubourg, J. Vanderplas, A. Passos, D. Cournapeau, M. Brucher, M. Perrot, and E. Duchesnay. Scikit-learn: Machine learning in Python. *Journal of Machine Learning Research*, 12:2825–2830, 2011.

- [83] B. Pontecorvo. Inverse beta processes and nonconservation of lepton charge. *Sov. Phys. JETP*, 7:172–173, 1958. [Zh. Eksp. Teor. Fiz.34,247(1957)].
- [84] B. Pontecorvo. Mesonium and Antimesonium. *Soviet Journal of Experimental and Theoretical Physics*, 6:429, 1958.
- [85] B. Pontecorvo. Neutrino experiments and the question of leptonic-charge conservation. *Sov. Phys. JETP*, 26:984–988, 1968.
- [86] J. Quinlan. *C4.5: programs for machine learning*. Morgan Kaufmann Publishers Inc., San Francisco, CA, 1993.
- [87] P. K. Rath, R. Chandra, K. Chaturvedi, P. K. Raina, and J. G. Hirsch. Uncertainties in nuclear transition matrix elements for neutrinoless  $\beta\beta$  decay within the PHFB model. *Phys. Rev.*, C82:064310, 2010.
- [88] F. Reines and C. L. Cowan. The Neutrino. *Nature*, 178:446–449, Sept. 1956.
- [89] R. G. H. Robertson. KATRIN: an experiment to determine the neutrino mass from the beta decay of tritium. In *Community Summer Study 2013: Snowmass on the Mississippi (CSS2013)* Minneapolis, MN, USA, July 29-August 6, 2013, 2013.
- [90] V. A. Rodin, A. Faessler, F. Simkovic, and P. Vogel. On the uncertainty in the 0 nu beta beta decay nuclear matrix elements. *Phys. Rev.*, C68:044302, 2003.
- [91] T. R. Rodriguez and G. Martinez-Pinedo. Energy density functional study of nuclear matrix elements for neutrinoless  $\beta\beta$  decay. *Phys. Rev. Lett.*, 105:252503, 2010.
- [92] J. Schechter and J. W. F. Valle. Neutrino Masses in SU(2) x U(1) Theories. *Phys. Rev.*, D22:2227, 1980.
- [93] M. R. Shafer, D. W. Baker, and K. R. Benson. Electric currents and potentials resulting from the flow of charged liquid hydrocarbons through short pipe. *Journal of Research of the National Bureau of Standards -C. Engineering and Instrumentation*, 69C(4):307–317, October-December 1965.
- [94] K. Twelker et al. An apparatus to manipulate and identify individual Ba ions from bulk liquid Xe. *Rev. Sci. Instrum.*, 85:095114, 2014.

